arXiv:2202.04098v1 [astro-ph.GA] 8 Feb 2022

Kinematics and Feedback in H II regions in the Dwarf Starburst Galaxy IC 10

Maren Cosens [ID],[1,2] Shelley A. Wright [ID],[1,2] Norman Murray,[3] Lee Armus [ID],[4] Karin Sandstrom [ID],[1,2] Tuan Do [ID],[5] Kirsten Larson [ID],[4] Gregory Martinez,[5] Sanchit Sabhlok [ID],[1,2] Andrey Vayner [ID],[6] and James Wiley [ID][1,2]

[1]*Physics Department, University of California, San Diego, 9500 Gilman Drive, La Jolla, CA 92093 USA*
[2]*Center for Astrophysics and Space Sciences, University of California, San Diego, 9500 Gilman Drive, La Jolla, CA 92093 USA*
[3]*Canadian Institute for Theoretical Astrophysics, University of Toronto, 60 St. George Street, Toronto, ON M5S 3H8, Canada**
[4]*Spitzer Science Center, California Institute of Technology, 1200 E. California Blvd., Pasadena, CA 91125 USA*
[5]*UCLA Galactic Center Group, Department of Physics & Astronomy, University of California, Los Angeles, Los Angeles, CA 90095, USA*
[6]*Department of Physics and Astronomy, Johns Hopkins University, Baltimore, MD 21218, USA*

ABSTRACT

We present a survey of the central region of the nearest starburst galaxy, IC 10, using the W. M. Keck Observatory Keck Cosmic Web Imager (KCWI) at high spectral and spatial resolution. We map the central starburst of IC 10 to sample the kinematic and ionization properties of the individual star-forming regions. Using the low spectral resolution mode of KCWI we map the oxygen abundance and with the high spectral resolution mode we identify 46 individual H II regions. These H II regions have an average radius of 4.0 pc, star formation rate $\sim 1.3 \times 10^{-4}$ M$_\odot$ yr^{-1}, and velocity dispersion ~ 16 km s^{-1}. None of the H II regions appear to be virialized ($\alpha_{\rm vir} >> 1$), and, on average, they show evidence of ongoing expansion. IC 10's H II regions are offset from the star forming region size-luminosity scaling relationships, as well as Larson's Law that relates size and velocity dispersion. We investigate the balance of inward and outward pressure, $P_{\rm in}$ and $P_{\rm out}$, finding $P_{\rm out} > P_{\rm in}$ in 89% of H II regions, indicating feedback driven expansion even in these low mass H II regions. We find warm gas pressure ($P_{\rm gas}$) provides the dominant contribution to the outward pressure ($P_{\rm out}$). This counteracts the inward pressure which is dominated by turbulence in the surrounding gas rather than self-gravity. Five H II regions show evidence of outflows which are most likely supported by either stellar winds (2 regions) or champagne flows (3 regions). These observations provide new insights into the state of the star-forming regions in IC 10 and negative feedback from low mass clusters.

Keywords: galaxies: star formation — galaxies: starburst — galaxies: kinematics and dynamics — HII regions — techniques: imaging spectroscopy — surveys

1. INTRODUCTION

H II regions are formed when UV photons from young stars and clusters ionize the surrounding gas cloud. The ionization within these regions is typically dominated by the most massive and luminous stars. This can be due to just a single O or B star (e.g., Armentrout et al. 2021)

Corresponding author: Maren Cosens
mcosens@ucsd.edu

* Canada Research Chair in Astrophysics

or a cluster of massive stars. H II regions are observed to have typical lifetimes $\lesssim 10$ Myr, starting out spatially compact ($<$pc) and expanding as they age (e.g., Spitzer 1978; Zamora-Avilés et al. 2019) before the H II region dissipates. As the H II regions expand they interact with and influence the surrounding gas. As the sites of recent massive star formation, H II regions are intrinsically linked to the efficiency of star formation in the larger molecular cloud, the properties of the Interstellar Medium (ISM), and the evolution of galaxies. The photometric and kinematic properties of H II regions are

therefore of great interest for studying and understanding the progression of star formation.

There are a number of surveys studying ionized and diffuse gas in and around the H II regions of nearby galaxies. Some of the first studies of extragalactic H II regions used Hα imaging with photographic plates and CCD's to map the ionized gas in the Small Magellanic Cloud (SMC) and Large Magellanic Cloud (LMC) (e.g., Davies et al. 1976; Kennicutt & Hodge 1986) as well as other nearby galaxies (e.g. NGC 6822, Hodge et al. 1989). With Hα imaging they were able to measure the size and flux of star forming regions and explore their size distributions and luminosity functions. As instrumentation improved, Fabry-Perot mapping added measurements of the ionized gas kinematics both within the H II regions and in the diffuse gas component, finding ∼ 4× higher velocity dispersions (σ) in the diffuse gas (e.g., Valdez-Gutiérrez et al. 2002). With the advent of integral field spectrographs (IFS), surveys could map the resolved gas properties and kinematics at ∼kpc scale. Large surveys such as CALIFA (Sánchez et al. 2012a), SAMI (Croom et al. 2012), and MaNGA(Bundy et al. 2015), studied hundreds to thousands of star forming galaxies and their resolved properties. These surveys have resulted in numerous publications including studies of galaxy dynamical scaling relations (Cortese et al. 2014), measurement of a "resolved" star forming main sequence (Ellison et al. 2018), and the fundamental metallicity relation (Cresci et al. 2019). The CALIFA survey also made the important characterization of the Diffuse Ionized Gas (DIG) showing a trend in the Hα equivalent width with both the position on the BPT diagram as well as galaxy morphological type for this large sample of galaxies (Espinosa-Ponce et al. 2020). Using the MaNGA survey, Rodríguez del Pino et al. (2019) identify ionized gas outflows in 7% of the studied Hα emitting galaxies, finding evidence of shocks in most of the outflows with larger velocities associated with more massive galaxies.

State of the art IFS's operating at visible wavelengths such as the Multi-Unit Spectroscopic Explorer (MUSE, Bacon et al. 2010), and the Keck Cosmic Web Imager (KCWI, Morrissey et al. 2018), have begun to allow incredibly high spatial and spectral resolution mapping of nearby H II regions. For example, Castro et al. (2018) used MUSE to map the giant H II region 30 Doradus, generating resolved maps of the ionization state and revealing bi-modal gas velocities surrounding the star cluster R136. In another study, McLeod et al. (2019) use MUSE to map two LMC H II region complexes and characterize the role of stellar feedback mechanisms, finding stellar winds and thermal gas pressure to be dom-

inant. Studying two giant H II regions in M101 with KCWI, Bresolin et al. (2020) find evidence of expanding shells and an underlying broad emission component potentially attributable to stellar winds interacting with cold gas.

The process of energy from star formation being injected into and influencing the surrounding gas through feedback can be caused by a variety of mechanisms. These mechanisms and their impact are typically discussed in the context of the larger molecular clouds surrounding the compact H II regions where the pressure originates. An important form of feedback is radiation pressure which occurs when stellar photons interact with dust grains in the surrounding molecular cloud thereby transferring both energy and momentum. The energy imparted to the molecular gas may be radiated away, but the momentum cannot and therefore may be able to more effectively cause expansion of the gas (Krumholz et al. 2014).

The ionizing photons produced in a star cluster also act to heat the surrounding H II region gas to typical temperatures of ∼ 10^4K. This warm gas generates an important source of outward pressure that may cause the expansion and eventual disruption of the region and surrounding gas. An additional source of thermal pressure comes from hot gas heated by shocks from stellar winds. The bubbles of hot gas produced can be observed via emitted X-rays. However, this hot gas is less effective in disrupting the region since it is limited by leakage through low density regions and turbulent mixing occurring with the neighboring cold gas resulting in enhanced thermal emission (Krumholz et al. 2019). Supernovae explosions also produce shocked winds in a short burst that can disrupt star-forming regions, but these don't occur until a few million years after the formation of the first massive stars by which point the molecular gas may be significantly disrupted or cleared already.

Which of these feedback mechanisms is dominant in different star forming environments is still a matter of some debate. Observational studies seek to determine the relative impact of each of these forms of pressure by estimating the energy input to the ISM or the pressure produced by each component. For instance, the giant H II region, 30 Doradus, has been one target of such pressure studies investigating the physical processes leading to the complex structure in this single region (Lopez et al. 2011; Pellegrini et al. 2011). These types of studies are often limited to just a few H II regions or a single giant H II region, making it difficult to form conclusions about the general population of star forming regions. IC 10 provides a unique laboratory to study the effectiveness of many of these forms of feed-

back in a statistically significant sample. Thanks to the >100 previously identified H II regions, a large sample of compact regions can be studied simultaneously, and the recent nature of the starburst allows the effectiveness of pre-SNe feedback to be investigated.

IC 10 is the nearest starburst galaxy at a distance of 715kpc (Kim et al. 2009), and the only one in the Local Group. It is also a dwarf galaxy with low metallicity; approximately $0.25\times$ solar (Magrini & Gonçalves 2009; Skillman et al. 1989). IC 10 has a higher density of Wolf-Rayet stars than both the SMC and LMC (e.g. Tehrani et al. 2017), indicating that the current observed burst of star formation is relatively recent. These unique characteristics as well as it's close proximity have made IC 10 the subject of numerous studies.

Studies of the gas in IC 10 have shown an expansive H I component stretching $\sim7\times$ larger than the optical component of the galaxy (e.g., Huchtmeier 1979; Namumba et al. 2019). The central region of the H I gas has been observed to have a regularly rotating disk structure with an extended counter-rotating component beyond that (e.g., Shostak & Skillman 1989; Wilcots & Miller 1998; Ashley et al. 2014). These studies also find kinematically distinct "spurs" and "plumes" that do not follow the main H I disk. The origin of these features is currently not well known but possible explanations presented include an as of yet undetected companion galaxy or a late stage merger (e.g., Ashley et al. 2014), ongoing accretion of primordial gas onto the main body of IC 10 (e.g., Wilcots & Miller 1998), past interaction with a body such as another dwarf galaxy (e.g., Nidever et al. 2013), or some combination of these mechanisms.

Narrow-band Hα imaging by Hodge & Lee (1990) was used to identify 144 individual H II regions and complexes throughout IC 10 and measure their characteristic properties such as size and SFR. The majority of the identified star-forming regions lie in the central $2.5'\times2.5'$ of the irregular galaxy. Thurow & Wilcots (2005) studied the ionized gas kinematics in a portion of this field with a fiber-fed IFS utilizing $3''$ fibers and achieving a maximum resolution of 23 km s^{-1}. Interestingly, they find larger line widths in the diffuse gas than in the compact H II regions which they attribute to a super-position of components with different velocities. They find that stellar winds are likely to have shaped much of the ionized and neutral gas in this region. Polles et al. (2019) model fine structure cooling lines observed in IC 10 with the photoionization code Cloudy (Ferland et al. 2017) finding relatively uniform properties between the five regions studied, which match the characteristics of matter-bounded regions allowing photons to escape and ionize the diffuse gas. These unique characteristics

of IC 10 make it an ideal target to study a large sample of young, evolving star-forming regions.

In order to better understand the conditions of star formation and its impact on galaxy properties it is important to study not only local H II regions, but also the sites of star formation throughout cosmic time. The H II regions of IC 10 provide an important tool for comparison with the $\sim$kpc scale star-forming "clumps" found at z $\gtrsim$ 1 (e.g., Livermore et al. 2012; Mieda et al. 2016). These clumps are found to have high velocity dispersions ($\sigma \gtrsim$ 50km s^{-1}, e.g., Genzel et al. 2011; Mieda et al. 2016) indicating strong energetics and significant amounts of turbulence present. In an effort to understand these massive star-forming regions and compare them to their more compact local counterparts, the scaling relationships between clump properties such as size, luminosity, and velocity dispersion are explored in order to provide insight into the process driving clump formation. However, these studies have yielded some conflicting results, in particular regarding whether high-z clumps are offset to higher luminosities than local H II regions for a given size (e.g., Wisnioski et al. 2012; Livermore et al. 2015). This was initially proposed as a possible redshift evolution in the size-luminosity scaling relationship (Livermore et al. 2012, 2015), but later studies by Wisnioski et al. (2012) and Mieda et al. (2016) did not find evidence of such an evolution. In order to investigate this discrepancy, our team compiled a comprehensive sample of high-z and local star-forming regions and developed a Bayesian Markov Chain Monte Carlo (MCMC) fitting framework to investigate these scaling relations in detail (Cosens et al. 2018). We did not find any clear evidence of redshift evolution with this expansive sample, nor a definite selection affect between lensed and field galaxies at high-z. Instead, we found evidence that there may be a break in the size-luminosity relationship based on the star formation rate (SFR) surface density, Σ_{SFR}.

A key area of parameter space missing in these scaling relationship investigations are compact ($\lesssim$50pc), low-luminosity (10^{34-36}erg s^{-1}) star-forming regions studied with the same methodology as at high-z. These compact regions set the constraint on the intercept of the relationship; a critical component in interpreting changes in slope or offsets between samples. Observing the H II regions of IC 10 with the KCWI IFS provides an ideal target to study a large sample of H II regions at unprecedented angular resolution, probing this missing parameter space and allowing for an improved comparison of local and high-z star-forming regions.

Despite the extensive study of IC 10, the exact distance to the dwarf galaxy remains rather uncertain since

it lies close to the plane of the Milky Way. Measured distances have ranged between 500kpc (Sakai et al. 1999) and >2Mpc (Bottinelli et al. 1984), with distances ~700kpc being used more recently (e.g., Ashley et al. 2014; Polles et al. 2019). Throughout this paper we will use the distance of 715±60 kpc measured by Kim et al. (2009) but we will also report the angular size of all measured structures. For the systemic velocity of IC 10 we will use the value of $-348 \pm 10 \mathrm{km\,s^{-1}}$ determined from the 21 cm line (Tifft & Cocke 1988).

In Section 2 we describe the observations carried out on the central starburst of IC 10 with KCWI and the method of reduction. Then we identify H II regions in our observations (Section 3.1), extract H II region spectra (Section 3.2), and determine SFRs (Section 3.3) and masses (Section 3.4). In Section 3.5 we investigate the kinematics of the field and H II regions, virialization and energetics. We estimate the metallicity throughout the field (Section 3.6), investigate the Diffuse Ionized Gas (Section 3.7), and study the star formation scaling relations (Section 3.8). In Section 4 we discuss how these results inform a picture of young H II regions still evolving. Lastly, in Section 5 we summarize our results.

2. OBSERVATIONS & DATA REDUCTION

2.1. *KCWI Observations*

We used KCWI (Morrissey et al. 2018) at the W.M. Keck Observatory to observe the star forming H II regions of IC 10. These observations tile a combined ~1.25 sq. deg. field of view (FoV) in the central region of the galaxy with the highest concentration of H II regions. We use a low resolution mode making use of KCWI's large slicer and BL grating which we will refer to as the "large slicer, R~900" mode, as well as a high resolution mode which uses the small slicer and BH3 grating which we will refer to as the "small slicer, R~18,000" mode. Observations in these two modes cover approximately the same FoV in order to combine the exceptional spatial sampling (0.35″/pixel) and spectral resolution (0.125Å/channel) of the small slicer, with the wavelength coverage afforded with the low resolution grating (3500-5500Å). We determine our achieved resolution by measuring the point-spread-function of the observed standard stars giving an average FWHM~ 1" across the observing nights in both modes. In this paper we will limit our discussion primarily to the high resolution "small slicer, R~18,000" observations with the "large slicer, R~900" mode providing the extinction correction and metallicity diagnostics in Section 3.6.

In the high resolution mode we obtain a wavelength range of 4700-5200Å and a FoV of 8.4″ × 20.4″ for each exposure, providing coverage of Hβ, [OIII]4959Å, and

[OIII]5007Å. A typical pointing consists of three 120s exposures with a dither pattern of 0, -1.5, +2 slices[1] perpendicular to the slices to improve sampling and avoid saturation of the bright [OIII]5007Å line. In the large slicer, R~900 mode we obtain wider FoV and spectral coverage in each exposure (3500-5500Å and 33″ × 20.4″) with lower spatial resolution of 1.35″/pixel. We limit these exposure times to 6s to avoid saturation at [OIII]5007Å and complete 5 exposures per pointing with a dither pattern of 0, -0.5, -1.5, -2.5, -0.5, 0 slices. Due to the nature of the extended diffuse emission in the FoV of our science observations we took standalone sky frames approximately once every hour for each mode at an exposure time of 120s in the small slicer mode and 6s in the larger slicer mode. With each exposure we saved the associated guide camera image to be used in correcting WCS errors. The observation details are summarized in Table 1 with the total FoV of each observing mode illustrated in Figure 1.

2.2. *Data Reduction*

Raw data were reduced using the IDL version of the public KCWI Data Reduction Pipeline (DRP) version 1.1.0 (Don et al. 2018) with modifications for our data set described here.

The first stage of the DRP consists of bias subtraction, gain correction, and cosmic ray removal procedures. In the default pipeline, the overscan region is used to perform a secondary bias subtraction after removal of the master bias to account for variation in the read noise between the calibration and science frames. We take this a step further to modify the bias subtraction used in our reduction to include a *scaled* bias subtraction. Before the bias subtraction occurs we take the ratio of the overscan regions in the science and master bias frame for each row of the detector and multiply the master bias row by this ratio before subtracting it. This gives us a better match to the readnoise throughout the night and between the two distinct chips of the detector (with distinct amplifiers and readnoise).

Stages 2-4 of the DRP perform scattered light subtraction, determine transformations to 3D data cubes (used later), and flat field correction, respectively. We skip stage 5 of the DRP which performs sky subtraction in favor of using our own scaled sky subtraction routine on the reduced data cubes. Before this subtraction is performed, we run DRP stage 6 generating data cubes with the geometric solutions of stage 3, stage 7 to perform a correction for differential atmospheric refraction,
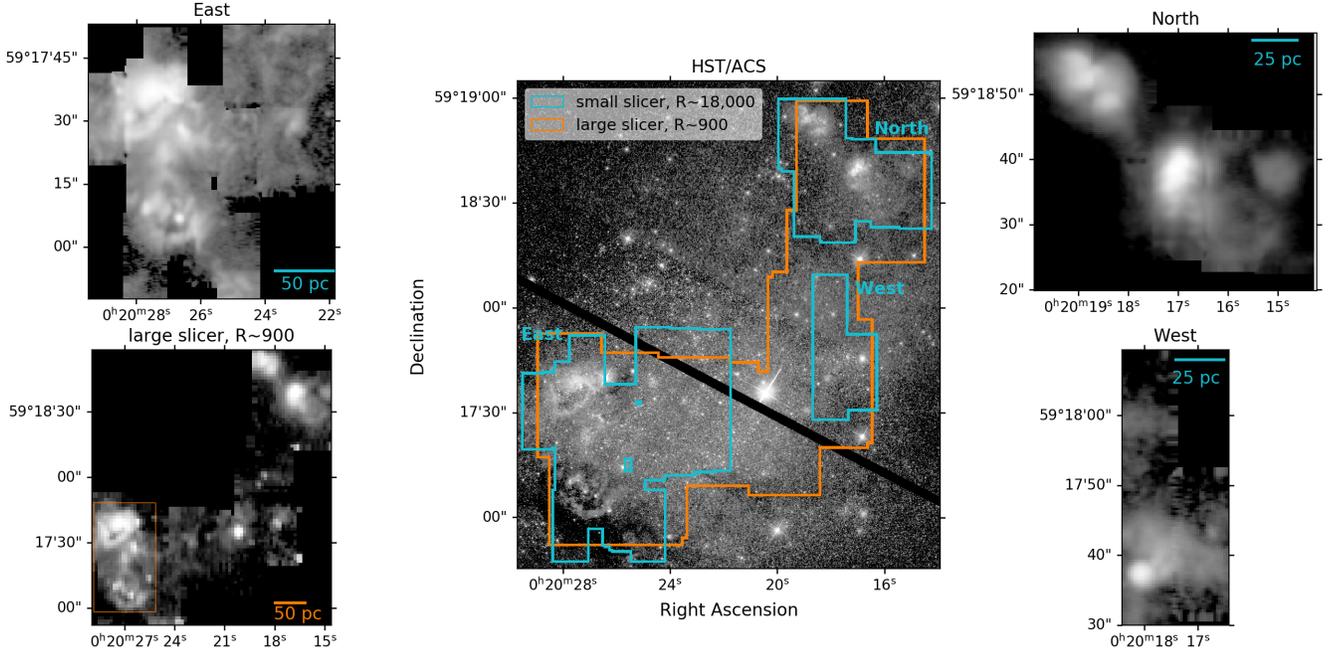
---

[1] (-): left; (+): right

Figure 1. (Middle): HST/ACS image of IC 10's central $2' \times 2'$ showing outlined field coverage of our completed and in progress KCWI observations in two modes: the high resolution small slicer, R∼18,000 mode (blue), and the coarse resolution large slicer, R∼900 mode (orange). (Top Left): Integrated [OIII]5007Å flux map from the East region of our small slicer, R∼18,000 observations. (Bottom Left): Large slicer, R∼900 observations. The extinction correction (Section 3.2) is determined from this full field, but the metallicity analysis of Section 3.6 is limited to the field inside the orange outline due to low SNR outside of the H II regions in the remainder of the field. (Top Right): North region of the small slicer, R∼18,000 observations. (Bottom Right): West region of the small slicer, R∼18,000 observations.

Table 1. KCWI Observational Summary

Date (mm-dd-yyyy)	Time (UT)	Airmass	Pointings	Exposures/Pointing	Exposure Time(s)	Standard Star
		small slicer, R∼18,000				
11-22-2017	4:30 - 5:40	1.41-1.36	1	3	900	L870-2
11-23-2017	4:17-5:50	1.43-1.31	3	3	300	Feige 24
08-16-2018	11:06 - 13:23	1.41-1.30	8	3	120	NGC7293/Feige 24
09-03-2018	11:20 - 14:23^a	1.3-1.5	5	3	120	NGC7293
08-16-2020	10:57 - 14:22	1.30-1.41	11	3	120-360	NGC7293/Feige24
		large slicer, R∼900				
08-16-2018	14:00 - 14:37	1.32-1.37	5	5	6	Feige24
08-16-2020	14:41 - 15:20	1.38-1.46	7	5	6	Feige24

Note—Summary of Keck/KCWI observations of IC 10's H II regions. Approximately the same fields are observed in both modes for complimentary observations. There is some overlap in pointings between nights to increase SNR in fainter areas of IC 10 so the total number of pointings is not the sum of each night. Approximately 1/2 of the small slicer R∼900 pointings are still in progress with more exposure time needed to achieve sufficient SNR at [OII]3727Å to determine metallicities, but the SNR is sufficient throughout the field for determining an extinction correction at the H II regions.

^{a}There was an observational gap from 12:31-13:51 UT due to inclement weather.

and stage 8 which uses observations of standard stars to flux calibrate the cubes. The final data products from this pipeline are flux calibrated data cubes for both sky and science observations with associated variance cubes.

After completion of the standard pipeline steps we run a custom scaled sky subtraction on the data. This routine takes an average spectrum over the entire cube for the science frame and associated sky observation. The ratio of these two spectra are computed away from any known emission lines. This ratio is then used to scale the average sky spectrum, which is then subtracted from every spaxel of the science data cube. Errors are propagated in this step using the associated object and sky variance cubes along with the computed scale factor.

WCS offsets between individual frames in the "small slicer, R∼18,000" mode were corrected by matching stars in the guide camera images to HST/ACS imaging of IC 10. The average offset of the measured and expected coordinates of stars in the field was used to shift the associated KCWI frame. On average, a 0.7″ offset in declination and a 1.2″ offset in right ascension were found for the "small slicer, R∼18,000" frames. We did not find WCS offsets in the "large slicer, R∼900 observations, and thus do not apply this step for that mode. All observations from each of the two observing modes were mosaicked with the rectangular KCWI pixels binned to square using the Python package `reproject` (Robitaille et al. 2020) before analysis.

Since the observations were spread over a multi-year period, we compared the calibration frames to ensure consistency in these steps. The master bias frames produced in DRP stage 1 for each night show a standard deviation in median flux of $< 0.5\%$ in the small slicer, R∼18,000 mode and $< 0.2\%$ in the large slicer, R∼900 mode. Similarly, the master flats produced in DRP stage 4 show only a standard deviation of $< 1\%$ in the small slicer, R∼18,000 mode and $< 0.1\%$ in the large slicer, R∼900 mode.

3. ANALYSIS

3.1. *Identifying star-forming regions*

Preliminary flux maps are generated for each emission line by summing over 15 channels (1.875Å) centered at the systemic velocity of IC 10 (-348km s^{-1}, Tifft & Cocke 1988). More robust flux maps are generated later from spectral fitting, but these preliminary maps are used so as not to introduce boundary effects from low SNR regions in the H II region identification routine. We use the python package, `astrodendro` (Thomas et al. 2013), to find the locations and extent of star forming H II regions in our [OIII] and Hβ flux maps. `Astrodendro` finds hierarchical structure in data sets by starting at

the pixels with the highest flux and progressing to lower flux pixels surrounding those. If a local maximum is found `astrodendro` creates a new structure with that as the peak when the local maximum is above a user defined threshold. As the algorithm progresses to lower flux values a system of leaves, branches, and trunks are defined relating these local maxima (see Rosolowsky et al. 2008, for an illustration of this method). In this system the leaves are the most compact structures, the individual H II regions in this study, while the branches connect the larger H II region complexes. The trunks are the bottom level of the hierarchical structure identified by `astrodendro` and show the extent of the ionized gas emission in our KCWI observations. If these observations covered the full optical extent of IC 10, we would expect the trunks to identify distinct areas of star-formation in the galaxy. However, since these observations are focused only on areas of high star formation activity the trunks fill the majority of the field and are therefore not physically significant in this study.

In order for a local flux maximum to be considered a real structure we have set a series of constraints to be applied by `astrodendro` - some of which are standard parameters in the package and some that are required routines unique to our data set. Standard parameters that we constrain with `astrodendro` are the minimum peak value for a structure, the minimum flux a pixel can contain in order to be added to any structure, and the minimum step size between independent structures (leaves) derived from the variance cubes resulting from the KCWI DRP. We have also written custom routines to set the minimum radius and minor axis length required for a real structure defined by the point spread function (PSF) of standard star observations. The values provided for these constraints are given in Table 2 for the [OIII]5007Å flux maps; the analysis with the Hβ maps uses the values obtained with the same σ requirements.

To accurately identify H II regions and determine SFRs, we first remove the background of Diffuse Ionized Gas (DIG). It is not possible to do this spectrally on individual spaxels since some locations have too low of SNR to determine the velocity shift (particularly in locations of greater DIG contribution). We identified three regions where there are no known H II regions in our observed field (identified by the white and red boxes in Figure 2). We find the mean flux per pixel in each of these regions, and take the minimum value to be our DIG contribution so as not to over-subtract flux at this stage (the red box). The average DIG contribution in all three cases is on the order of a percent in pixels associated with H II regions, so the DIG region chosen should
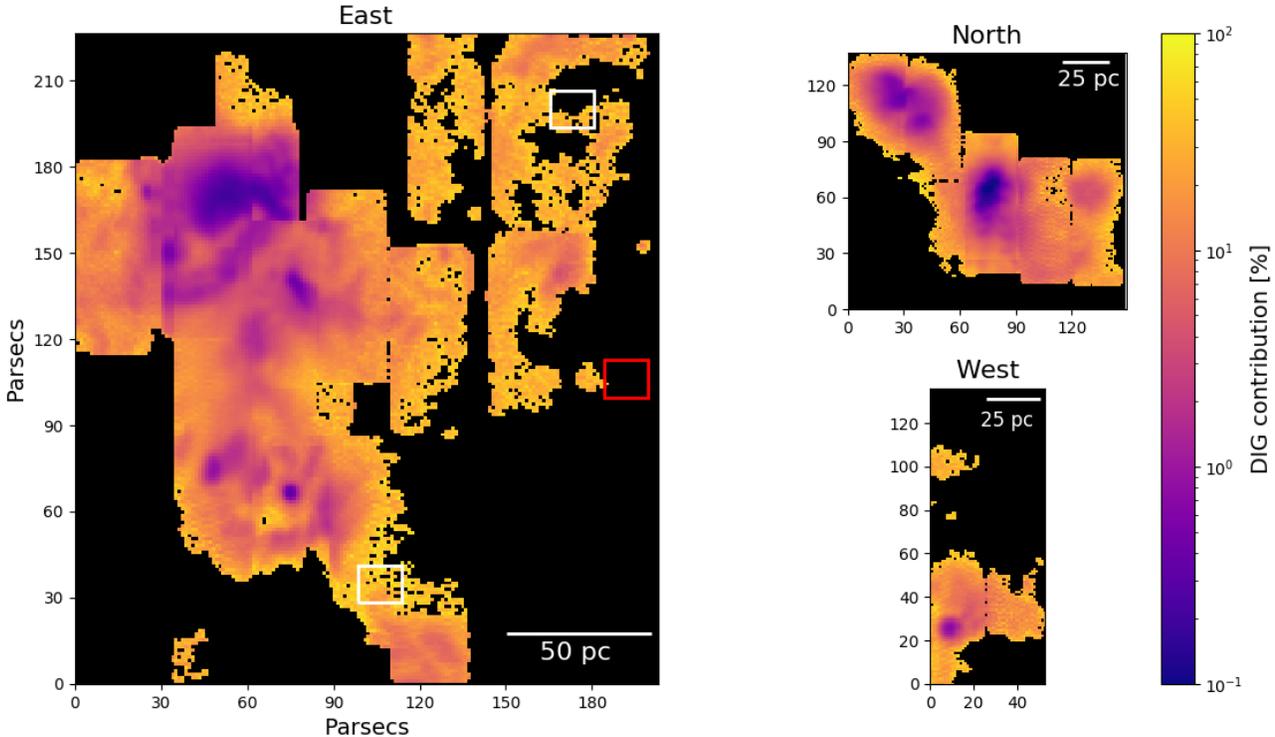
Figure 2. Map of the Diffuse Ionized Gas (DIG) contribution to the total [OIII]5007Å flux before subtraction. The locations of HII regions are identified after this DIG contribution is removed from the flux maps. Spaxels with SNR< 2 are masked in this figure. The DIG flux per pixel was evaluated in the three outlined boxes, with the region outlined in red chosen for the DIG subtraction as it contained the minimum flux per pixel.

Table 2. Clump Identification Constraints

Type	Value
Minimum radius	1.4px
(HWHM)	~ 0.5"
Minimum peak flux	3.7×10^{-17}
$[\mathrm{erg\,s^{-1}\,cm^{-2}\,\mathring{A}^{-1}}]$	(5σ)
Minimum peak delta	7.3×10^{-18}
$[\mathrm{erg\,s^{-1}\,cm^{-2}\,\mathring{A}^{-1}}]$	(1σ)
Minimum flux	2.2×10^{-17}
$[\mathrm{erg\,s^{-1}\,cm^{-2}\,\mathring{A}^{-1}}]$	(3σ)

NOTE—Parameters used to constrain the `astrodendro` clump fitting procedure after correcting the KCWI small slicer, R~18,000 flux maps for the background DIG. The values listed for each constraint are for the [OIII]5007Å flux maps, but the same constraint method (e.g., 5σ minimum peak flux) is used for all emission lines.

not make a significant difference in the subsequent analysis. Maps of the DIG contribution to the integrated [OIII]5007Å flux are shown in Figure 2. Finally, we subtract the mean DIG flux/pixel from every location in our flux maps. For the small slicer, R~18,000 observations, this removes on average 21% of the [OIII]5007Å flux per spaxel, with significantly lower contribution at the HII regions. We repeat this subtraction on integrated flux maps for each emission line using the same DIG region throughout. We also extract a mean DIG spectrum over this same region for use in correcting HII region spectra to be discussed in Section 3.2.

The `astrodendro` package has the option to compute dendrograms on either 2D (position-position) or 3D (position-position-velocity) data. We chose to use our flux maps for HII region identification due to the need to subtract the DIG contribution to identify fainter regions. To test whether any major differences in identified HII regions were produced by the choice of using flux maps, the dendrograms constructed from unsubtracted flux maps and data cubes were compared. For the latter, a defined range of spectral channels is used to limit the analysis to a single emission line and a requirement is added that the spectral extent of each structure exceeds 0.38Å, the average width of arc lines

determined from Gaussian fits to lines in the calibration frames separated every 100Å. There was not a significant deviation in either the size or number of H II regions identified with these two methods and therefore we proceed in the analysis of regions identified from the DIG subtracted flux maps.

Running `astrodendro` on the 2D [OIII]5007Å flux map and manually removing narrow filaments or regions truncated by the edge of the mosaic results in the identification of 46 H II regions. The average radius is 4.0 pc with a Σ_{SFR} of $0.20\,M_\odot\ \mathrm{yr}^{-1}\ \mathrm{kpc}^{-2}$. Each of these identified regions are listed in Table 3 with the contours shown in the [OIII]5007Å and Hβ flux maps of Figure 3. Using the 2D Hβ flux map produces the same H II region locations in areas of high SNR, but the lower SNR of the Hβ line means that faint regions cannot be identified in this map that can in [OIII]5007Å. Since the results are consistent in areas where the SNR is high for both lines, we proceed with the region identification from the [OIII]5007Å flux map.

It should be noted that there are more compact structures within the identified H II regions which can be seen visually (Figure 3) but do not result in unique structures detected by `astrodendro`. In some cases these structures do not meet the resolution requirements, but in others it is a result of using the same identification criteria across the entire field. A larger number of H II regions can be identified using location dependent criteria, but that introduces an extra element of uncertainty in requiring manual tuning of the parameters. It is more prudent to maintain consistent requirements for H II region identification across the study even if it does not result in perfect separation of compact structures.

3.1.1. *H II Region Naming*

Throughout this paper the identified H II regions will be referred to with a naming convention based on a simple grid divided into $15''\times15''$ regions spanning the optical extent of IC 10. This grid based naming convention provides a simpler method of comparison between studies and extension to a larger FoV than the initial H II region naming developed in the study by Hodge & Lee (1990), as discussed in more detail in Appendix A. The grid rows are numbered from 0 - 24 with columns designated A - X as illustrated in Figure 4 and Appendix Figure A1. H II regions will be assigned a name consisting of their column followed by their row (e.g., J16). In the case of multiple H II regions falling into the same square of this grid, they are assigned an additional letter, "a,b,c,etc.", in order of decreasing luminosity (e.g., J16a). Each knot belonging to a larger complex will be given its own designation based on the knot center with

the parent complex listed in column 2 of Table 3 along with the designation from Hodge & Lee (1990) if there is a corresponding one in column 3.

3.1.2. *Defining the Radius*

There are a number of ways in which to define the size of star-forming regions, and the use of these methods is not always consistent between studies, particularly when comparing local and high-redshift samples with widely varying resolution. One method is to assume a spherically symmetric region (such as a Strömgren sphere) and fit the flux profile with a 2D elliptical Gaussian (e.g., Wisnioski et al. 2012). The half-width at half-maximum (HWHM) then gives an estimate of the half-light radius, $r_{1/2}$. A second method is to fit contours to the flux profile at a defined level above the noise and then sum the pixels contained within the contour to determine the area, A, of the region. This area can then be used to define the effective radius, $r_{\mathrm{eff}} = \sqrt{A/\pi}$ (e.g., Larson et al. 2020). This total area is produced by the `astrodendro` algorithm, from which we calculate r_{eff} of the H II regions in IC 10. A third method, also produced by `astrodendro`, takes an approach that compromises between the two previous methods. Rather than summing the pixels within the defined contour the second moment of the structure is determined along the direction of greatest elongation and the direction perpendicular to that. The HWHM determined by these second moments is then used to define an ellipse centered at the region peak and calculate its area. We use this area to define a pseudo half-light radius, $r_{1/2}^* = \sqrt{A_{\mathrm{ellipse}}/\pi}$ which we will use as the characteristic size of the H II regions throughout this paper. We compare the result of using each of these three methods to define the extent of the H II regions in IC 10 in Appendix B along with a discussion of the definitions used in similar studies.

Our choice of determining region sizes from the second moments will be most directly comparable to high-redshift studies which use $r_{1/2}$, but we do not expect significant biases from including studies using r_{eff} in our investigation of the scaling relationships (Section 3.8) due to the larger impact of the PSF in high-redshift observations and the systematically larger uncertainties on measured sizes.

3.2. *H II Region Spectra*

Spectra are extracted for each identified H II region by integrating the flux over a circular aperture defined by the region center position and $r_{1/2}^*$ at each wavelength channel using the `aperture_photometry` function in the Python package `photutils`. With this we produce an integrated flux and error spectrum for each region. The use of a circular aperture will necessarily

Table 3. H II Region Catalogue (small slicer, R~18,000)

Region ID	Complex	HL90 ID	RA	Dec	Radius	
			(J2000)	(J2000)	(pc)	(arcseconds)
G16	⋯	125	00h20m29.14s	+59d17m32.37s	2.60 ± 0.22	0.75 ± 0.06
G17	⋯	⋯	00h20m28.81s	+59d17m21.76s	2.11 ± 0.18	0.61 ± 0.05
H16a	c_H16	111c/111e	00h20m27.35s	+59d17m36.49s	10.32 ± 0.87	2.98 ± 0.25
H16b	c_H16	111d	00h20m28.23s	+59d17m31.24s	2.95 ± 0.25	0.85 ± 0.07
H17a	c_H17	111a	00h20m26.57s	+59d17m27.05s	5.08 ± 0.43	1.47 ± 0.12
H17b	c_H17	111b	00h20m27.12s	+59d17m22.66s	4.14 ± 0.35	1.20 ± 0.10
H17c	c_H16	111e	00h20m28.06s	+59d17m26.90s	3.54 ± 0.30	1.02 ± 0.09
H18a	c_I18	106a	00h20m26.61s	+59d17m07.72s	4.74 ± 0.40	1.37 ± 0.12
H18b	c_H18	106b	00h20m27.53s	+59d17m09.82s	4.08 ± 0.34	1.18 ± 0.10
H18c	c_H18	106	00h20m27.08s	+59d17m08.61s	2.19 ± 0.18	0.63 ± 0.05
H18d	⋯	106	00h20m27.33s	+59d17m02.74s	3.38 ± 0.28	0.98 ± 0.08
H18e	⋯	115	00h20m28.05s	+59d17m11.42s	2.72 ± 0.23	0.79 ± 0.07
I16a	⋯	⋯	00h20m24.82s	+59d17m35.54s	2.60 ± 0.22	0.75 ± 0.06
I16b	⋯	⋯	00h20m24.66s	+59d17m42.49s	2.31 ± 0.19	0.67 ± 0.05
I17a	⋯	100	00h20m25.33s	+59d17m24.36s	2.56 ± 0.21	0.74 ± 0.06
I17b	⋯	⋯	00h20m24.82s	+59d17m26.99s	3.02 ± 0.25	0.87 ± 0.07
I17c	⋯	⋯	00h20m24.72s	+59d17m17.36s	2.10 ± 0.18	0.61 ± 0.05
I18	c_I18	106	00h20m26.26s	+59d17m04.28s	7.02 ± 0.59	2.03 ± 0.17
I19a	c_I19	97	00h20m25.18s	+59d16m51.19s	3.51 ± 0.30	1.01 ± 0.09
I19b	c_I19	91	00h20m24.69s	+59d16m51.24s	3.30 ± 0.28	0.95 ± 0.08
J15	⋯	⋯	00h20m23.07s	+59d17m43.78s	2.71 ± 0.23	0.78 ± 0.07
J16a	⋯	86/87	00h20m23.91s	+59d17m42.08s	7.72 ± 0.65	2.23 ± 0.19
J16b	c_J16	73	00h20m23.06s	+59d17m29.61s	4.46 ± 0.37	1.29 ± 0.11
J16c	c_J16	77	00h20m23.38s	+59d17m31.51s	2.24 ± 0.19	0.65 ± 0.05
J16d	⋯	⋯	00h20m23.01s	+59d17m38.83s	3.74 ± 0.31	1.08 ± 0.09
J17a	⋯	74	00h20m23.37s	+59d17m17.83s	3.76 ± 0.32	1.09 ± 0.09
J17b	⋯	⋯	00h20m24.08s	+59d17m15.08s	3.50 ± 0.29	1.01 ± 0.08
J17c	⋯	85	00h20m23.99s	+59d17m27.41s	2.94 ± 0.25	0.85 ± 0.07
J17d	⋯	74a	00h20m22.83s	+59d17m18.09s	3.09 ± 0.26	0.89 ± 0.08
J17e	c_J17	83	00h20m23.92s	+59d17m19.54s	2.61 ± 0.22	0.75 ± 0.06
J17f	⋯	74	00h20m22.97s	+59d17m21.34s	3.18 ± 0.27	0.92 ± 0.08
J17g	c_J17	84	00h20m23.93s	+59d17m21.84s	2.91 ± 0.24	0.84 ± 0.07
K16	⋯	⋯	00h20m22.50s	+59d17m42.22s	5.10 ± 0.43	1.47 ± 0.12
L11	c_L11	50b/50c	00h20m18.85s	+59d18m53.14s	5.32 ± 0.45	1.54 ± 0.13
M11	c_L11	50a	00h20m18.38s	+59d18m49.17s	2.77 ± 0.23	0.80 ± 0.07
M12	c_M12	45	00h20m16.95s	+59d18m37.43s	9.24 ± 0.78	2.67 ± 0.23
M14	⋯	49	00h20m18.10s	+59d17m58.82s	6.74 ± 0.57	1.95 ± 0.16
M16a	c_M16	46a/46b	00h20m17.84s	+59d17m38.78s	8.45 ± 0.71	2.44 ± 0.21
M16b	c_M16	46c	00h20m18.32s	+59d17m43.01s	2.62 ± 0.22	0.76 ± 0.06
M16c	c_M16	44	00h20m16.76s	+59d17m39.25s	2.61 ± 0.22	0.75 ± 0.06
M16d	⋯	48	00h20m18.17s	+59d17m31.05s	3.33 ± 0.28	0.96 ± 0.08
N12a	⋯	36	00h20m15.03s	+59d18m37.82s	6.79 ± 0.57	1.96 ± 0.16
N12b	⋯	37	00h20m15.56s	+59d18m33.30s	1.98 ± 0.17	0.57 ± 0.05
N13a	c_M12	41	00h20m16.02s	+59d18m25.67s	3.91 ± 0.33	1.13 ± 0.10
N13b	⋯	35	00h20m15.28s	+59d18m27.28s	3.26 ± 0.27	0.94 ± 0.08
N15	⋯	43	00h20m16.56s	+59d17m45.47s	2.85 ± 0.24	0.82 ± 0.07

NOTE—H II regions identified in small slicer, R~18,000 observations of IC 10 following the new region identification scheme laid out in Section 3.1.1 and the radius definition adopted in Section 3.1.2.
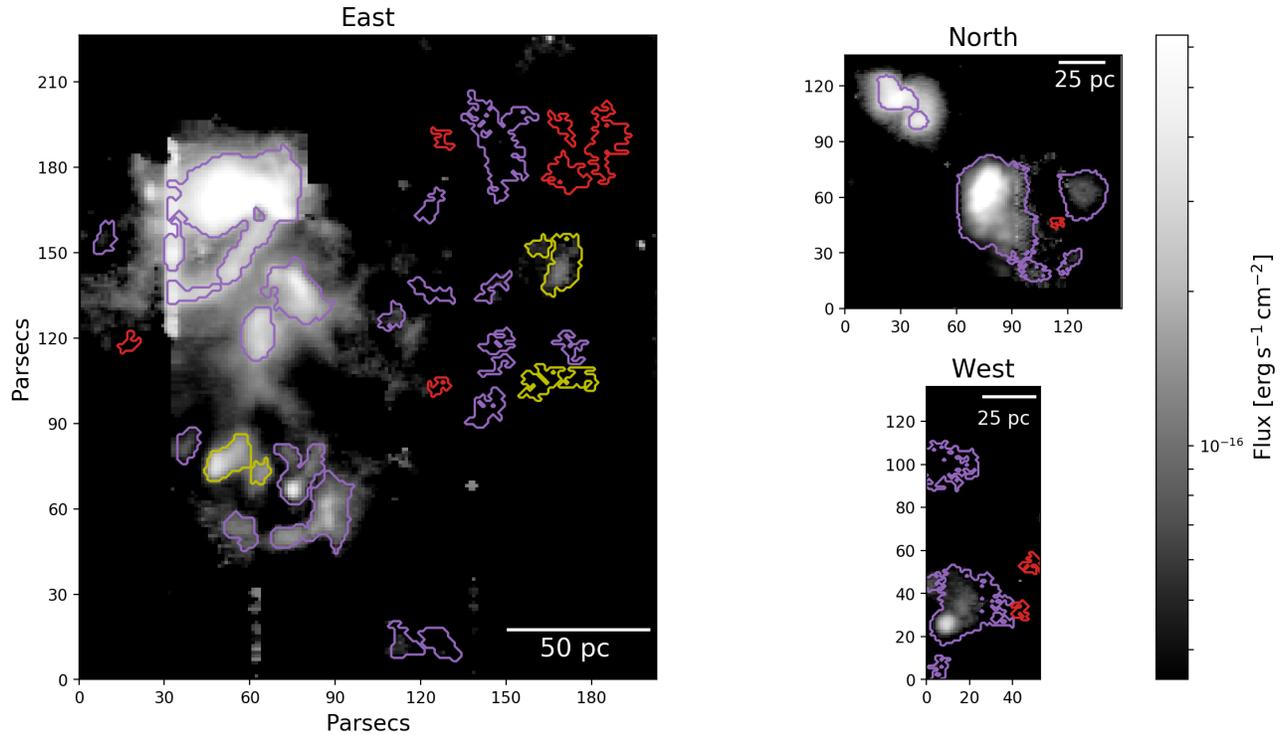
(a) [OIII]5007Å

(b) Hβ
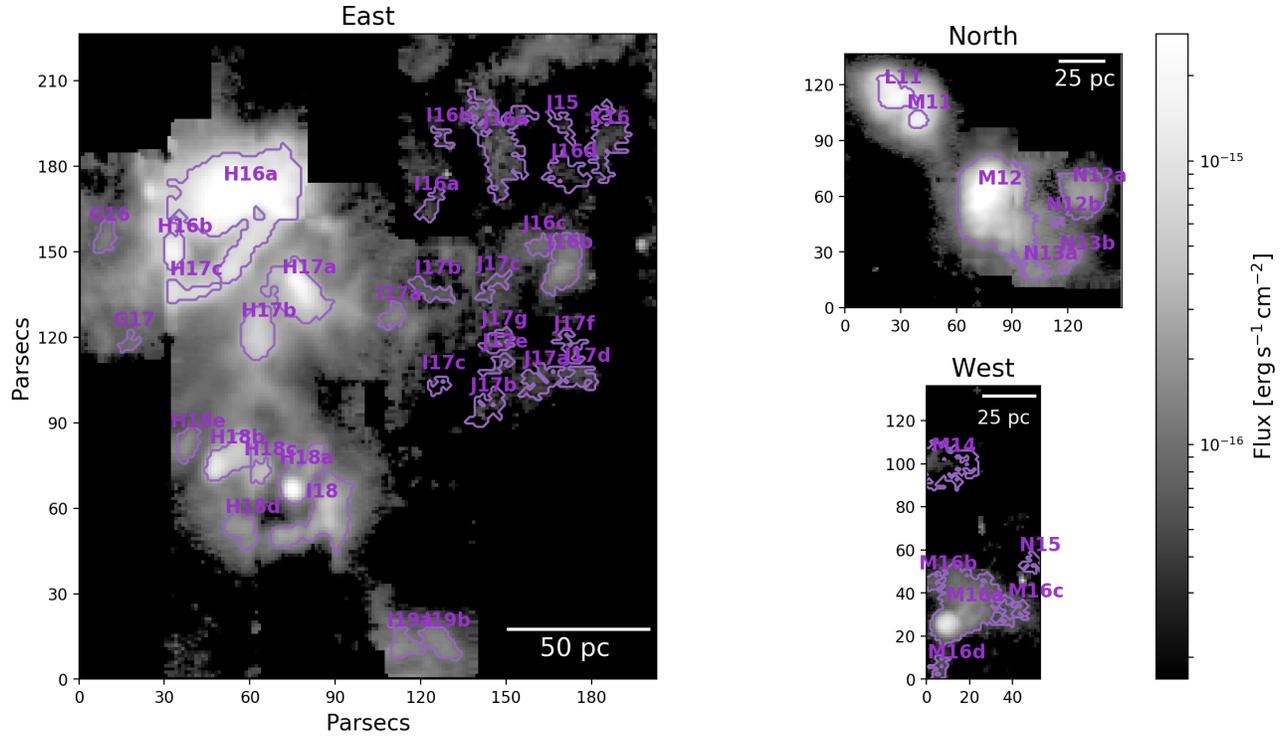
Figure 3. Maps of integrated flux of the ionized gas in IC 10 measured from Gaussian fits to the [OIII]5007Å (a) and Hβ (b) lines at each spaxel for the high resolution "small slicer, R∼18,000" observing mode. Each map is divided into the "North" portion of the FoV in the upper right, the lower right shows the "West" field, and the "East" region of the observed field on the left. The purple contours mark the edges of the most compact H II region structures found by `astrodendro` in the [OIII]5007Å flux map. The H II regions outlined in red in the Hβ map were not found by `astrodendro` on this lower SNR map, and the H II regions outlined in yellow were blended into single regions. SNR >2 is required for these maps, with more spaxels falling below this cut in Hβ. It should be noted that the H II region contours are determined from integrated flux maps at [OIII]5007Å rather than these maps generated from Gaussian fits at each spaxel due to the regions with too low of SNR to perform DIG subtraction at the individual spaxel.
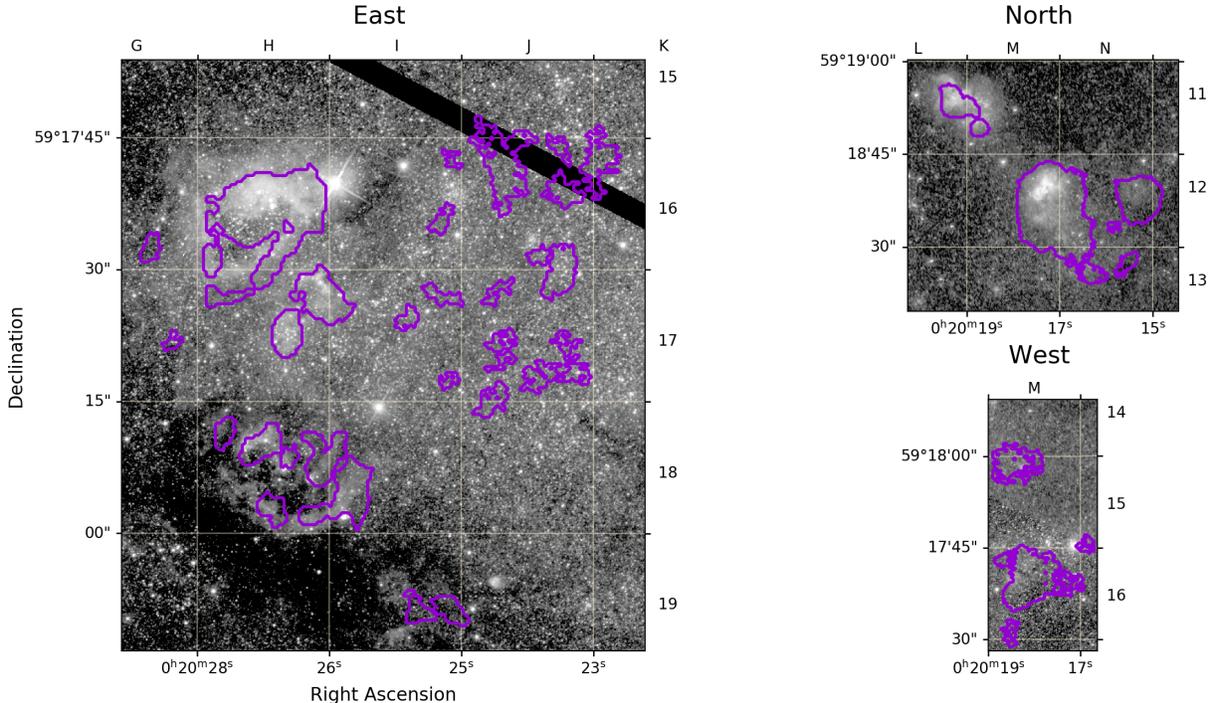
Figure 4. Coordinate grid for proposed H II region naming scheme overlaid on an HST/ACS image of the galaxy. The column letter is shown along the top of each image with the row number along the right hand side. H II regions are named based on the column and row corresponding to their center. The HST image is divided into the "East", "West", and "North" sections as in the presentation of the KCWI maps throughout this paper (e.g., Figure 3) with the identified H II regions outlined in purple.

exclude the edges of asymmetric H II regions, but it will capture the core which provides the dominant contribution to the flux. The use of a circular aperture has also been found to include less bias from background emission (Wisnioski et al. 2012). Since the DIG subtraction prior to the construction of the dendrogram uses a lower limit on this emission source, the exact boundaries may be biased by this estimation while the circular aperture is less impacted. To ensure the choice of aperture does not bias the conclusions of this paper key analysis was carried out with both integration methods. While the size, luminosity, and dependent properties do increase slightly for integration over the exact area, the trends observed and conclusions reached in the following analysis do not change. Therefore we proceed with the analysis and results using the circular aperture with $r^*_{1/2}$. The integrated spectra are corrected for the underlying DIG contribution. To do this a Gaussian profile is fit to the [OIII]5007Å line in both the region and mean DIG spectrum. Any wavelength shift between these Gaussian centers is corrected and the DIG spectrum is subtracted from the integrated region spectrum with a scaling factor for the number of spaxels in the integrated region. For the remainder of our analysis we use this DIG subtracted spectrum.

We fit each spectrum with a continuum and a Gaussian profile at each emission line, weighted by the associated error spectrum. An example of these fits is shown in Figure 5 for region G16 with the full figure set of fits for the remainder of the H II regions available in Appendix C. The velocity shift of the region is determined from the mean of the Gaussian fit to [OIII]5007Å relative to the proper motion of IC 10 ($-348 \pm 1 \, \mathrm{km \, s^{-1}}$; Tifft & Cocke 1988). The velocity dispersion is determined from the standard deviation of the Gaussian fit with the instrumental width subtracted in quadrature. The total flux of the emission line is determined by integrating over the Gaussian profile and is converted to luminosity using a distance to IC 10 of $715 \pm 60 \, \mathrm{kpc}$ (Kim et al. 2009). For nearly all cases the emission is well represented by a single Gaussian, but one region, J16a, exhibits a double peaked [OIII]5007Å line. For this special case integrating over the single Gaussian profile underestimates the flux by ~30% compared to a pure sum over the emission line. For this region we instead fit a double Gaussian, using the primary component to derive the velocity shift and dispersion, and integrating over both peaks to determine the flux.

Emission line luminosities are corrected for extinction determined from the ratio of the Hβ and Hγ Balmer lines in the large slicer, R~900 H II region spectra. We
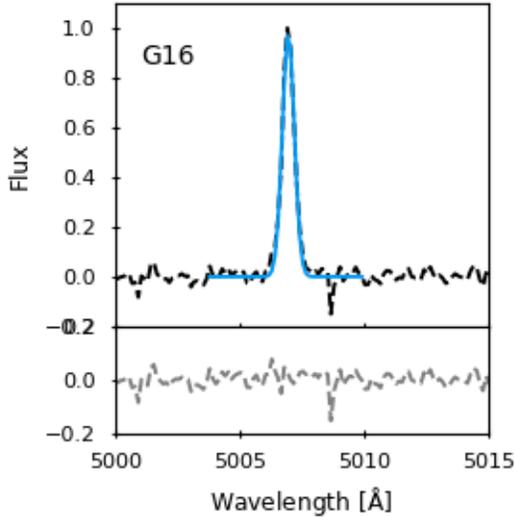
Figure 5. Thumbnail of region G16 integrated spectrum at [OIII]5007Å in the small slicer, R∼18,000 observing mode. The complete figure set including spectra from all identified H II regions (46 images) are available in the online journal and as thumbnails in Appendix C. The spectral lines are fit by a single Gaussian profile (except for J16a with a double Gaussian profile) shown in cyan with the residuals shown in grey below the associated spectrum. The spectra have been normalized to the peak of the [OIII]5007Å line.

use the ratio of the integrated flux of each of these lines along with the theoretical line ratio of 0.47 assuming Case B recombination (Osterbrock & Ferland 2006) to determine the $E(B-V)$ reddening in each of the identified H II regions following Momcheva et al. (2013)'s Equation A10:

$$E(B-V) = \frac{-2.5}{\kappa(H\beta) - \kappa(H\gamma)} \times log_{10}\left(\frac{0.47}{(H\gamma/H\beta))_{\mathrm{obs}}}\right) \tag{1}$$

where $\kappa(H\beta) = 4.6$ and $\kappa(H\gamma) = 5.12$.

For the H II regions identified, we determine an average total reddening value of $E(B-V) = 0.67 \pm 0.10$ with a higher nominal reddening $E(B-V) = 0.97 \pm 0.24$ in a stacked spectrum of spaxels outside the H II regions, though these values overlap when incorporating the measurement uncertainties. The reddening in the stacked spectrum outside the H II regions had to be determined using the peak flux of the $H\beta$ and $H\gamma$ lines due to lower SNR at $H\gamma$ resulting in a poor fit. We expect this to be a reasonable approximation as the difference introduced by this method inside the H II regions is less than $1/3$ of the uncertainty on the associated $E(B-V)$. The larger uncertainty on the estimated reddening outside the H II regions is likely to encompass the possible source of error introduced by the use of peak flux.

The reddening determined in our H II region spectra are lower than the values found by Kim et al. (2009) via NIR colors of RGB stars ($E(B-V) = 1.01 \pm 0.03$) and from UBV photometry of early type stars ($E(B-V) = 0.95 \pm 0.06$), but the estimated reddening for IC 10 varies widely throughout the literature. These estimates have ranged from $E(B-V) = 0.47$ (Lequeux et al. 1979) to upwards of 1.7 (Yang & Skillman 1993) with a variety of methods used. These estimates are of the total reddening, including the foreground reddening from the Milky Way. IC 10 is at a low galactic latitude, so estimates of even the foreground reddening show large variation. The estimate from the commonly used survey by Schlegel et al. (1998) gives $E(B-V) \sim 1.6$, larger than many of the estimates for the total reddening in IC 10. Kim et al. (2009) notes the large uncertainties in the Schlegel et al. (1998) maps at low galactic latitude and finds a foreground extinction of $E(B-V) = 0.52$ towards IC 10. Given the wide variation in reddening determined for IC 10 we therefore proceed with the values determined from our spectra as this is likely to provide the most accurate measure of the extinction in our FoV.

For the remainder of the analysis all spectra will be extinction corrected according to the associated $E(B-V)$ determined from the appropriate stacked spectrum of spaxels either inside or outside of H II regions and a Cardelli et al. (1989) extinction law. These two different measurements of extinction are particularly important in accurately correcting the extinction of these two distinct gas regions prior to estimates of the metallicity in Section 3.6 using the R_{23} parameter with emission lines covering a wide wavelength range (e.g., Kewley et al. 2019). Ideally each spaxel would be extinction corrected individually, but the SNR was not sufficient to reliably measure $H\gamma$ at each spaxel in order to determine the localized extinction. However, due to the high foreground extinction the uncertainty in using global average extinction corrections is reduced compared to environments with a high amount of internal extinction.

3.3. Star Formation Rate Indicators

Our high resolution observations cover the $H\beta$ and [OIII]5007Å emission lines, both of which can be used as SFR tracers. Kennicutt (1992) and Moustakas et al. (2006) investigate the accuracy of these emission lines as SFR diagnostics and provide a detailed description of their advantages and disadvantages. Both determine the $H\alpha$ luminosity to be the more reliable SFR indicator, but unfortunately this lies beyond the wavelength coverage of KCWI. We provide here a brief description of the method of calculating SFR from each of the observed emission lines.

3.3.1. *Hβ*

In order to determine the SFR from the extinction corrected Hβ flux we first convert to equivalent Hα luminosity based on the Balmer decrement and then use the calibration of Murphy et al. (2011):

$$SFR = 5.37 \times 10^{-42} L_{\mathrm{H}\alpha} \qquad (2)$$

This calibration is based solar metallicity and a Kroupa (2001) IMF. It is updated from the calibration of Kennicutt (1998); Moustakas et al. (2006) which make use of a Salpeter (1955) IMF.

3.3.2. *[O*III*]5007Å*

Moustakas et al. (2006) uses their sample of SDSS star-forming galaxy spectra to explore the uncertainties present when using [OIII]5007Å to calculate SFR. They find a significant amount of scatter when comparing the luminosity of [OIII] to the Hα derived SFR, resulting in a factor of 3-4 uncertainty which they attribute to variation in chemical abundance and excitation. However, for a single galaxy like IC 10, and particularly for H II regions in the central starburst, we would not expect the same level of variation in these parameters as would be present in a sample of unique galaxies. Further, previous studies have used the [OIII]5007Å, flux to estimate SFR when Balmer line measurements were not present by assuming an [OIII]5007Å/Hα ratio of unity (Teplitz et al. 2000).

We investigate substituting the extinction corrected [OIII]5007Å luminosity for $L_{\mathrm{H}\alpha}$ in Equation 2 to estimate the SFR in the H II regions of IC 10, beginning with the same factor of $L_{\mathrm{[OIII]}}/L_{\mathrm{H}\alpha} = 1$ as Teplitz et al. (2000). This is compared to the Hβ derived SFR in Figure 6 to determine if the two SFR estimates are correlated and if the coefficient of 1 between $L_{\mathrm{[OIII]}}$ and $L_{\mathrm{H}\alpha}$ provides the best match. We find that there is good agreement between the two methods with an average $SFR_{\mathrm{[OIII]5007}}/SFR_{\mathrm{H}\beta} = 0.9$, though this ratio drops to $SFR_{\mathrm{[OIII]5007}}/SFR_{\mathrm{H}\beta} = 0.63$ in the faintest 1/3 of the H II regions. Since these are well matched overall in this sample, the higher signal-to-noise ratio [OIII]5007Å line will be used in the remainder of the analysis allowing for the identification of fainter star-forming regions. We checked whether the apparent lower $SFR_{\mathrm{[OIII]}}/SFR_{\mathrm{H}\beta}$ ratio in the faintest regions would introduce a bias in the results of the following sections by underestimating $L_{\mathrm{H}\alpha}$. This was not found to have a significant impact on the results and conclusions in the remainder of this paper with the potential differences being captured in the existing uncertainties. We therefore report only measurement uncertainties on quantities like SFR which rely on $L_{\mathrm{[OIII]}}$ as a proxy for $L_{\mathrm{H}\alpha}$ and proceed

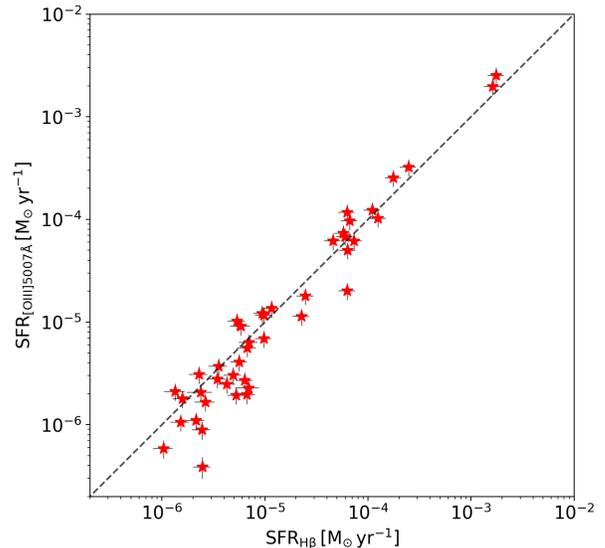with $L_{\mathrm{[OIII]}}/L_{\mathrm{H}\alpha} = 1$ for the full sample of IC 10 H II regions for consistency with previous studies.

Figure 6. Comparison of the SFR determined from Hβ and [OIII]5007Å. The dashed black line denotes the one-to-one line. Given an average $SFR_{\mathrm{[OIII]5007}}/SFR_{\mathrm{H}\beta} = 0.9$, the $SFR_{\mathrm{[OIII]5007}}$ does, on average, provide a good match to the more commonly used $SFR_{\mathrm{H}\beta}$.

3.3.3. *Low SFR H II Regions*

As can be seen in Figure 6, many of the identified H II regions in IC 10 have very low SFR. The rate of production of ionizing photons for a single $18M_{\odot}$ O9 star is $Q = 10^{47.90} \mathrm{s}^{-1}$ (Martins et al. 2005). Assuming Case B recombination this results in an expected $L_{\mathrm{H}\alpha} \approx 10^{36} \mathrm{erg \, s}^{-1}$. In this sample of IC 10 H II regions, 23/46 of the identified regions have luminosities less than this, indicating that the primary ionization source is a less massive star or cluster. There are a limited number of extragalactic surveys which to compare to in this low luminosity regime as the spatial resolution needed to differentiate these compact sources necessitates nearby objects as well as the sensitivity to detect low luminosities. The identification of IC 10's many H II regions by Hodge & Lee (1990) in Hα imaging survey does get to this regime as well. They also find some regions in which they attribute the ionization to a single late B or early A type star. The same regime of single star ionization is reached by Hodge et al. (1989) in NGC6822 though they note that some of the regions with low surface brightness may instead be diffuse emission rather than the H II regions they are identified as.

Within the Milky Way a number of studies of compact and ultra-compact H II regions have been conducted which fall into this category of ionization by

a single intermediate mass star at radio and infrared wavelengths. Lundquist et al. (2014) studied four intermediate mass star forming regions identified in the *Infrared Astronomical Satellite (IRAS)* Point Source Catalog and *Wide-field Infrared Survey Explorer (WISE)* images which they determined were powered by low mass clusters with mid-B stars as the most massive components and therefore the dominant source of ionizing photons. Over 900 so-called "yellowball" regions, compact H II regions sometimes ionized by a single B type star were identified by citizen scientists as part of the Milky Way Project (Kerton et al. 2015). The yellowballs regions show spatially coincident 8 and $24\mu m$ fluxes, which the authors attribute to the early stages of the H II region evolution. As part of HRDS, Armentrout et al. (2021) identify single star H II regions with *WISE* and the Very Large Array (VLA). They find that these single star regions have similar morphologies as their more luminous counterparts and can be powered by a single B2 or earlier spectral type star.

To determine the likely stellar type for the ionizing star in IC 10's H II regions, we compare the observed luminosity to models of the number of Lyman continuum photons produced by a given stellar type. For consistent comparison with the Armentrout et al. (2021) Milky Way study we use the same stellar models for the number of ionizing photons produced by a single star, Martins et al. (2005) for O type stars and Smith et al. (2002) for B type stars. The minimum number of ionizing photons required to power a given H II region is given by:

$$Q_{\mathrm{req}} = 7.31 \times 10^{11} L_{\mathrm{H}\alpha} \qquad (3)$$

under case B recombination (Osterbrock & Ferland 2006). The lowest luminosity region identified in IC 10 can be produced by ionization from a B0.5 star, with 10 H II regions potentially being produced by ionization from a single B star. Forty-four of the identified H II regions have luminosities which can be produced by a single star, while the remaining two would require an ionizing photon production rate equivalent to at least six O3 stars. The number of IC 10 H II regions that could be produced by ionization from a single star of each spectral type is shown in Figure 7.

3.4. Mass

The mass for each H II region is estimated based on the assumption that the H II regions are approximately spherical making the gas mass simply a function of the volume and density:

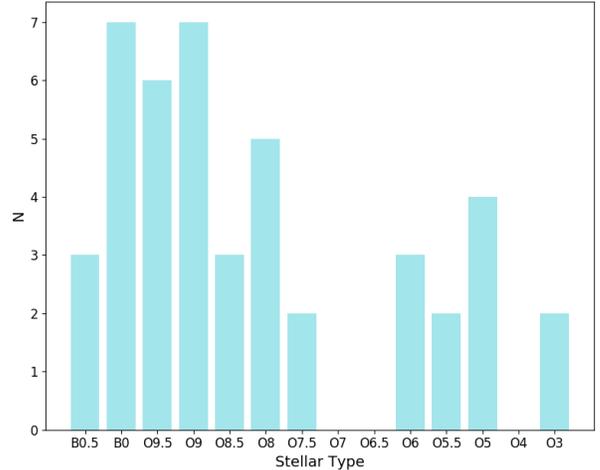$$M_{\mathrm{HII}} = \frac{4}{3}\pi r^3 n_{\mathrm{h}} m_{\mathrm{h}} \qquad (4)$$

Figure 7. Distribution of the potential central ionizing source for each H II region. The stellar type identified here is determined by the minimum number of ionizing photons which can produce the observed luminosity. In the case of a single star providing the dominant source of ionization, each IC 10 H II region requires at least a B0.5 star.

where r is the H II region radius and m_{h} is the mass of a hydrogen atom. We cannot directly measure the number density of hydrogen, n_{h}, in our KCWI spectra, but we can estimate it via the Strömgren sphere approximation; the assumption that the gas is fully ionized and therefore the measured luminosity directly measures the amount of hydrogen gas present:

$$n_{\mathrm{h}} = \sqrt{\frac{3 L_{\mathrm{H}\alpha} \lambda_{\mathrm{H}\alpha}}{4\pi h c \alpha_{\mathrm{B}} r^3}} \qquad (5)$$

where $\lambda_{\mathrm{H}\alpha}$ is the wavelength of Hα, h is Planck's constant, c is the speed of light, and α_B is the Case B recombination coefficient.

Combining these two equations we can solve for the mass of ionized hydrogen gas in each H II region. The resulting masses are shown in the histogram of Figure 8 with a median region mass for the sample $\sim 56\,\mathrm{M}_\odot$ and a total $\mathrm{M_{HII}} \sim 2 \times 10^4\,\mathrm{M}_\odot$ residing in the identified H II regions. We will compare this to estimates of the mass based on the measured H II region kinematics in Section 3.5.3.

The stellar mass of each region is estimated by integrating the IMF over the full mass range from $0.1\mathrm{M}_\odot$ to $100\mathrm{M}_\odot$ following the method laid out in Relaño et al. (2005). We summarize the method here but refer the reader to Relaño et al. (2005) for a more detailed discussion.

The total stellar mass with the previously stated upper and lower bounds is defined as:

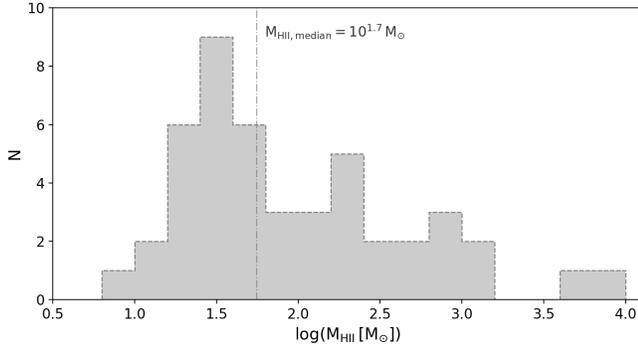$$M_* = \int_{0.1M_\odot}^{100M_\odot} m\Phi(m)dm \qquad (6)$$

Figure 8. Histogram of the H II region ionized gas masses, $M_{\rm HII}$, estimated from the Strömgren sphere approximation and the measured size and luminosity.

where $\Phi(m) = Am^{-2.3}$ for a Kroupa (2001) IMF. In order to perform the integration, the normalization factor, A, needs to be determined. This is done by estimating the stellar mass over a smaller range of stellar types. A first order estimate of M_* is determined by calculating a required number of O5 stars needed to produce the measured H II region luminosity and multiplying by the mass of an O5 star ($49.53\,M_\odot$). This is then substituted into Equation 6 with the upper and lower limits of integration replaced by the masses of an O3 ($55.3\,M_\odot$) and O9 ($22.1\,M_\odot$) star, respectively. The normalization factor, A, can then be solved for and the IMF can be integrated over the full mass range to give a more accurate estimate of M_*. For the low mass H II regions of IC 10 where we find luminosities consistent with ionization by a single early B star, integrating over the full IMF is somewhat uncertain. To address this, we include an estimated 30% systematic uncertainty on M_* in addition to the propagated uncertainty from the measured luminosity.

For IC 10's H II regions we find a mean $M_* \sim 400\,M_\odot$ from this method with a significantly lower median $M_* \sim 18\,M_\odot$. The large difference in the mean and median masses is due in part to a number of very low M_* estimates for low luminosity regions in which the assumption of a fully sampled IMF is less reliable. The

estimates of $M_{\rm HII}$ and M_* for each H II region are shown in Figure 9, with $M_* \sim 0.3 \times M_{\rm HII}$ on average.

3.5. *Kinematics*

As discussed in Section 3.2, we fit a Gaussian to each emission line in the integrated region spectra to determine the velocity shift and dispersion in each detected H II region. Due to the higher SNR of the [OIII]5007Å line, we will report the values from this fit here, though the trends are the same regardless of emission line used. Previous studies of ionized gas in giant H II regions find a systematic difference in linewidths measured from Hα or Hβ and [OIII], with [OIII] measurements giving a $\sim 2\,{\rm km\,s^{-1}}$ underestimate of the dispersion, σ (e.g., Bresolin et al. 2020). After correcting for thermal broadening of both lines, we do not observe such an offset in the spectra of IC 10's H II regions indicating that turbulence is likely the dominant source of the line broadening (O'Dell et al. 2017). We will therefore proceed with the [OIII]5007Å measurements to trace the kinematics of the ionized gas. The fitted kinematic properties for [OIII]5007Å are shown in Table 4 with properties for [OIII]4959Å and Hβ included in a machine readable version of the table online. The average velocity shift is -12±12 km s^{-1} relative to the systemic velocity of IC 10 with typical velocity dispersions of 16±8 km s^{-1}.

Each of the H II region DIG subtracted spectra are shifted to a common velocity based on the mean of the Gaussian fit to [OIII]5007Å, normalized to the [OIII]5007Å peak flux, and stacked to generate a composite spectrum as shown in Figure 10. Other than removal of the DIG, no other corrections are applied to the spectra before stacking. This reveals a lower luminosity broad component to the [OIII]5007Å line too faint to be detected in the individual H II region spectra or the lower SNR Hβ line. The broad component has a velocity dispersion $\sigma = 36.6$ km s^{-1} and shows only a 2.4km s^{-1} velocity shift relative to the narrow component. Its peak is only 21% of the narrow component peak, but contributes $\sim$37% of the integrated flux. The double Gaussian fit is shown in Figure 10 with the stacked spectrum.

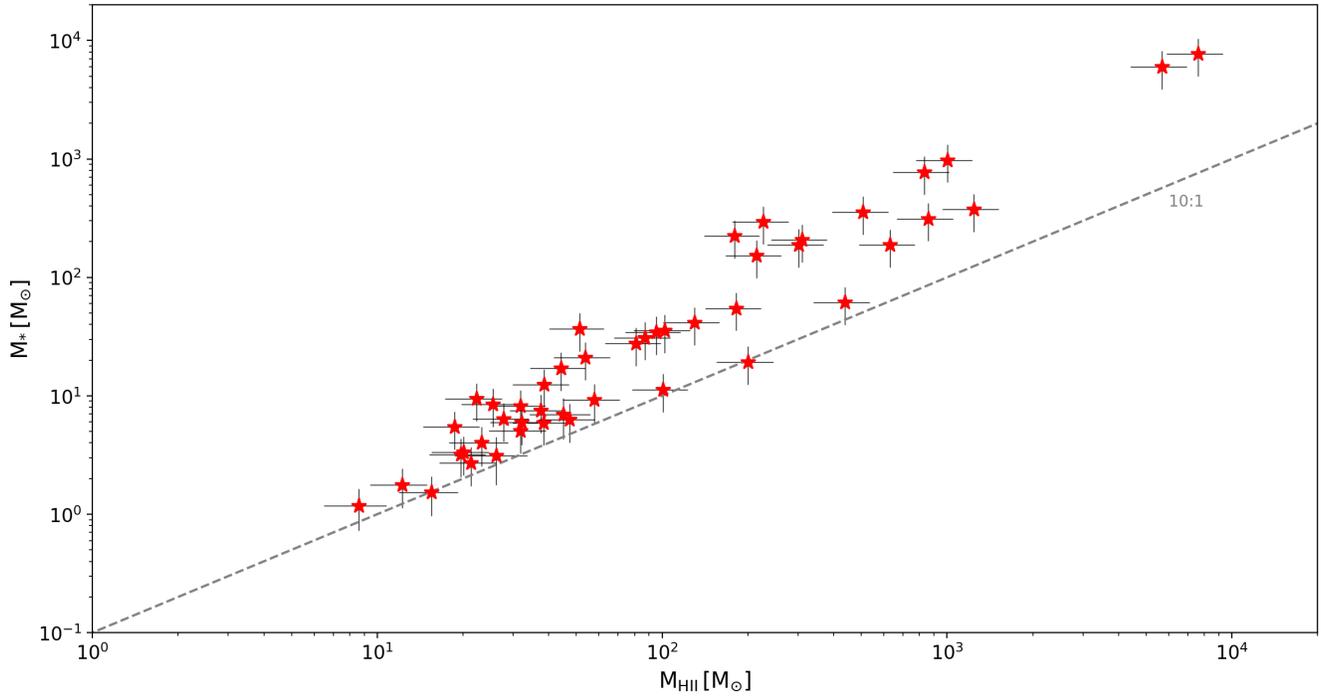**Figure 9.** Comparison of the estimated M_{HII} and M_* for each IC 10 H II region identified in the KCWI data. On average $M_* \sim 30\% \, M_{HII}$.
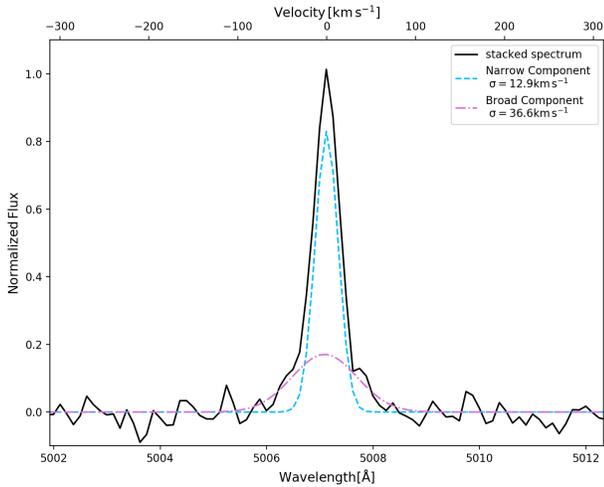

Figure 10. Stacked spectrum from each identified H II region (black). Each individual spectrum is normalized to the [OIII]5007Å flux before stacking to investigate the shape of the emission lines. This reveals a faint broad component at [OIII]5007Å that could not be detected in the individual regions. Fits to the broad and narrow components of the [OIII]5007Å line are shown in magenta and cyan, respectively.

Table 4. H II Region Properties (small slicer, R∼18,000)

Region	radius (pc)	$\Delta V_{[\mathrm{OIII}]5007}$ (km s⁻¹)	$\sigma_{[\mathrm{OIII}]5007}$ (km s⁻¹)	$L_{[\mathrm{OIII}]5007}$ (10³⁵ erg s⁻¹)	SFR (10⁻⁶ M$_\odot$ yr⁻¹)	M_{HII} (M$_\odot$)	τ_{cr} (10⁶ yrs)
G16	2.60 ± 0.22	-8.73 ± 1.77	14.52 ± 0.18	7.62 ± 1.43	4.09 ± 0.77	38.48 ± 8.59	0.18 ± 0.05
G17	2.11 ± 0.18	5.62 ± 1.57	14.52 ± 0.28	3.35 ± 0.63	1.80 ± 0.34	18.65 ± 4.19	0.14 ± 0.04
H16a*	10.32 ± 0.87	-11.98 ± 1.61	17.02 ± 0.00	4741.00 ± 889.10	2546.00 ± 477.40	7591.80 ± 1690.19	0.59 ± 0.17
H16b*	2.95 ± 0.25	-11.52 ± 1.50	15.15 ± 0.08	181.00 ± 33.95	97.20 ± 18.23	226.71 ± 50.65	0.19 ± 0.06
H17a*	5.08 ± 0.43	-4.43 ± 2.18	15.85 ± 0.01	476.90 ± 89.41	256.10 ± 48.01	831.57 ± 185.60	0.31 ± 0.09
H17b*	4.14 ± 0.35	-0.44 ± 1.98	11.83 ± 0.01	115.60 ± 21.68	62.08 ± 11.64	301.21 ± 67.18	0.34 ± 0.10
H17c*	3.54 ± 0.30	-3.46 ± 5.64	12.95 ± 0.03	93.73 ± 17.58	50.33 ± 9.44	214.45 ± 47.91	0.27 ± 0.08
H18a*	4.74 ± 0.40	-14.98 ± 1.52	16.84 ± 0.03	218.70 ± 41.01	117.40 ± 22.02	507.55 ± 113.07	0.28 ± 0.08
H18b	4.08 ± 0.34	-38.16 ± 1.67	11.83 ± 0.01	127.50 ± 23.90	68.47 ± 12.83	309.48 ± 68.38	0.34 ± 0.10
H18c	2.19 ± 0.18	-31.40 ± 1.72	11.75 ± 0.03	22.63 ± 4.24	12.15 ± 2.28	51.27 ± 11.23	0.18 ± 0.05
H18d	3.38 ± 0.28	-18.39 ± 1.50	13.70 ± 0.04	21.16 ± 3.97	11.36 ± 2.13	95.07 ± 20.93	0.24 ± 0.07
H18e	2.72 ± 0.23	-15.82 ± 1.50	11.93 ± 0.08	12.89 ± 2.42	6.92 ± 1.30	53.56 ± 11.95	0.22 ± 0.06
I16a	2.60 ± 0.22	-6.80 ± 1.51	12.18 ± 0.55	1.97 ± 0.38	1.06 ± 0.20	19.59 ± 4.40	0.21 ± 0.06
I16b	2.31 ± 0.19	-1.66 ± 1.51	16.64 ± 1.53	1.09 ± 0.22	0.59 ± 0.12	12.20 ± 2.76	0.14 ± 0.04
I17a*	2.56 ± 0.21	7.85 ± 1.68	17.05 ± 0.57	10.48 ± 1.99	5.63 ± 1.07	44.10 ± 9.69	0.15 ± 0.04
I17b	3.02 ± 0.25	-3.88 ± 1.50	15.08 ± 0.43	4.62 ± 0.87	2.48 ± 0.47	37.50 ± 8.28	0.20 ± 0.06
I17c*	2.10 ± 0.18	-2.29 ± 1.50	36.14 ± 6.23	0.73 ± 0.17	0.39 ± 0.09	8.63 ± 2.14	0.06 ± 0.02
I18*	7.02 ± 0.59	-63.67 ± 1.65	15.16 ± 0.06	192.30 ± 36.07	103.30 ± 19.37	857.80 ± 190.61	0.45 ± 0.13
I19a	3.51 ± 0.30	-22.49 ± 1.51	32.39 ± 0.23	21.85 ± 4.10	11.73 ± 2.20	102.23 ± 22.97	0.11 ± 0.03
I19b*	3.30 ± 0.28	-29.09 ± 1.64	19.26 ± 0.13	19.07 ± 3.58	10.24 ± 1.92	87.06 ± 19.47	0.17 ± 0.05
J15	2.71 ± 0.23	-1.79 ± 1.51	53.08 ± 6.37	2.46 ± 0.52	1.32 ± 0.28	23.27 ± 5.46	0.05 ± 0.02
J16a	7.72 ± 0.65	-6.02 ± 1.50	11.91 ± 0.47	37.66 ± 7.13	20.22 ± 3.83	437.78 ± 97.70	0.63 ± 0.19
J16b	4.46 ± 0.37	-9.92 ± 1.76	9.88 ± 0.17	33.71 ± 6.35	18.10 ± 3.41	181.87 ± 40.13	0.44 ± 0.13
J16c	2.24 ± 0.19	-20.49 ± 1.56	10.21 ± 0.16	5.21 ± 0.98	2.80 ± 0.53	25.45 ± 5.69	0.21 ± 0.06
J16d	3.74 ± 0.31	-15.46 ± 1.53	22.29 ± 1.51	3.87 ± 0.76	2.08 ± 0.41	47.33 ± 10.59	0.16 ± 0.05
J17a	3.76 ± 0.32	-12.90 ± 1.50	15.70 ± 0.47	5.67 ± 1.07	3.05 ± 0.58	57.76 ± 12.98	0.23 ± 0.07
J17b	3.50 ± 0.29	0.80 ± 1.50	21.47 ± 3.60	4.27 ± 1.00	2.29 ± 0.53	44.98 ± 10.84	0.16 ± 0.05

Table 4 *continued*

Table 4 (*continued*)

Region	radius	$\Delta V_{\mathrm{[OIII]5007}}$	$\sigma_{\mathrm{[OIII]5007}}$	$L_{\mathrm{[OIII]5007}}$	SFR	M_{HII}	τ_{cr}
	(pc)	(km s^{-1})	(km s^{-1})	(10^{35} erg s^{-1})	(10^{-6} M$_\odot$ yr^{-1})	(M$_\odot$)	(10^6 yrs)
J17c	2.94 ± 0.25	1.89 ± 1.52	14.66 ± 0.92	3.68 ± 0.72	1.98 ± 0.39	32.16 ± 7.32	0.20 ± 0.06
J17d*	3.09 ± 0.26	-2.98 ± 1.50	13.66 ± 0.76	3.11 ± 0.60	1.67 ± 0.32	31.85 ± 7.18	0.22 ± 0.07
J17e	2.61 ± 0.22	4.98 ± 1.50	22.06 ± 1.57	2.05 ± 0.40	1.10 ± 0.22	20.06 ± 4.55	0.12 ± 0.03
J17f	3.18 ± 0.27	-16.69 ± 3.92	18.31 ± 5.39	1.92 ± 0.60	1.03 ± 0.32	26.13 ± 7.45	0.17 ± 0.07
J17g	2.91 ± 0.24	-33.59 ± 6.47	12.12 ± 0.91	1.66 ± 0.33	0.89 ± 0.18	21.28 ± 4.77	0.23 ± 0.07
K16	5.10 ± 0.43	-26.38 ± 1.55	12.79 ± 0.32	6.91 ± 1.31	3.71 ± 0.70	100.70 ± 22.48	0.39 ± 0.11
L11	5.32 ± 0.45	-14.92 ± 3.02	10.21 ± 0.01	601.40 ± 112.80	323.00 ± 60.57	1000.78 ± 223.30	0.51 ± 0.15
M11*	2.77 ± 0.23	-19.93 ± 1.51	11.42 ± 0.02	137.30 ± 25.75	73.73 ± 13.83	179.66 ± 39.61	0.24 ± 0.07
M12*	9.24 ± 0.78	-45.03 ± 1.57	14.88 ± 0.00	3693.00 ± 692.40	1983.00 ± 371.80	5676.59 ± 1264.79	0.61 ± 0.18
M14	6.74 ± 0.57	-17.98 ± 1.60	25.23 ± 0.95	11.84 ± 2.25	6.36 ± 1.21	200.24 ± 44.91	0.26 ± 0.08
M16a*	8.45 ± 0.71	-12.73 ± 1.66	10.06 ± 0.02	230.30 ± 43.19	123.70 ± 23.19	1239.72 ± 275.42	0.82 ± 0.24
M16b	2.62 ± 0.22	-9.04 ± 1.50	9.98 ± 0.15	5.06 ± 0.95	2.72 ± 0.51	31.73 ± 7.05	0.26 ± 0.07
M16c	2.61 ± 0.22	-13.06 ± 1.50	8.91 ± 0.21	3.92 ± 0.74	2.11 ± 0.40	27.78 ± 6.20	0.29 ± 0.08
M16d	3.33 ± 0.28	-3.86 ± 1.50	14.12 ± 0.38	3.61 ± 0.68	1.94 ± 0.37	38.39 ± 8.55	0.23 ± 0.07
N12a*	6.79 ± 0.57	-27.95 ± 1.53	12.18 ± 0.04	115.20 ± 21.61	61.86 ± 11.60	631.57 ± 140.24	0.55 ± 0.16
N12b*	1.98 ± 0.17	-24.54 ± 2.13	15.93 ± 0.30	5.78 ± 1.09	3.10 ± 0.58	22.28 ± 5.03	0.12 ± 0.04
N13a	3.91 ± 0.33	-21.74 ± 1.50	11.97 ± 0.08	25.42 ± 4.77	13.65 ± 2.56	129.64 ± 28.89	0.32 ± 0.09
N13b*	3.26 ± 0.27	-20.63 ± 1.65	12.80 ± 0.28	17.06 ± 3.22	9.16 ± 1.73	80.85 ± 17.84	0.25 ± 0.07
N15	2.85 ± 0.24	-6.88 ± 1.58	14.88 ± 1.77	0.94 ± 0.20	0.50 ± 0.11	15.52 ± 3.64	0.19 ± 0.06

NOTE—Properties of the [OIII]5007Å emission line for HII regions in the small slicer, R∼18,000 observing mode. Spectral properties are determined by fitting a single Gaussian model to the emission line. Regions with elevated σ in the surrounding gas are identified with a *. The properties of the [OIII]4959Å and Hβ lines are available in the machine-readable version of this table online.

3.5.1. *Resolved Kinematics*

In addition to spectra integrated over IC 10's H II regions, we investigate the resolved kinematic properties of the ionized gas at each spaxel. The velocity shift relative to the systemic velocity ($v_{sys} = -348 km s^{-1}$), ΔV, and dispersion, σ, are measured from single Gaussian fits to [OIII]5007Å and Hβ emission lines. The properties determined from the [OIII]5007Å line in spaxels inside H II regions are used to illustrate the three dimensional structure of the identified H II regions in Figure 11. Additionally, maps of ΔV and σ at each spaxel in the FoV with SNR>2 for both the [OIII]5007Å and Hβ fits are shown in Figures 12 & 13. Thumbnail flux and kinematic maps for each H II region are included in Appendix D with an example for region G16 in Figure 14. These maps show interesting kinematic trends between gas inside and outside the H II regions. The velocity shift shows clear differences between gas residing in the population of H II regions (blue-shifted) and the diffuse gas not associated with a particular region (redshifted). This is illustrated in both the map of Figure 12 and the distributions of Figure 15a which shows a much broader distribution of ΔV in spaxels outside the H II regions. This is not surprising as less structure would be expected in the kinematics of this gas than that which is associated with a coherent H II region.

Furthermore, it can be seen in the maps of Figure 14 and Appendix D that the velocity dispersion is highest at many of the H II region borders, particularly those that reside in larger complexes. In fact, 37% of the identified H II regions, identified with a * in Table 4, show elevated velocity dispersions at one or more of their edges which could be indicative of outflowing gas. The distributions of measured σ at each spaxel inside and outside of the H II region boundaries are shown in Figure 15b for further comparison. The mean σ for spaxels inside and outside H II regions is quite similar (13 and 14 km s^{-1}, respectively), but the width of the distribution is twice as large for spaxels outside the region boundaries. We investigate the possibility of shocked gas at the H II region boundaries by evaluating the [OIII]5007Å/Hβ ratio. An area with an elevated line ratio may indicate the presence of shocked gas. To ensure this ratio is evaluated over the same physical gas column, we define a fixed velocity shift and width for [OIII] and Hβ in each spaxel determined from the Gaussian fit to the lower SNR Hβ line. Figure 16 shows the map of this line ratio along with contours of elevated velocity dispersion, and as can be seen, the spaxels which show the highest $\log\left([OIII]5007Å/H\beta\right)$ also correspond to the areas of elevated velocity dispersion. This result indicates that the elevated velocity dispersion observed at the H II region borders is due to shocked gas.

3.5.2. *Region Rotation*

In order to classify the kinematic structure of the individual H II regions we generate ΔV maps centered on each region adjusted so the systemic shift of the H II region is 0 km s^{-1}(based on the mean of the Gaussian fit to the integrated region spectrum). For each region we designate whether it is rotating both visually and quantitatively. In order for a region to be considered rotating by eye it must have a bimodality of the velocity shift relative to the region's systemic velocity shift; meaning it must have one region of negative shift and one of positive shift. If for example, there is positively shifted gas surrounded by negatively shifted gas or viceversa we do not consider that to be ordered rotation. With this method we find 35% of regions to be rotating, which is likely a conservative estimate due to the strict visual criteria.

To assign a quantitative rotation criteria we fit the velocity gradient across the region at different position angles. For each position angle we generate a "fit quality factor" based on the reduced χ^2 combined with the steepness of the slope. The maximum value of the fit quality factor is taken to be the most probable rotation direction and magnitude for that region. If the slope is greater than a threshold value of 0.57 km s^{-1}pc^{-1} then the region is considered rotating. This threshold was determined by assuming an electron density, $n_e = 100 cm^{-3}$ and determining the mass contained within a region of radius 1pc. Assuming the gas is virialized we then determined the expected value of velocity dispersion and range of velocity shifts[2]. With this criteria we find 65% of H II regions to be rotating. More regions are classified as rotating using this method than the visual classification which in part is due to restricting our visual classification to regions which only have one transition between positive and negative velocity shifts rather than based only on the overall gradient. This restriction is then susceptible to bias from velocity shifts in a small number of pixels that may be outliers for the H II region, classifying regions as "not rotating" when they do in fact have underlying rotation. The quantitative method is also free from the inherent bias with all visual classification and is more easily extended to other samples and studies. Therefore we proceed with

---

[2] For an H II region with the average radius of this sample, r = 4 pc at $n_e = 100 cm^{-3}$, the resulting mass $M_{H II}$ 500M$_{\odot}$. This is larger than the average mass estimated in the previous section for IC 10's H II regions, but that simply results in a conservative threshold for rotation.
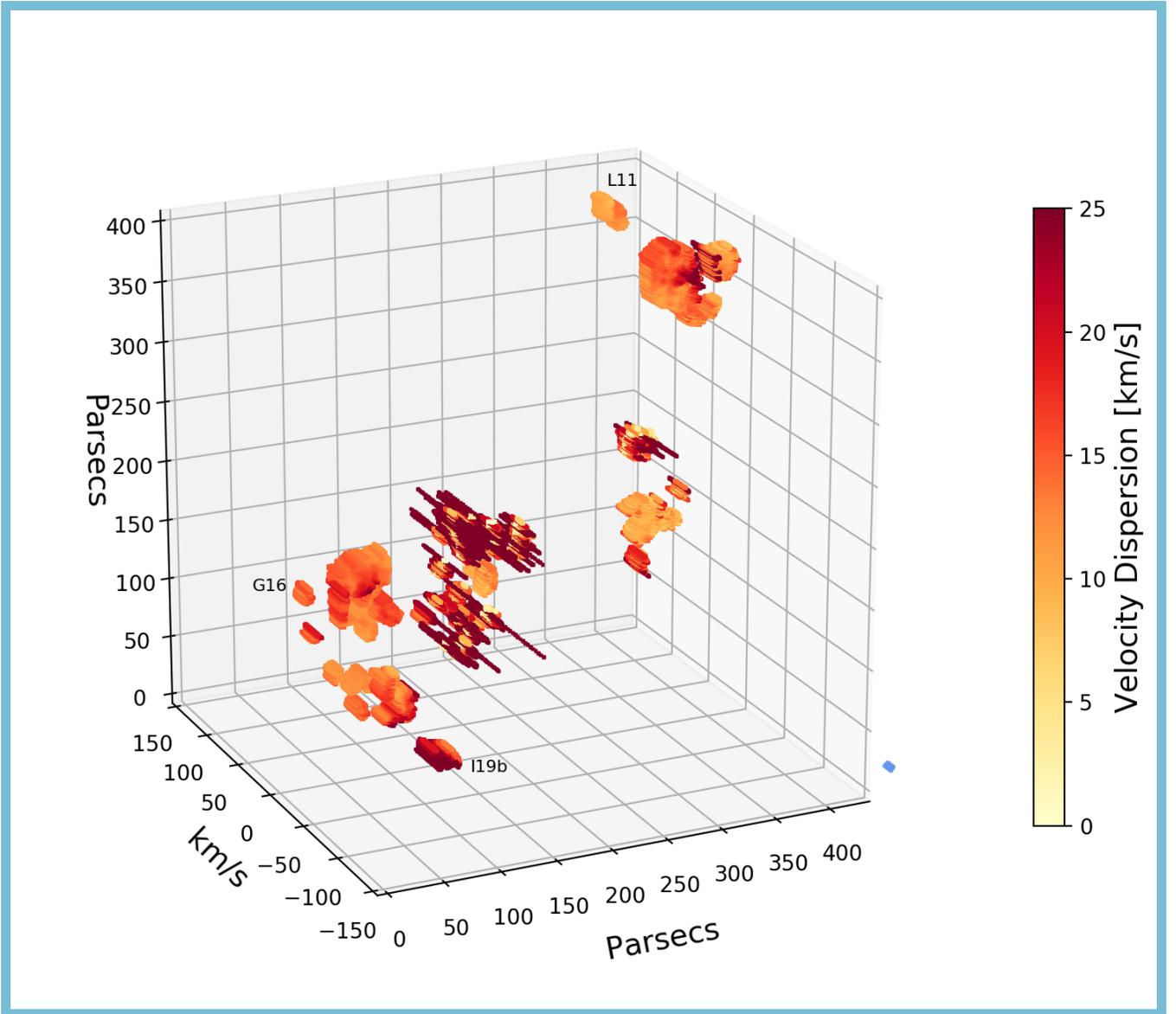
Figure 11. Three dimensional view of the 46 identified H II regions in the center of IC 10 based on Gaussian fits to [OIII]5007Å at each spaxel within the region contours. For each spaxel belonging to an identified H II region, the central velocity is set by the velocity shift relative to the systemic velocity of IC 10 and the depth by the velocity dispersion. The colormap also illustrates the measured velocity dispersion at each spaxel. The blue cylinder at the lower right represents a single spectral (depth) and spatial (width/height) resolution element. This figure is available online as an animation which rotates about the field of view.

the rotation classification of the quantitative method in further analysis.

3.5.3. *Virialization*

In addition to M_{HII}, we can also estimate the H II region masses based on the measured kinematics of the ionized gas by calculating the virial, M_{vir}, and enclosed, M_{encl}, masses. However, these rely on the assumption that the motion of the ionized gas is dominated by the self-gravity of the region.

For M_{vir} the region is assumed to be bound and we apply the virial theorem:

$$M_{vir} = \frac{5\sigma^2 r}{G} \qquad (7)$$

where the factor of 5 is a geometric factor representing the shape of the potential well for a spherical region. This results in a median $M_{vir} = 7.6 \times 10^5 \, M_{\odot}$, orders of magnitude greater than M_{HII}.

As a second method of estimating the H II region masses kinematically we calculate the enclosed mass,

(a) [OIII]5007Å

(b) Hβ
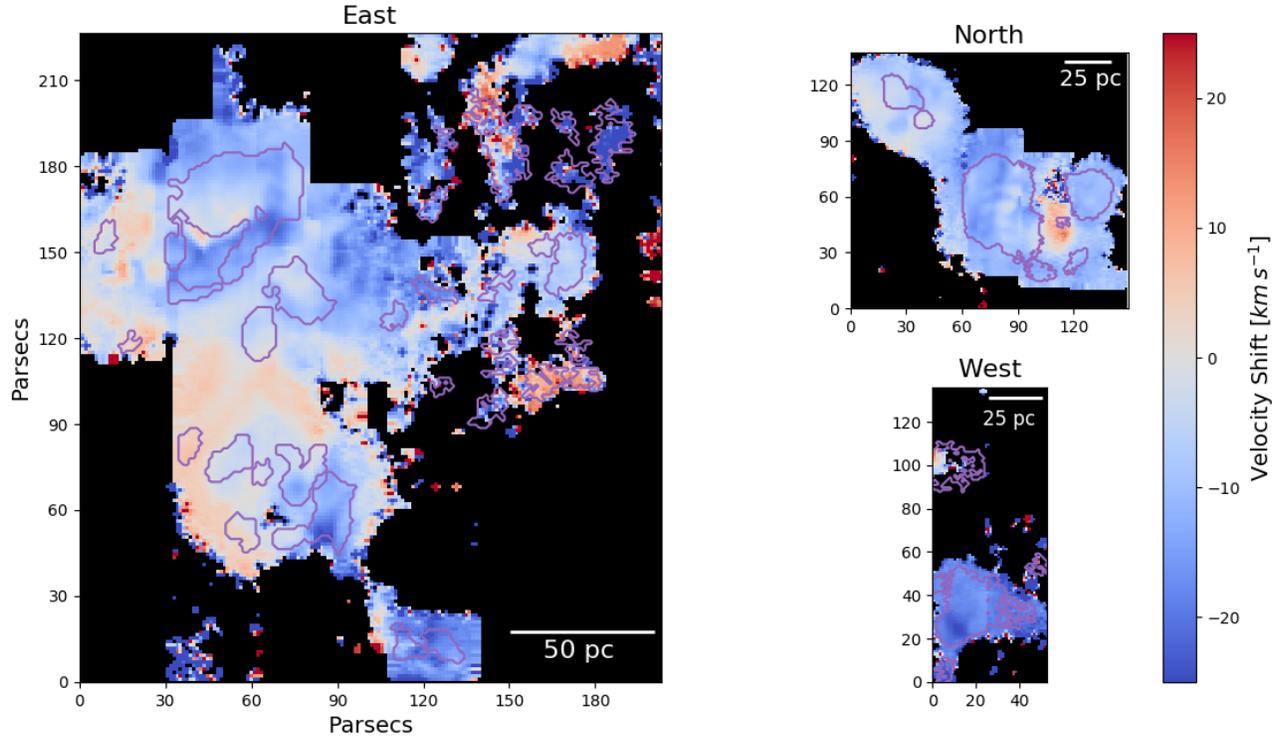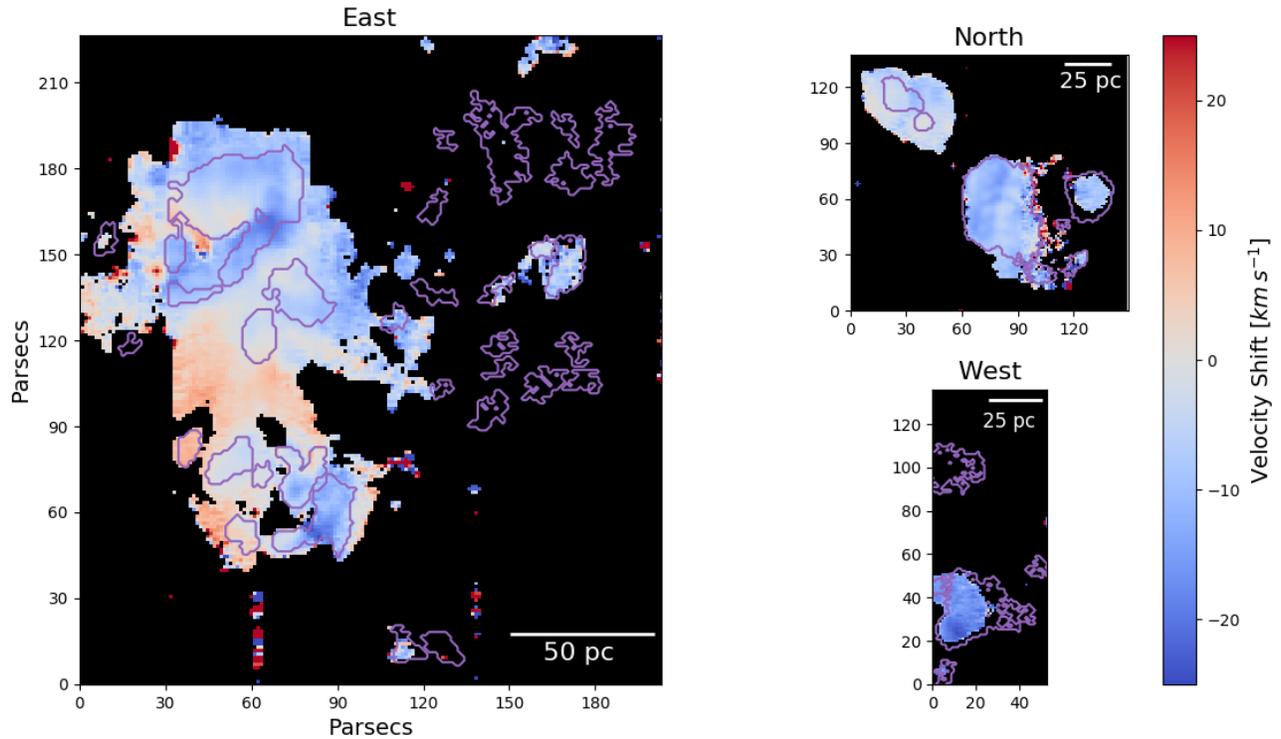
Figure 12. Maps of velocity shift of the ionized gas in IC 10 measured from Gaussian fits to the [OIII]5007Å (a) and Hβ (b) lines at each spaxel for the high resolution "small slicer, R~18,000" observing mode. Each map is divided into the "North", "West", and "East" regions of the observed field. The purple contours mark the edges of the most compact H II region structures found by `astrodendro`. Interestingly, these H II regions predominantly show gas which is blue-shifted relative to the systemic velocity of IC 10 while the surrounding diffuse gas more often shows red-shifted components. SNR >2 is required for these maps, with more spaxels falling below this cut in Hβ, but with the velocity fields matching when measured from either emission line where the SNR is high enough for comparison.

(a) [OIII]5007Å

(b) Hβ
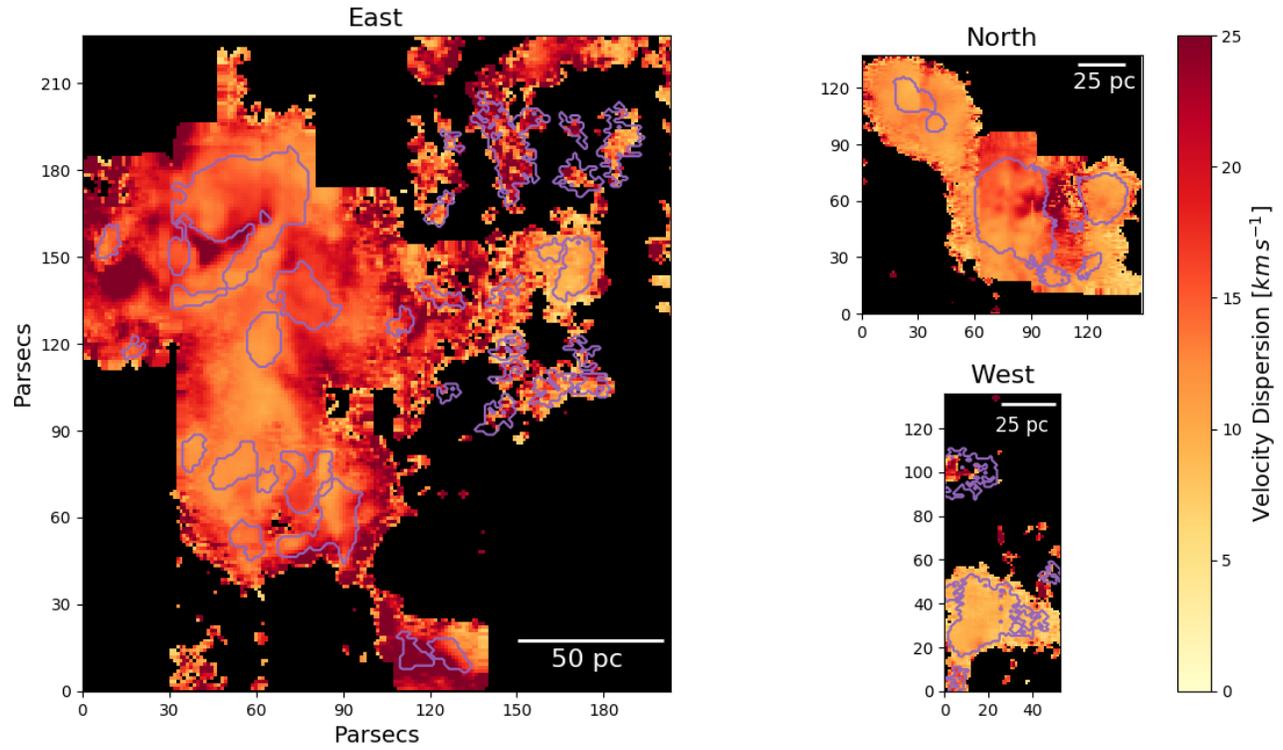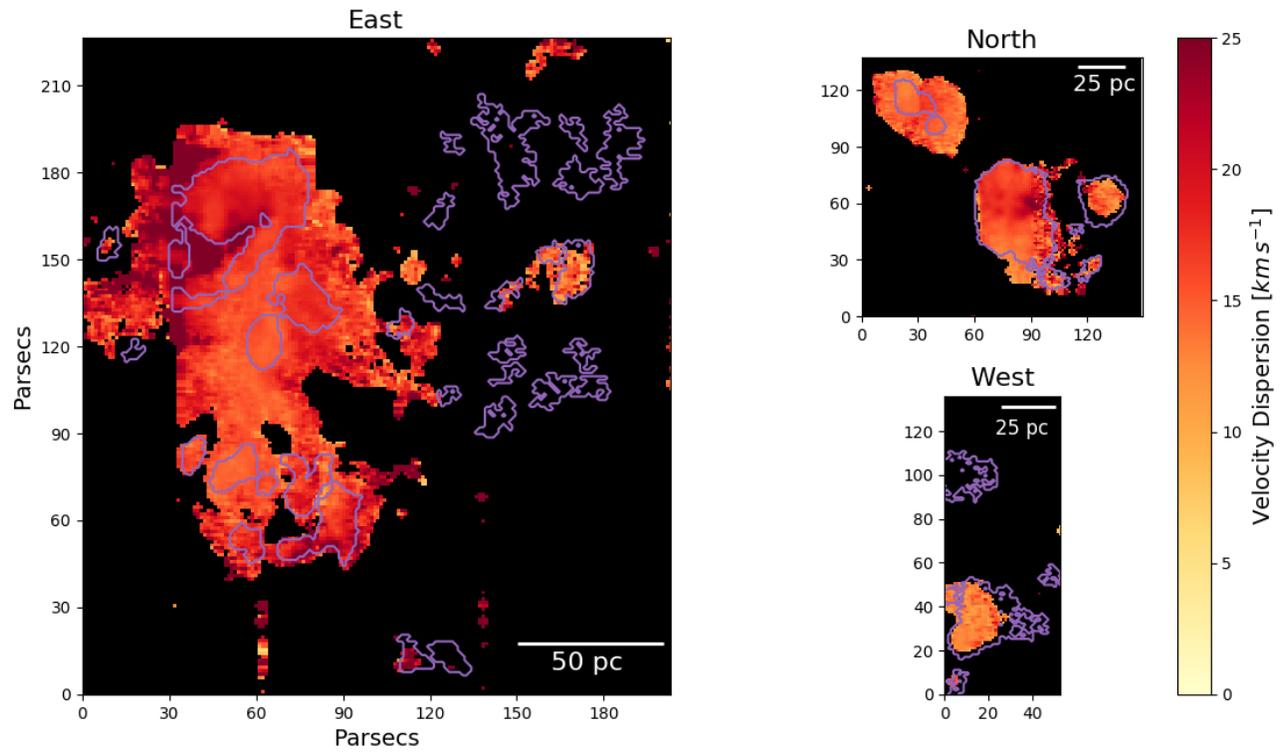
Figure 13. Maps of velocity dispersion of the ionized gas in IC 10 measured from Gaussian fits to the [OIII]5007Å (a) and Hβ (b) lines at each spaxel for the high resolution "small slicer, R~18,000" observing mode. Each map is divided into the "North", "West", and "East" regions of the observed field. The purple contours mark the edges of the most compact H II region structures found by `astrodendro`. SNR >2 is required for these maps, with more spaxels falling below this cut in Hβ, but with the velocity fields matching when measured from either emission line where the SNR is high enough for comparison. In particular note the elevated dispersion along the outer edges of some H II regions.

M$_{\rm encl}$, for regions that were determined to be rotating.

$$M_{\rm encl} = \frac{v_{\rm c}^2 r}{G} \qquad (8)$$

where $v_{\rm c}$ is the circular velocity determined from the measured velocity shift, v, at a distance, r, from the H II region center corrected for the inclination, i:

$$v_{\rm c} = v \, sin(i) \qquad (9)$$

Assuming a circular region and no preferred inclination relative to the direction of rotation, we take an average of $sin(i)$ between 0 and $\pi/2$, resulting in a factor of $\frac{\pi}{4}$. The median M$_{\rm encl}$ for rotating regions is $\sim 1.0 \times 10^4$ M$_{\odot}$, more than an order of magnitude less than M$_{\rm vir}$, but still significantly greater than M$_{\rm HII}$.

The more than 3 orders of magnitude discrepancy between M$_{\rm HII}$ or M$_{\rm encl}$ and M$_{\rm vir}$ implies that, on average, the H II regions are not in fact virialized and the use of the velocity dispersion is overestimating the gravitational potential. Furthermore, the measured rotational velocity is also overestimating the gravitational potential, indicating that rotation is not the dominant cause of the velocity gradient observed accross the H II regions. To explore this further we first investigate the virial parameter, $\alpha_{\rm vir} = \frac{5\sigma^2 {\rm r}}{{\rm GM}_{\rm gas}}$, of the H II regions. We determine $\alpha_{\rm vir}$ using the H II region radius following the $r_{1/2}^*$ definition and the velocity dispersion, σ measured from the Gaussian fit to the integrated spectrum. For M$_{\rm gas}$, we use M$_{\rm HII}$, assuming that the gas in the vicinity of the identified H II region is fully ionized. The resulting values for $\alpha_{\rm vir}$ are shown plotted as a function of L$_{\rm [OIII]5007}$ in Figure 17 with the resulting $\alpha_{\rm vir} \gg 1$, falling in the regime of H II regions which are not virialized.

Studies of H II regions have often investigated the relationship between the luminosity and velocity dispersion, the L $-$ σ relation, to study the the region dynamics. Rather than finding a correlation between these two properties for all H II regions, studies typically fit the upper envelope of the relationship defining the area of the correlation where H II regions in virial equilibrium would lie (e.g., Arsenault et al. 1990). We compare the identified H II regions in IC 10 to the relationships measured for the upper L $-$ σ envelope in three such studies (Zaragoza-Cardiel et al. 2015; Relaño et al. 2005; Rozas et al. 1998) as another test of virialization. As can be seen from this comparison in Figure 18, IC 10's H II regions fall below the envelope fits further supporting the conclusion that the H II regions are not virialized and the dynamics are dominated by sources of energy besides gravity.

The free-fall time estimate is a useful quantity for regions which are forming stars under simple gravitational collapse. We have shown that the H II regions of IC 10 are not virialized, however, and thus the free-fall time may not be the best characterization in this case. The crossing time, based on the measured velocity dispersion may provide a more useful characterization of the timescale relevant for an expanding H II region. The crossing time is defined as:

$$\tau_{\rm cr} = \frac{r}{\sigma} \qquad (10)$$

The average $\tau_{\rm cr} \sim 2 \times 10^5$ yrs for IC 10's H II regions.

3.5.4. *Energetics*

As outlined in the previous section, the H II regions identified in IC 10 are not virialized, and the velocity dispersions are therefore not a good estimate of the gravitational potential. To quantify the amount of dispersion due to sources other than gravitational motion we generate model spectra with only rotational motion included for those regions classified as rotating. For this simple model we sum individual Gaussian profiles at each pixel along the direction of rotation with the center set by the measured ΔV, and the width set only by the instrumental width, ~ 7.5km s^{-1}. The peak flux of each component of the sum is based on a simple Gaussian flux profile for the H II region. After each model pixel is summed the total flux is normalized by the measured [OIII]5007Å flux of the region for accurate comparison. These model spectra are then fit with a single Gaussian profile and the velocity dispersion compared to the measured value for the H II region. The non-rotational motion in the measured profile is defined as $\Delta\sigma = \sqrt{\sigma_{\rm meas}^2 - \sigma_{\rm mod}^2}$, the difference between measured and modeled. The distribution of $\Delta\sigma$ is shown in Figure 19 along with a cartoon illustrating the Gaussian components of the model spectrum. The average value for $\Delta\sigma$ is ~ 14km s^{-1}, similar to the sound speed expected in a typical H II region.

We checked the accuracy of this simple rotating H II region model using the software SHAPE (Steffen et al. 2011). SHAPE allows the user to generate a model with potentially complex geometry and kinematic structure. We use a spherical geometry with only rotational motion at the spatial and spectral resolution for each observation. We model this for 3 of our identified rotating H II regions (H18d, H18e, G16) and compare the velocity dispersion from the SHAPE model and simplified Gaussian sums. For region G16, we find that the SHAPE model produces a velocity dispersion 0.3 km s^{-1} greater than our model, in the other two the difference is less than 0.03 km s^{-1}. With measured spectra producing velocity dispersions ~ 14km s^{-1} greater than either model, this discrepancy is negligible. We therefore use the simple
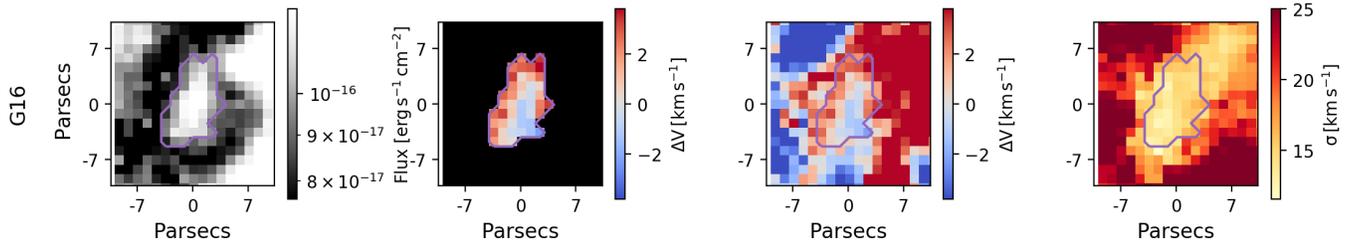
Figure 14. Thumbnail map of H II region G16 identified in our KCWI observations. The complete figure set (46 images) is available in the online journal. (Left): Flux maps of the surrounding area. (Center Left): Velocity shift of spaxels within the H II region relative to the systemic velocity of the region. (Center Right): Velocity shift of the H II region and the surrounding gas. (Left): Velocity dispersion within the H II region and the surrounding gas. Regions of elevated velocity dispersion may be indicative of outflowing gas, particularly when correlated with a velocity shift relative to the surrounding gas.
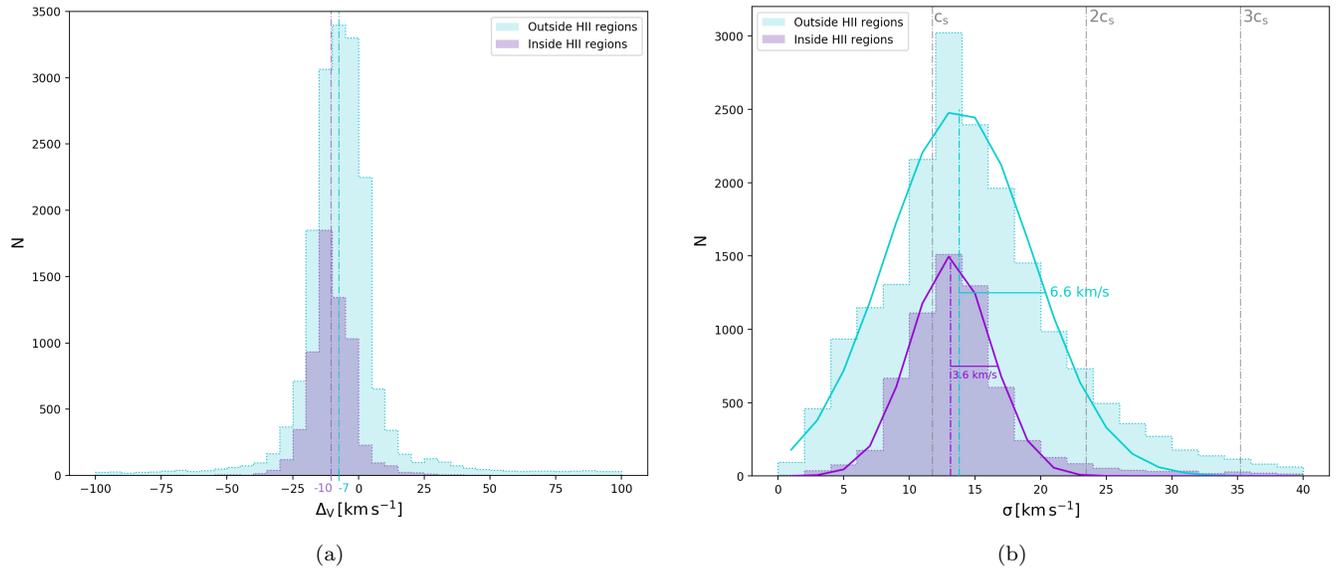
Figure 15. Distributions of kinematic properties derived from Gaussian fits to the [OIII]5007Å line at each spaxel. These distributions are seperated into spaxels which lie outside the H II region boundaries (purple) and inside (cyan). (a): Distribution of ΔV determined from the Gaussian mean relative to the systemic velocity of IC 10 (-348km s^{-1}). The median of each distribution is denoted with a dashed line, but it should be noted that the distributions are quite broad at the base, in particular for those spaxels which are not associated with an H II region. (b): Distribution of σ, the Gaussian standard deviation after subtraction of instrumental width. These distributions are more regularly distributed about their peaks than their ΔV counterparts and are therefore fit with Gaussians (solid lines). The mean of the Gaussian fits to the distributions are marked with dashed lines and are quite similar (13km s^{-1} for spaxels inside H II regions and 14km s^{-1} outside), but the width of the distribution outside the H II regions is twice as large as can be seen in the annotated standard deviation of the fitted distribution.

(a)

(b)
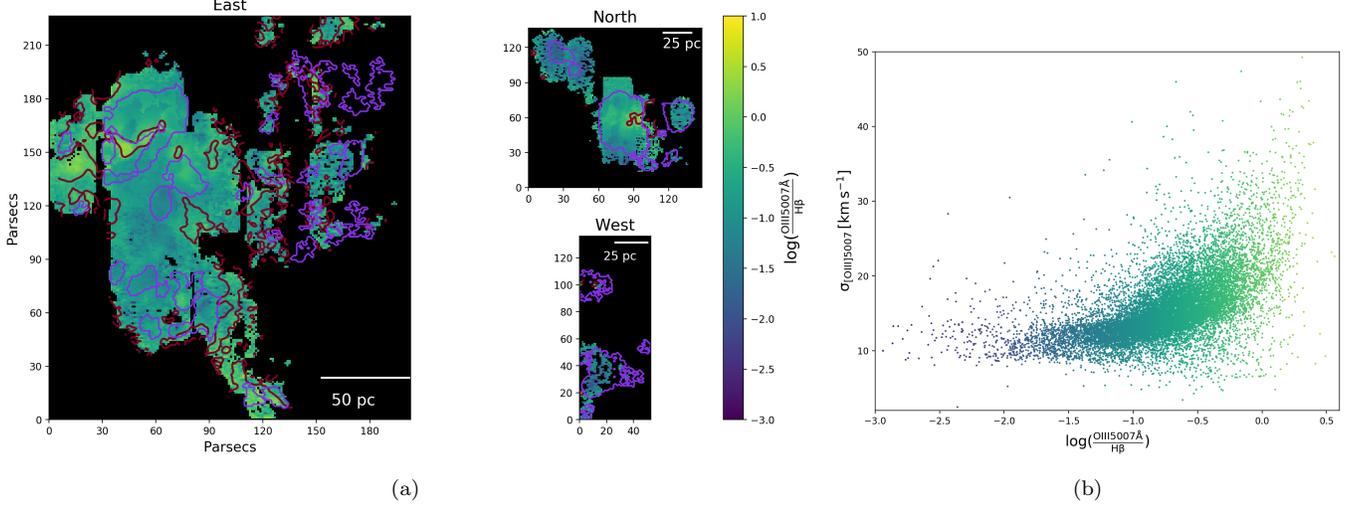
Figure 16. (a): Map of the [OIII]5007Å/Hβ ratio for spaxels with SNR>2 at the weaker Hβ line. As in Figure 3, the purple contours show the edges of the identified H II regions. The dark red contours show areas with velocity dispersion > 20 km s^{-1} as measured from the [OIII]5007Å line. (b): The [OIII]5007Å/Hβ ratio plotted against velocity dispersion for each spaxel with the same requirement that SNR$_{Hβ}$ > 2. There is a significant amount of scatter here, but the general trend is for increased velocity dispersion with higher [OIII]5007Å/Hβ, which largely coincides with the edges of the identified H II regions in (a).
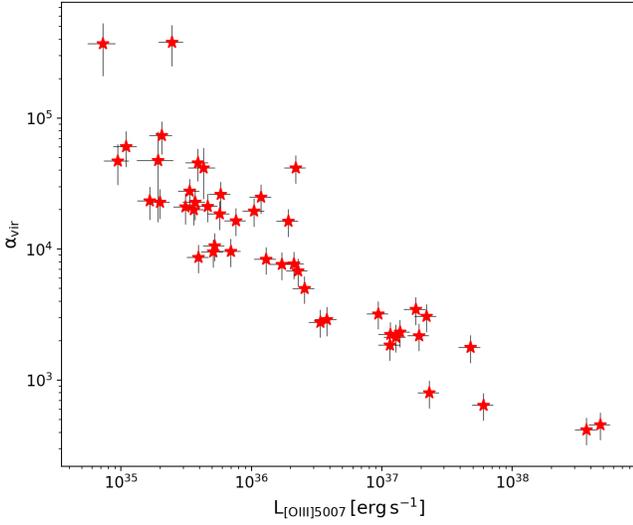
Figure 17. The virial parameter, $\alpha_{vir} = \frac{5\sigma^2 r}{GM_{gas}}$, plotted as a function of the integrated H II region luminosity. For all regions $\alpha_{vir} \gg 1$, indicating regions which are not virialized.

model summing Gaussian components for the full sample of H II regions due to the ease of extending this to a larger sample.

The excess in velocity dispersion that is not attributable to rotational motion can not be explained by virialization and therefore may lead to expansion of the H II regions. We estimate the amount of inward, P_{in}, and outward pressure, P_{out}, in the H II region, with an imbalance indicating that the region is not in equilibrium with the ISM. As a first order approximation, we
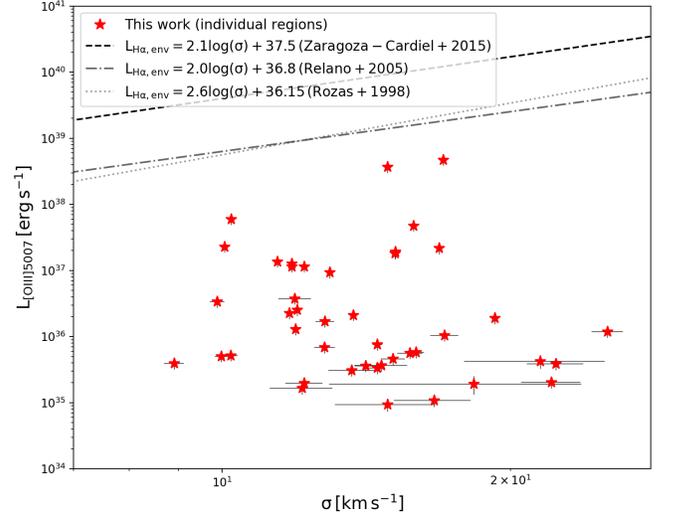
Figure 18. Measured L$_{[OIII]5007}$ plotted against σ from Gaussian fits to integrated H II region spectra. The lines show the fits to the upper envelope of this L $-\sigma$ relationship for other samples of H II regions. Regions that fall near the envelope are thought to be virialized while those below the curve are under-luminous for their velocity dispersion. This is the regime where the IC 10 regions fall, further supporting the interpretation that they are not virialized and show significant non-gravitational motion.

estimate the outward sources of pressure to come predominantly from thermal gas pressure,

$$P_{gas} = 2nkT, \tag{11}$$

(a)

(b)
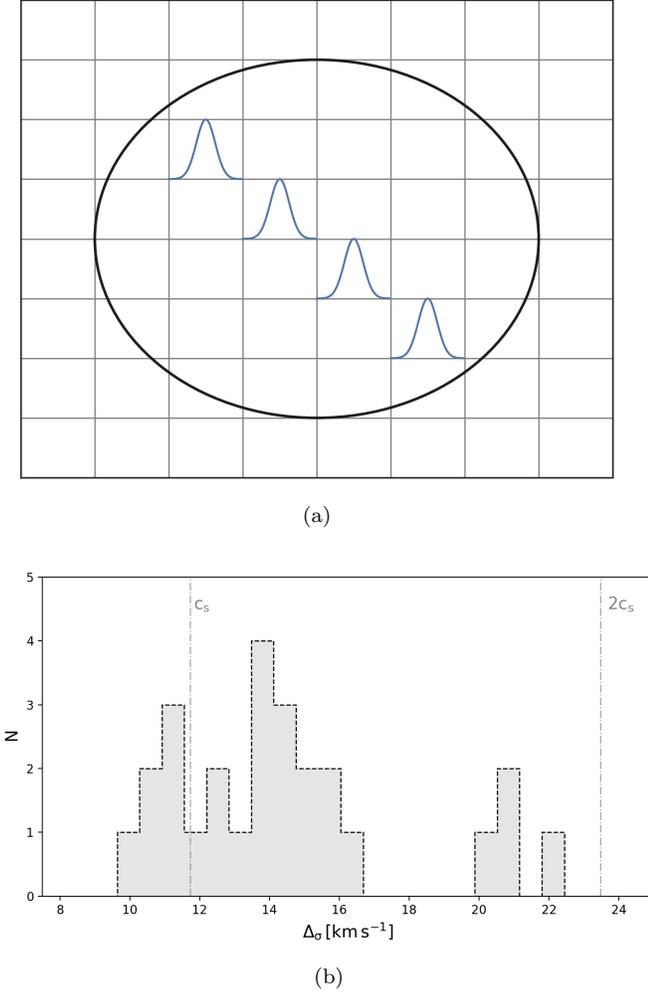
Figure 19. (a): Illustration of the Gaussian components summed in the simple model of a rotating H II region. Components are added at each spaxel along the axis of rotation with the flux of the final profile normalized to the measured spectrum. The width of each spaxel Gaussian is set by the instrumental width with the centers set by the measured rotational velocity. (b): Histogram of the non-rotational component of velocity dispersion measured in each of the rotating H II regions where $\Delta\sigma = \sqrt{\sigma_{\rm meas}^2 - \sigma_{\rm mod}^2}$, the difference between the measured and model velocity dispersion. The vertical dashed line shows the estimated sound speed in a typical H II region, $c_{\rm s}$, treating the region as an ideal gas with temperature T = 10^4K.

internal turbulence in the region,

$$P_{\rm turb,int} = \frac{1}{2}\rho\sigma_{\rm t}^2, \qquad (12)$$

and direct radiation pressure,

$$P_{\rm dir} = \frac{Qh\nu}{4\pi r^2 c}. \qquad (13)$$

where Q is the ionizing photon production rate which we can estimate from the integrated [OIII] luminosity of the H II region:

$$Q = \frac{L_{\rm [OIII]}\lambda}{hc} = \frac{L_{\rm [OIII]}}{h\nu}. \qquad (14)$$

Combining Equations 13 & 14 results in the formula for direct radiation pressure based on the measured luminosity:

$$P_{\rm dir} = \frac{L_{\rm [OIII]}}{4\pi r^2 c}. \qquad (15)$$

We use the definition of $r_{1/2}^*$ for the radius, r, k is the Boltzmann constant, and c is the speed of light. We are unable to directly measure the gas temperature, T, and number density, n, from our spectra so we use a constant temperature of T = 10^4 K and estimate n for each region from the Strömgren sphere approximation resulting in a median n $\sim 20\,{\rm cm}^{-3}$. This is significantly lower than the $\sim 10^2\,{\rm cm}^{-3}$ density determined by Polles et al. (2019) from models of infrared cooling lines in five of the brightest H II region complexes which are also included in this study, suggesting that we may be underestimating the actual density in the assumption of a Strömgren sphere representation. To maintain internal consistency with other measured and estimated quantities we will proceed with density determined from our KCWI spectra with the caveat that this may result in an underestimate of $P_{\rm gas}$ and $P_{\rm turb}$. This estimated value of n is combined with the mass of the hydrogen atom to determine the value of ρ used in the calculation of $P_{\rm turb,int}$. The turbulent linewidth, $\sigma_{\rm t}$ is evaluated by removing the thermal sound speed from the measured velocity dispersion, $\sigma_{\rm t} = \sqrt{\sigma^2 - c_{\rm s}^2}$, with $c_{\rm s}$ is defined as:

$$c_{\rm s} = \sqrt{\frac{\gamma kT}{m_{\rm h}}} \qquad (16)$$

where $\gamma = 5/3$ for an ideal gas.

The average values estimated for these pressure components are $P_{\rm dir} \sim 4 \times 10^{-14}\,{\rm dyne\,cm}^{-2}$, $P_{\rm turb,int} \sim 1 \times 10^{-11}\,{\rm dyne\,cm}^{-2}$, and $P_{\rm gas} \sim 5 \times 10^{-11}\,{\rm dyne\,cm}^{-2}$, making $P_{\rm gas}$ and $P_{\rm turb,int}$ the dominant factors in the outward pressure. One caveat is that the form of direct radiation pressure used here based on Q is specifically at the ionization front (McLeod et al. 2019). Another often used method to use the bolometric luminosity of all the stars in the region, which is estimated as $L_{\rm bol} \approx 138L_{\rm H\alpha}$ (or $L_{\rm bol} \approx 138L_{\rm [OIII]}$) (Lopez et al. 2014) in place of $L_{\rm [OIII]}$ in Equation 15. This would increase the impact of $P_{\rm dir}$, while still leaving it an order of magnitude less than $P_{\rm gas}$. However, there is some uncertainty in the correlation of $L_{\rm bol} \approx 138L_{\rm H\alpha}$ based on the age and star formation history of a region. This could overestimate

the bolometric luminosity for a young stellar population like that of an H II region (Lopez et al. 2014). Further, there is some disagreement on whether this definition of radiation pressure traces the force that is actually exerted on the gas, as this may be lower than the pressure in an optically thin medium like the interior of an H II region (Pellegrini et al. 2011; Krumholz et al. 2014). Since both definitions produce a radiation pressure here that is sub-dominant compared to P_{gas} we will proceed with the definition based on $L_{[OIII]}$, but note that the uncertainty in the definition of P_{dir} may result in a less drastic difference in the sources of pressure.

An additional source of outward pressure that is not included here is the hot gas pressure observed in X-rays. A diffuse X-ray component is observed in this same region of IC 10 with an average temperature of $\sim 4 \times 10^6$ K (Wang et al. 2005). Determining the temperature and number density of the X-ray emitting gas at the resolution of individual H II regions needed to include in P_{out} at this scale is beyond the scope of this study, but it would likely provide a smaller contribution than P_{gas} as found in a sample of 32 LMC and SMC H II regions which show evidence of leakage of this hot gas (Lopez et al. 2014).

For the inward pressure we combine the contributions of pressure due to self-gravity,

$$P_{grav} = GM^2/4\pi r^4 \tag{17}$$

where $M = M_{H II}$, with external turbulent pressure, $P_{turb,ext}$, from the surrounding gas evaluated following Equation 12. We estimate this latter pressure source with $\sigma_{t,ext}$ evaluated in a 3.5 pc (3 pixel) border around each H II region with the sound speed removed in the same way as the internal turbulent linewidth. The density, ρ used in the external turbulent pressure is the same as its internal counterpart as we do not have a direct method of measuring the gas density. This should still provide a reasonable first order estimate that may even be conservative as Polles et al. (2019) find lower typical densities in modelled zones containing diffuse gas than the bright H II regions in IC 10. On average the difference ($P_{turb,ext}$-$P_{turb,int}$), or the resulting turbulent pressure, provides an inward pressure which is $\sim 500 \times P_{grav}$ due to the compact, low-mass nature of the identified H II regions. As shown in Figure 20, 89% of the H II regions show $P_{out} > P_{in}$ with on average $P_{out} \sim 3P_{in}$. As these are all approximations it does not necessarily indicate that a given H II region exhibiting greater P_{out} will be expanding (and vice versa), but rather that it is likely that the majority of the H II regions in our sample are expanding into the ISM, especially since P_{out} can be considered a lower estimate with the exclusion of the hot

gas pressure. This additional component would increase the inbalance towards greater P_{out} and increase the likelihood and/or strength of the H II region expansion.
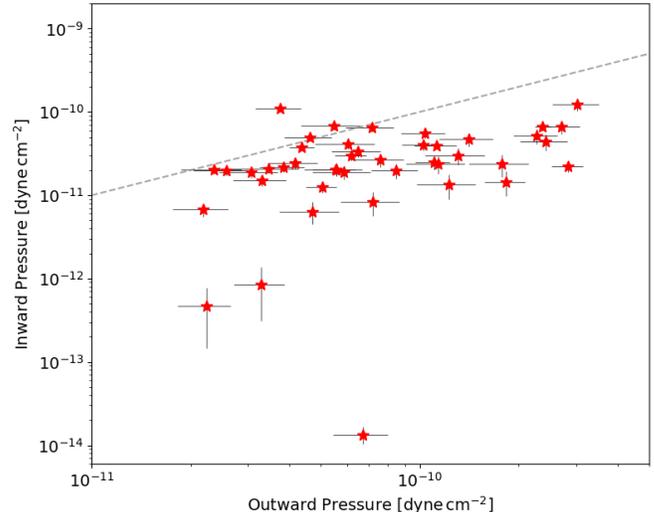

Figure 20. Comparison of inward and outward sources of pressure in the identified H II regions with the 1:1 line shown in gray. The inward pressure estimate is a sum of $P_{grav} + P_{turb,ext}$, while the outward estimate is a sum of $P_{gas} + P_{dir} + P_{turb,int}$. On average $P_{out} \sim 3P_{in}$, with 89% of the H II regions showing $P_{out} > P_{in}$.

Additionally, there are 6 H II regions where we find significantly elevated velocity dispersions at the region boundaries indicating the presence of outflows. These areas of elevated velocity dispersion are defined and identified using a similar method as identifying the H II regions described in Section 3.1. We use the `astrodendro` package along with the velocity dispersion map in Figure 13 to identify areas with a peak velocity dispersion $> 25\,\mathrm{km\,s^{-1}}$ and a minimum of $21\,\mathrm{km\,s^{-1}}$. These regions must also be resolved with a diameter greater than the FWHM measured from standard star observations. Of the regions identified with elevated velocity dispersion only those located at the border of an H II region are considered as potential outflows. These outflows and the host H II regions are shown in Figure 21.

We interpret the regions with elevated velocity dispersion as turbulent volumes. Turbulence is believed to decay on an eddy turnover time (roughly the crossing time of the turbulent region, l/σ), where l is the linear size of the turbulent region. Using the average properties measured from these turbulent regions of $l \approx 5.4$ pc and $\sigma \approx 25.5\,\mathrm{km\,s^{-1}}$ the turbulence will decay over 2×10^5 yrs, much shorter than the lifetimes or ages of the H II regions. This raises the question of what powers
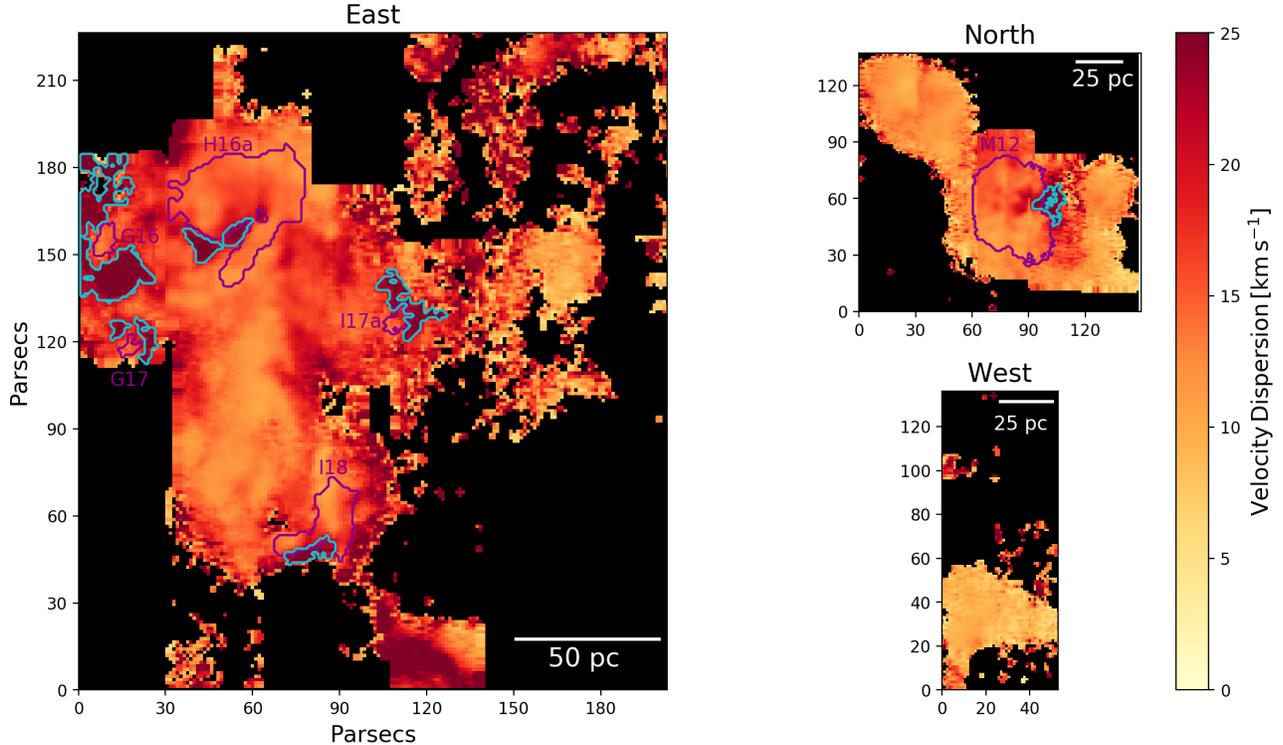
Figure 21. Maps of velocity dispersion of the ionized gas in IC 10 measured from Gaussian fits to the [OIII]5007Å line at each spaxel for the high resolution "small slicer, R∼18,000" observing mode. Each map is divided into the "North" portion of the FoV, the middle row shows the "West" field, and the bottom row shows the "East" region of the observed field. The purple contours mark the edges of the H II regions which are bordered by areas of elevated velocity dispersion which may be due to possible outflows, (outlined in cyan). These potential outflows must have a maximum velocity dispersion $\geq 25\,\mathrm{km\,s^{-1}}$ and a minimum of $21\,\mathrm{km\,s^{-1}}$. SNR >2 is required for these maps

the turbulence. We consider three possibilities: expansion of the H II regions causing outflows through lower density channels; photoionization heating of neutral gas; or stellar winds mixing with dense gas leading to turbulence.

In the simplest model we would expect all three of these mechanisms to act outward in a spherically symmetric zone around the central star cluster. However, H II regions do not typically exist in a medium of uniform density (e.g., Harper-Clark & Murray 2009; Rogers & Pittard 2013). There are holes and channels for outflowing gas to escape, which would produce isolated areas of increased turbulence rather than covering the entire perimeter, just as we see in these H II regions. This non-uniform density can clearly be seen from the irregular morphology of these 6 regions as well as the rest of IC 10's H II regions.

To first determine whether these regions of elevated velocity dispersion can be maintained by outflows generated from expansion of the observed H II regions, we compare the kinetic luminosity, L_{kin}, inside the star-forming region with the turbulent luminosity, L_{turb} in the potential outflow.

The kinetic luminosity crossing the boundary of the H II region is

$$L_{\mathrm{kin}} \equiv \dot{E}_{\mathrm{kin}} = \frac{1}{2} M_{\mathrm{H\,II}} v_{\mathrm{exp}}^2 \frac{v_{\mathrm{exp}}}{r_{1/2}^*}, \qquad (18)$$

where v_{exp} is the expansion velocity of the region defined as the half-width at zero intensity (HWZI)[3] of the emission line.

The turbulent luminosity in each elevated dispersion region is determined similarly from the rate of change of the kinetic energy attributable to turbulence, which we will refer to as $\dot{E}_{\mathrm{turb}}$ to differentiate it from the internal H II region kinetic energy above. This is defined as follows:

$$L_{\mathrm{turb}} \equiv \dot{E}_{\mathrm{turb}} = \frac{1}{2} M_{\mathrm{t}} \sigma^2 \frac{\sigma}{l} \qquad (19)$$

where M_{t} and σ are the ionized gas mass and velocity dispersion in the potential turbulent region, measured

---

[3] Note that the HWZI is proportional to the velocity dispersion, σ, but is a more physically intuitive way of denoting the expansion velocity as it captures the full range of velocities contributing to the Gaussian line profile.

in the same way as their counterparts inside the H II regions and l is the average of the turbulent region major and minor axes. σ is measured from the Gaussian fit to [OIII]5007Å and M_t is calculated from the density determined via the Strömgren sphere approximation. This relies on the assumption that most of the gas in the areas of elevated velocity dispersion is ionized, which may not be reliable outside of an H II region and particularly for the more extended areas of elevated dispersion. We may then be underestimating M_t and thus L_{turb}.

The second possible scenario for these turbulent regions at the edges of the identified H II regions are "champagne" or "blister" flows (e.g., Israel 1978; Tenorio-Tagle 1979) in which radiation from the central star cluster heats and ionizes neutral gas. This causes an area of overpressure, resulting in rapid expansion of the gas and could explain the observed elevated velocity dispersions. We estimate the amount of energy available for this mechanism from the type and number of ionizing stars in each H II region determined in Section 3.3.3. We take the effective temperature, T_{eff} for the stellar type from the models of Martins et al. (2005) for O stars and Smith et al. (2002) for B stars, combined with Wien's Law to estimate the wavelength at the peak of the black-body curve. We assume this represents the average energy of the emitted photons. We take the amount of energy above 13.6 eV as the energy imparted to the electron after ionizing a hydrogen atom. This is combined with the ionizing photon production rate for the determined stellar type and the number of stars required, N_{stars}. This is 1 except for the case of H16a and M12 which require multiple O3 stars to produce the measured luminosity:

$$L_{champagne} = (E_{peak} - 13.6eV) Q N_{stars} \qquad (20)$$

where E_{peak} is the energy of a photon at the peak wavelength.

The third possible explanation for the observed velocity dispersions are winds from massive stars. This can result in turbulence at the interface of the hot wind and cold dense gas where mixing occurs and thermal energy is dissipated (Krumholz et al. 2019). The wind luminosity is described by the following equation

$$L_{wind} = \frac{1}{2} \dot{M} V_{wind}^2 N_{stars} \qquad (21)$$

where $\dot{M}$ is the mass loss rate in the stellar wind and V_{wind} is the wind speed. For the B0 star in H II region G17, $\dot{M}$ and V_{wind} are taken directly from the Smith et al. (2002) models. For the O stars in the other 5 H II regions, these quantities are estimated from the stellar mass, M, luminosity, L, and radius, R, determined in

the Martins et al. (2005) models. The wind velocity is then estimated as

$$V_{wind} = 3\sqrt{2GM/R}, \qquad (22)$$

with a maximum mass loss rate of

$$\dot{M} = \frac{L}{V_{wind}c} \qquad (23)$$

following Lamers & M. Levesque (2017).

The required L_{turb} as well as the luminosities available from each scenario to power the observed turbulence are reported in Table 5. It should be noted that each of these scenarios assumes a spherically symmetric deposition of energy and thus should be multiplied by the factor, Ω, the fraction of a sphere covered by the outflow as seen from the stars, determined from the ratio of the projected area of the outflow and H II region. If the luminosity available in the outflow mechanism multiplied by Ω is greater than L_{turb}, it indicates that the mechanism could provide sufficient energy to support the energy dissipated in the turbulent region.

For the three largest regions with potential outflows, H16a, I18, and M12 $L_{kin}\Omega > L_{turb}$ with H16a $L_{kin}\Omega \sim 1.5L_{turb}$, M12 with $L_{kin}\Omega \sim 3L_{turb}$, and $L_{kin}\Omega \sim L_{turb}$ for I18. However, for these same three H II regions the early O stars needed to produce the measured $L_{[OIII]}$ produce estimated L_{wind} and $L_{champagne}$ that are greater than L_{kin}. For region I18 which requires a single O5 star, $L_{wind} \sim 2 \times L_{kin}$ while $L_{wind} \sim 10 \times L_{kin}$ for H16a and M12 which require multiple O3 stars. In all three of these H II regions, $L_{champagne}$ is estimated to be ~ 2 orders of magnitude greater than L_{kin}. This scenario of observing champagne flows in the turbulent regions around these 3 H II regions is therefore the most likely.

For the three smaller regions, G16, G17, and I17a, L_{kin} is not high enough to sustain the turbulence we see. This is unsurprising as the turbulent regions are comparable in size or larger than the H II region they border (see Figure 21). G16 and I17a both require a single O9 star to produce the required ionization, and the estimated winds from this type of star produce $L_{wind}\Omega \sim 100-1000 \times L_{turb}$ indicating that stellar winds are a possibly sufficient source of energy to sustain the turbulent regions around G16 and I17a. For G17, none of three scenarios considered here produce a sufficient amount of energy to support the measured turbulence in the surrounding region. While these estimates are approximate, this along with the extended nature of the turbulence around G17 indicate an external source of energy.

Table 5. Outflow Properties

ID	radius	stellar type	Turbulent Region				H II Region				
			σ	$\tau_{\rm eddy}$	$L_{\rm turb}$	Ω	$v_{\rm exp}$	$\tau_{\rm dyn}$	$L_{\rm kin}$	$L_{\rm champagne}$	$L_{\rm wind}$
	(pc)		$({\rm km\,s^{-1}})$	$(10^6\,{\rm yrs})$	$({\rm erg\,s^{-1}})$		$({\rm km\,s^{-1}})$	$(10^6\,{\rm yrs})$	$({\rm erg\,s^{-1}})$	$({\rm erg\,s^{-1}})$	$({\rm erg\,s^{-1}})$
G16	2.60	O9	27.12	0.35	1.94×10^{36}	0.30	44.06	0.07	4.08×10^{35}	5.99×10^{35}	6.31×10^{38}
G17	2.11	B0	22.92	0.11	1.59×10^{35}	0.19	44.05	0.05	2.44×10^{35}	$-2.73 \times 10^{35\,a}$	5.46×10^{34}
H16a	10.32	O3	25.98	0.11	7.02×10^{35}	0.03	51.65	0.22	3.27×10^{37}	3.06×10^{39}	1.40×10^{38}
I17a	2.56	O9	25.31	0.24	3.27×10^{35}	0.20	51.76	0.06	7.70×10^{35}	5.99×10^{35}	6.31×10^{38}
I18	7.02	O5	25.19	0.15	2.12×10^{35}	0.05	46.02	0.17	3.84×10^{36}	1.13×10^{38}	7.04×10^{36}
M12	9.24	O3	27.01	0.19	4.79×10^{35}	0.08	45.17	0.23	1.82×10^{37}	2.29×10^{39}	1.05×10^{38}

Note—Measured properties and estimated energies in the turbulent regions and associated H II regions.

[a] The negative value of $L_{\rm champagne}$ for region G17 is due to the method of estimation (Equation 20). The peak photon energy for a B0 star used to estimate the average is $< 13.6\,{\rm eV}$, giving a negative estimate of $L_{\rm champagne}$. This merely indicates that the turbulent region observed is unlikely to be due to a champagne flow.

3.6. Metallicity

The KCWI small slicer, R∼18,000 mode observations used throughout this analysis provide a detailed look at the structure and kinematics of the ionized gas, but the wavelength coverage is extremely limited. Our supplementary observations in the large slicer, R∼900 mode rectify this shortcoming with coverage from 3500-5500Å, at the expense of more limited spatial sampling and spectral resolution. This wavelength range allows us to estimate the gas-phase metallicity throughout IC 10. Ideally, the auroral [OIII]4363Å line would be used with [OIII]5007Å to infer the electron temperature and metallicity (e.g., Kewley et al. 2019), but this is a very weak emission line and is unfortunately not detected in our stacked or individual spaxel spectra. Instead, we use the empirical R_{23} strong line calibration. The commonly used R_{23} was proposed by Pagel et al. (1979) as a calibration with the oxygen abundance as it is less sensitive to geometric factors than the [OIII]/Hβ ratio alone. It is defined as:

$$R_{23} = \frac{{\rm F([OII]3727, 3729\text{\AA})} + {\rm F([OIII]4959\text{\AA})} + {\rm F([OIII]5007\text{\AA})}}{{\rm F(H\beta)}}$$

(24)

One caveat with this diagnostic is that it is degenerate, providing two possible values of the metallicity for a given R_{23}. Another diagnostic ratio is therefore required to determine the correct solution. These nebular ratios often make use of the [NII]6584Å line (Nagao et al. 2006), but since this is not in the observed wavelength range we will instead use the line flux ratios utilizing [OIII]5007Å, [OIII]4959Å, and the [OII]3727,3729Å doublet; an indicator of the ionization parameter.

After applying the dereddening correction and DIG subtraction described in Section 3.2, we employ a similar fitting method as for the [OIII]5007Å/Hβ line ratio at each spaxel: fitting a Gaussian profile to the Hβ line and using the center to define the systemic velocity shift at that spaxel and the width to define the number of wavelength channels over which to integrate the emission line fluxes. These fluxes are determined by a direct sum of the flux at that wavelength channel in the spectrum rather than integrating over the fitted Gaussian so as not to skew the resulting flux of the [OII]3727,3729Å doublet by the fitting of a single Gaussian. Defining the same central velocity and line width ensures that each line flux is evaluated over the same gas column. Any spaxel with a SNR of the [OII]3727,3729Å doublet $({\rm SNR_{[OII]}}) < 3$ is removed from the analysis. Due to this cut only the "East" (lower left) portion of the field covering the HL111 and HL106 complexes of Hodge & Lee (1990) is included here and shown in Figure 22, with the vast majority of this field showing ${\rm SNR_{[OII]}} > 4$.

There are a number of calibrations in the literature utilizing the R_{23} parameter, but we will limit our discussion to just three: the theoretical calibration of Kobulnicky & Kewley (2004) (hereafter KK04), and empirical calibrations from Pilyugin & Thuan (2005) (PT05) and Nagao et al. (2006) (N06). Both the KK04 and PT05 calibrations rely on separate equations for what are referred to as the "upper" and "lower" branches of the diagnostic, while N06 uses a single continuous calibration. All three employ a diagnostic ratio involving one or more [OIII] lines and [OII]3727,3729Å in addition to R_{23}.

The KK04 equations for oxygen abundance on each branch are dependent on R_{23} as well as the ionization parameter, q, which is in turn dependent on the oxygen abundance and O_{32}, defined as:

$$O_{32} = \frac{F([OIII]4959\mathring{A}) + F([OIII]5007\mathring{A})}{F([OII]3727, 3729\mathring{A})} \qquad (25)$$

Since the equations for oxygen abundance and ionization parameter are dependent on each other this method requires an iterative solution, but the result converges after a few iterations. The transition between the two branches is noted to be at $12 + \log(\text{O/H}) = 8.4$. This is slightly higher than the global metallicity typically measured for IC 10 at $12 + \log(\text{O/H}) \sim 8.2$ (e.g., Skillman et al. 1989; Lebouteiller et al. 2012), making the lower branch likely a better match.

The PT05 calibration does not require iteration, with each branch simply being dependent on the value of R_{23} and the line ratio P:

$$P = \frac{F([OIII]4959\mathring{A}) + F([OIII]5007\mathring{A})}{F([OIII]4959\mathring{A}) + F([OIII]5007\mathring{A}) + F([OII]3727, 3729\mathring{A})}$$
$$(26)$$

For this calibration there is a "transition zone" between $8.0 < 12 + \log(\text{O/H}) < 8.5$ where the lower branch applies for values < 8.0 and the upper branch applies for values > 8.5. This transition zone does fall at the expected metallicity for IC 10, so the results from this method should be taken with caution.

The N06 calibration, by contrast does not have a separate equation for the upper and lower branches. The equation for the oxygen abundance is also only dependent on the value of R_{23}, however the solution is double valued, relying on the [OIII]5007Å/[OII]3727,3729Å (or other) line ratio to break this degeneracy. We evaluate the oxygen abundance in our IC 10 field using this method to determine the most likely solution for each spaxel independently and also by constraining the solution for the entire field to either the upper or lower portion of the curve, mimicking the two branches of the KK04 and PT05 methods.

The results for all three calibrations and the branches of each are summarized in Table 6 which includes the mean metallicity throughout the field, for spaxels inside detected H II regions, and for spaxels outside H II regions. The upper branch solutions seem to systematically overestimate the oxygen abundance, a not unexpected result given the low global metallicity of IC 10. The continuous N06 calibration gives an unrealistic result when the degeneracy is broken at each spaxel based on the [OIII]/[OII] ratio, resulting in an abrupt jump from low to high solutions at the edges of H II regions rather than a smooth transition. Even when constrained

to the lower solutions, the N06 calibration appears to give less realistic estimates with a ~ 0.9dex lower average metallicity than the previous estimates for IC 10.

The lower branches of the KK04 and PT05 calibrations give the most reasonable results for the metallicity throughout this field of view in IC 10 with average metallicities $12 + \log(\text{O/H})_{\text{PT05,lower}} \approx 7.85 \pm 0.03$ and $12 + \log(\text{O/H})_{\text{KK04,lower}} \approx 8.22 \pm 0.02$. There is a well studied offset between these two calibrations and it is thought that they span the range of potential "true" values (e.g., Moustakas et al. 2010; Kewley & Ellison 2008), making this 0.4dex range a good indicator of the likely metallicity in this region of IC 10. While the values differ, the variation in metallicity across the field is consistent between both the KK04 and PT05 results. With both calibrations there is an average ~ 0.1dex lower metallicity inside the H II regions than in the surrounding gas. On average this difference is within the uncertainties, with some areas of higher metallicity in the diffuse gas being more apparent in the maps of Figure 22. This trend is consistent with the study by McLeod et al. (2019) of two H II region complexes in the LMC in which they find lower oxygen abundance within the compact H II regions than elsewhere in the complex. The difference in metallicity in this study is larger than in IC 10, although the authors note that there is a dependence in their calibrations on ionization parameter (as the MUSE spectra do not cover [OII]3727Å needed for R_{23}) and the abundances may therefore be underestimated in the H II regions. An earlier study by Russell & Dopita (1990) also found slightly lower metallicity in individual H II regions in the SMC and LMC (0.1dex and 0.22dex respectively) than the global measurements. Deeper and wider field observations in IC 10 and other local galaxies are needed in order to form a clearer picture of the metallicities of H II regions relative to the surrounding gas.

3.7. Diffuse Ionized Gas

A significant fraction of the ionized gas emission in star forming galaxies has been observed outside of the H II regions in the DIG. Often studies will differentiate the DIG from the star formation based on the Hα surface brightness. For example, in a sample of 109 galaxies, Oey et al. (2007) attribute $\sim 60\%$ of the Hα flux to the DIG with no correlation based on the galaxy Hubble type. Lacerda et al. (2018) on the other hand, propose a system of differentiating the DIG based on the equivalent width instead. They do find a correlation in the DIG fraction with Hubble type, with the highest contribution in ellipticals and lowest in late type galaxies, resulting in a similar average DIG fraction but with a

Table 6. Metallicity Calibration Results

Method	Mean Inside Regions	Mean Outside Regions	Total Mean
	$12 + \log(O/H)$	$12 + \log(O/H)$	$12 + \log(O/H)$
Lower Branch			
KK04	8.14 ± 0.01	8.26 ± 0.02	8.22 ± 0.02
PT05	7.76 ± 0.01	7.89 ± 0.03	7.85 ± 0.03
N06[a]	7.50 ± 0.01	7.53 ± 0.01	7.52 ± 0.01
Upper Branch			
KK04	8.85 ± 0.01	8.79 ± 0.01	8.81 ± 0.01
PT05	8.40 ± 0.01	8.22 ± 0.02	8.27 ± 0.02
N06[a]	8.61 ± 0.01	8.58 ± 0.01	8.59 ± 0.01
Continuous Calibration			
N06	8.26 ± 0.03	8.10 ± 0.04	8.13 ± 0.04

NOTE—Average oxygen abundance derived from the three different calibrations for the upper and lower branches. The means are derived inside and outside the contours of the identified H II regions as well as over all spaxels. The lower branches of the PT05 and KK04 branches provide the most reasonable solutions for the metallicity given the existing global measurements of IC 10 which are below the branch transitions. The results from these two methods likely bracket the true metallicity.

[a] The "upper" and "lower" branches of the N06 calibration are evaluated from the same equation with the root in the desired range taken as the solution rather than using the [OIII]5007Å/[OII]3727,3729Å line ratio to break the degeneracy.

wide distribution, $56\% \pm 38\%$. Part of the cause for the differing conclusions from these two large studies is likely due to the two methods of differentiating DIG from star forming regions.

Before the identification and spectral analysis of IC 10's H II regions we performed a conservative subtraction of the DIG contribution based on the choice of a low surface brightness region free of known H II regions. This resulted in an average DIG contribution of $\sim21\%$ of the [OIII]5007Å flux per spaxel across the FoV, with only $\sim1\%$ at the H II regions. Of the total [OIII]5007Å flux observed in our FoV, 78% is contained in the H II regions, 20% in the connecting complexes, and the remaining 2% from the DIG. This is significantly lower than what would be expected for the overall DIG contribution in IC 10, but our field of view intentionally selected an area dense with H II regions and complexes. To estimate the flux contribution of these three components throughout IC 10 as a whole the measured flux is scaled based on the ratio of the number of H II regions observed to total identified previously in IC 10 (Hodge & Lee 1990) and the ratio of area observed to total area. This reduces the total estimated flux contribution from H II regions to only 26%, complexes to 7%,

and increases the estimated DIG contribution to 57% throughout IC 10. This estimate for the galaxy as a whole is more in line with values seen in previous studies for the DIG contribution to galaxy flux (e.g., Oey et al. 2007), but highlights the irregular distribution of H II regions and DIG in irregular galaxies such as IC 10.

We differentiate the H II regions and DIG based on the ionized gas surface brightness, but compare the equivalent width between these areas of emission. Interestingly we find no significant difference between the distribution of Hβ equivalent width between spaxels identified as belonging to an H II region and that belonging to DIG in IC 10. This may be a selection effect of our study. The high density of H II regions not only gives a small sample of diffuse gas, but also makes it likely to be more closely associated with the inter-dispersed H II regions than is typical of DIG studies. However, the DIG in IC 10 may be ionized by different sources than typically observed. (Hidalgo-Gámez 2005) finds higher excitation in the IC 10 DIG than for spiral galaxies which they find can be produced by leakage from H II regions and the large number of WR stars. The gas throughout IC 10, and particularly in the KCWI FoV, may be more similar to what Lacerda et al. (2018) refers to as mDIG,
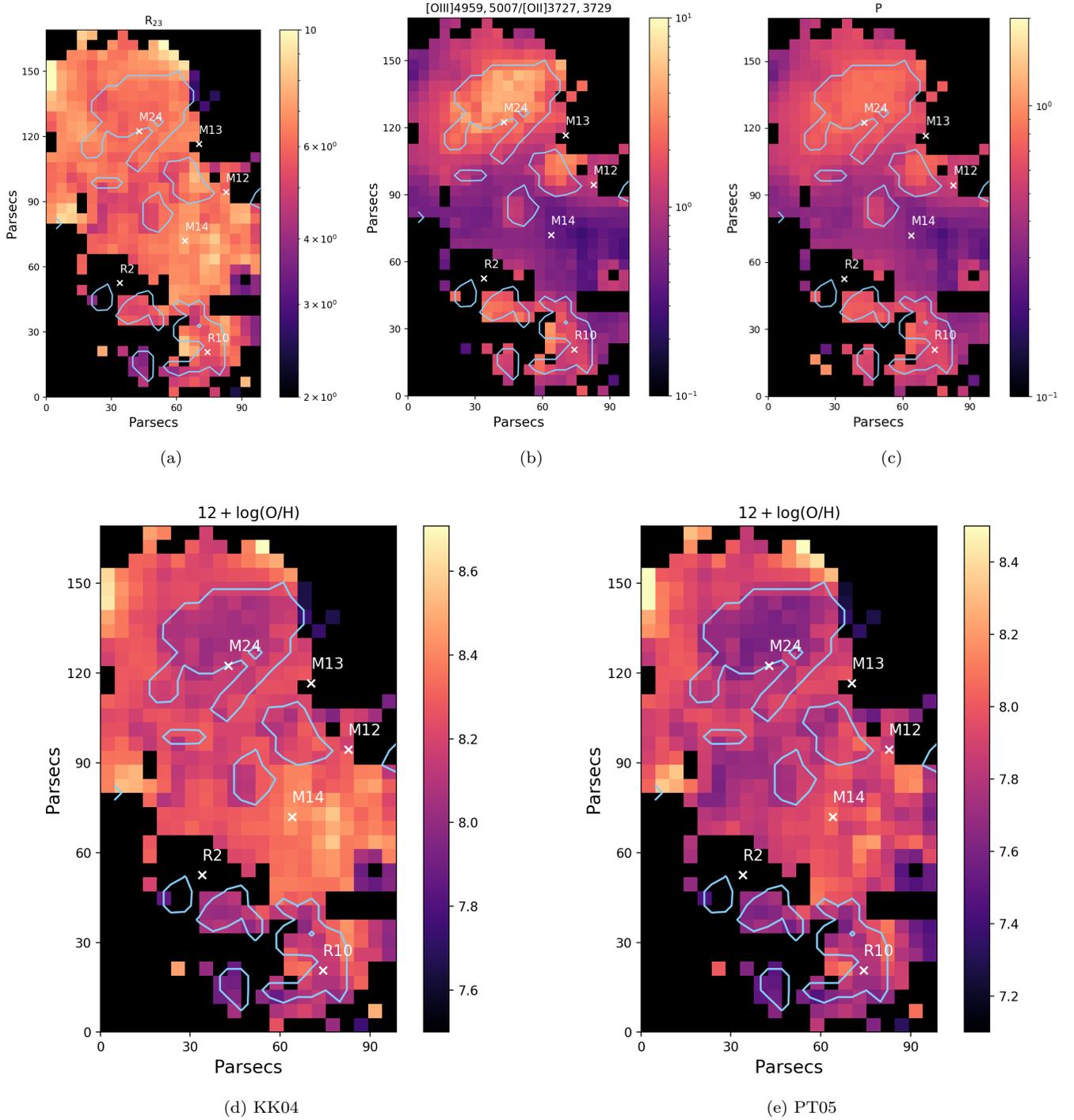
Figure 22. Diagnostic line ratio maps from the "large slicer, R∼900" mode observations. Due to the lower SNR of the [OII]3727Å line only the lower left portion of the field is shown, coinciding with the "East" field of the high resolution observations discussed in the majority of this study. (a): R_{23} metallicity diagnostic. (b): O_{32} line ratio (Equation 25) used in the KK04 metallicity calibration. (c) P line ratio (Equation 26) used in the PT05 calibration. (d) Metallicity as determined by the KK04 diagnostic. (e) Metallicity as determined by the PT05 diagnostic. The metallicities are systematically lower than in the KK04 map, but the locations of lower *relative* metallicity are consistent. The H II regions identified in the high resolution mode are shown with the light blue contours (binned to the resolution here) and the locations of known WR stars are marked with white X's.

or 'mixed' DIG in which the ionization source is due to a combination of processes such as emission from an older stellar population in addition to photon leakage from H II regions. This is consistent with the small difference in metallicity we see between the H II regions and surrounding gas in comparison with other studies, as well as Polles et al. (2019) Cloudy simulations showing matter-bounded regions in IC 10 which would result in escaping photons ionizing the DIG.

3.8. *Scaling Relations*

In Cosens et al. (2018) we developed a framework to use Bayesian inference via PyStan to fit the scaling relationships between the properties of local and high-redshift star-forming regions in the literature. In this study we focused primarily on the relationship between star forming region size and Hα luminosity ($L_{H\alpha}$), which takes on the form of a power law:

$$L_{\mathrm{H}\alpha} = exp(\beta)r_{\mathrm{clump}}^{\alpha} \qquad (27)$$

with r_{clump} giving the radius of the star forming region and β giving the intercept of the fit. The key model parameter of interest is the slope, α. The value of this slope holds information about the driving formation mechanism of the star-forming regions. A slope of r^3 is often explained by a region which forms under Jeans collapse and is then well-represented by a Strömgren sphere. On the other hand, a slope of r^2 is often explained by a region which forms under Toomre instability and undergoes the fastest mode of Jeans collapse resulting in a different form for the characteristic mass and size (e.g., Genzel et al. 2011). In Cosens et al. (2018) we found that this r^2 slope could also be explained by a Strömgren sphere argument where the ionizing photon production rate is large enough that the radius of the region is larger than the scale height of the galaxy disk. This would lead to a non-spherical geometry and an observed relationship of $L \sim r^2$.

Using Bayesian inference provides a number of advantages over standard least-squares fitting. First, uncertainties in every dimension can be incorporated in the fitting; there is no need to estimate a single overall uncertainty assigned to one dimension. Second, we can use our existing knowledge of the scaling relationships between parameters to inform our model through the use of Bayesian priors. Third, this method reproduces a distribution for each model parameter, allowing the determination of not only the best fit model, but robust determination of uncertainties for each model component as well. Using this framework allowed us to perform robust fits to the overall scaling relationships as well as investigate potential differences in smaller subsamples

such as redshift bins and lensed versus field galaxies. Interestingly, we were able to identify a possible break in the size-luminosity scaling relationship based on the Σ_{SFR} of the star-forming region.

However, a key missing area of the parameter space in our previous investigation was small, low $L_{H\alpha}$ star-forming regions (< 50 pc, $< 10^{34-36}$ erg s^{-1}). This sets the limit on the low-mass end of the relationship and helps to constrain the intercept when performing fits. One challenge in interpreting fitting results for sub samples of the local and high-redshift clumps was that the best fit slope and intercept are not entirely independent parameters. Therefore, missing constraints on the low-mass intercept of the size-luminosity relationship makes it difficult to be certain whether a change in slope is really a change in that parameter or just in the lever arm of the fit. With the proximity of IC 10 and the sensitivity of KCWI we are able to target a large sample of H II regions at this crucial scale.

3.8.1. *Size-Luminosity Relationship*

While these small, low-mass star-forming regions are critical for constraining the intercept of the size-luminosity relationship, one must first check that the possibility of stochastic sampling is not biasing the measured properties. The lower mass limit to avoid stochastic effects is typically determined to be $M_* \sim 10^3 M_\odot$ (e.g., Hollyhead et al. 2015; Krumholz et al. 2015). Below these masses random sampling of the IMF can lead to deviations between the actual physical properties and those determined from photometric measurements. The average stellar mass distribution determined for the IC 10 H II regions from the measured [OIII]5007Å flux is $M_* \sim (4 \pm 14) \times 10^2 M_\odot$, with 96% falling below the $10^3 M_\odot$ limit. Further, IC 10's H II regions are largely consistent with ionization predominantly from a single O or B type star which will be stochastic by nature. Hannon et al. (2019) found themselves faced with a similar dilemma studying a sample of ∼700 young star clusters with over 90% below the stochastic limit. They investigate a method of mitigating the impact of stochastic sampling by stacking the fluxes of individual clusters with similar properties. These composite clusters no longer fall into the regime of stochastic sampling, but Hannon et al. (2019) still find results consistent with the individual clusters. We apply a similar check to our sample, but rather than stacking the H II region spectra, we instead make use of the hierarchical structure determined from `astrodendro` which identifies the H II region complexes. Using the complexes results in a smaller sample than with individual regions, but one that lies above the stochastic limit with a mean $M_* \sim 2 \times 10^3 M_\odot$.

We do not find any significant deviation in the trends determined for the complexes vs. the individual H II regions, finding proportional increases in the mass and luminosity to the increase in radius (e.g., Figure 23). The measured properties of individual regions may show an increase in scatter due to stochastic sampling, but the average sample properties and trends do not appear to be affected. Therefore we will proceed with the determination of the scaling relationships using the individual regions in the fitting, but we will include the complexes in all figures for comparison.

Fitting the size-luminosity relationship using our MCMC framework with just IC 10 H II regions yields a slope of $L_{H\alpha} \propto r_{clump}^{3.6}$. The complexes do shift to slightly larger radii than the individual H II regions but with a proportional increase in luminosity, placing them along the same relationship. We also combine these regions with the full sample of H II regions and high-redshift clumps outlined in Cosens et al. (2018), now including additional published samples of star-forming regions in the SMC (Kennicutt & Hodge 1986), LMC (Ambrocio-Cruz et al. 2016), NGC 6822 (Hodge et al. 1989), and local LIRGs (Zaragoza-Cardiel et al. 2017; Larson et al. 2020). These LIRG studies also make use of `astrodendro` to identify star-forming regions and their properties[4]. Collating all low and high-redshift samples results in a significantly shallower slope of approximately $L_{H\alpha} \propto r^3$; matching the result of fitting the full sample in Cosens et al. (2018) and indicating the IC 10 H II regions may be an outlier. The IC 10 fit and entire sample fit are shown in Figure 23, where it can be can see that the IC 10 H II regions lie above the size-luminosity relation found for the full sample. This is also true of some other local samples, particularly in more extreme environments such as the LIRGs (e.g. Larson et al. 2020) and turbulent galaxies (Fisher et al. 2017). Whether the offset of the IC 10 H II regions is then due to improved resolution breaking the IC 10 regions down into more compact components, or due to a fundamental difference in the environments of star-forming regions driving scatter in the scaling relationships is not fully clear. It may be that active expansion of these regions as discussed in Section 3.5.4 leads to the offset we see here with the H II regions currently being under-sized for their luminosity.

The full results of these fits and those described in Section 3.8.2 are shown in Table 7 for the intercept, slope, and intrinsic scatter along with their uncertainties. Re-

sults of fitting additional data subsets (as detailed in column 1) are also included for completeness.

3.8.2. Σ_{SFR} break

In Cosens et al. (2018), we found that there was a potential break in the size-luminosity relationship that divides star-forming regions into two samples: one with high Σ_{SFR} and one with low Σ_{SFR} with the break nominally located at a value of $\Sigma_{SFR} = 1\,M_\odot\,yr^{-1}\,kpc^{-2}$. Both locally and at high redshift we found that lower Σ_{SFR} star-forming regions followed a size-luminosity relationship of $L \sim r^3$, while the high Σ_{SFR} sub-sample followed a relationship closer to $L \sim r^2$.

In our observations of IC 10's H II regions, the average size of identified H II regions is $r_{avg} = 4.0\,pc$ with a $\Sigma_{SFR,avg} = 0.20\,M_\odot\,yr^{-1}\,kpc^{-2}$ with only 2 identified H II regions falling above the $\Sigma_{SFR} > 1\,M_\odot\,yr^{-1}\,kpc^{-2}$ limit. When combined with the full comparison sample this does still provide some improvements on constraining the size-luminosity relationship at low masses by reducing the uncertainties on the fitted parameters. The resulting slopes for the two populations remain consistent with the previous results, with nominal values differing by $< 2\sigma$.

3.8.3. Size - Velocity Dispersion

Larson (1981) found an empirical relationship between the size of molecular clouds and their velocity dispersion that is tied to turbulence in the clouds and ISM. For resolved Milky Way GMCs in virial equilibrium, Larson (1981) found a relationship:

$$\sigma = 1.1 r^{0.38} \qquad (28)$$

where r is the radius of the GMC in pc and σ is in $km\,s^{-1}$. This has been refined and updated with expanded galactic (Solomon et al. 1987) and extra-galactic (Bolatto et al. 2008) data sets of molecular clouds, arriving at slight changes to the scaling but the same basic conclusion that the line width increases with cloud size approximately $\propto r^{1/2}$. This scaling is typically interpreted as being due to turbulence in the molecular clouds (e.g., Larson 1981; Bolatto et al. 2008).

While Larson's Law is usually discussed in relation to GMCs it may also apply to ionized gas in star-forming regions if they are in virial equilibrium and exhibit turbulent motions. Wisnioski et al. (2012) fit this relationship with a portion of the local and high-redshift data sets used in the present study and find a scaling of $\sigma \propto r^{0.42}$, but determine that their $z \sim 1$ clumps are likely not virialized. We test this now with the addition of local and high-z star-forming regions measured with IFS observations since the study by Wisnioski et al.

---

[4] The effective radii, r_{eff}, of Zaragoza-Cardiel et al. (2017) are adjusted to match our definition of $r_{1/2}^*$ for a consistent comparison.

Table 7. Size - Luminosity Relation Fit Parameters: $(L_{H\alpha} = e^{\beta} r_{clump}^{\alpha})$

Sample	Subset Criteria	Figure	α	β	Scatter (r)	Scatter (L)	# of Clumps
IC 10	$\cdots$	23	$3.601^{+0.471}_{-0.385}$	$78.812^{+0.455}_{-0.652}$	$0.147^{+0.154}_{-0.103}$	$0.156^{+0.144}_{-0.103}$	46
all comparisons	$\cdots$	$\cdots$	$3.215^{+0.023}_{-0.030}$	$73.782^{+0.129}_{-0.119}$	$0.184^{+0.118}_{-0.112}$	$0.171^{+0.115}_{-0.114}$	3858
	high Σ_{SFR}	$\cdots$	$1.788^{+0.063}_{-0.059}$	$84.617^{+0.314}_{-0.357}$	$0.461^{+0.317}_{-0.316}$	$0.470^{+0.320}_{-0.314}$	264
	low Σ_{SFR}	$\cdots$	$2.967^{+0.024}_{-0.027}$	$74.670^{+0.123}_{-0.111}$	$0.142^{+0.092}_{-0.095}$	$0.136^{+0.092}_{-0.093}$	3573
IC 10 & all comparisons	$\cdots$	23	$3.002^{+0.023}_{-0.024}$	$74.800^{+0.100}_{-0.115}$	$0.240^{+0.147}_{-0.154}$	$0.249^{+0.154}_{-0.151}$	3904
	high Σ_{SFR}	24	$1.841^{+0.070}_{-0.059}$	$84.310^{+0.335}_{-0.384}$	$0.426^{+0.279}_{-0.285}$	$0.360^{+0.323}_{-0.268}$	266
	low Σ_{SFR}	24	$2.775^{+0.021}_{-0.018}$	$75.577^{+0.086}_{-0.090}$	$0.194^{+0.136}_{-0.132}$	$0.194^{+0.132}_{-0.138}$	3617

NOTE—Results of model parameters determined from MCMC fitting of IC 10 H II regions and the local and high-redshift comparison sample for all fits discussed in Section 3.8 as well as additional fits to only the comparison sample (rows 2-4).

(2012). Unfortunately, not all data sets used to investigate the size-luminosity relationship have spectral information, but it is still a large enough sample (515 regions) to investigate the presence of a similar size-velocity dispersion relationship. In fact, we do see a clear trend where the velocity dispersion increases with larger size regions, except with IC 10, which is still a notable outlier. On their own, IC 10 H II regions do not show any evidence of this power law scaling, and instead when included significantly skew the resultant slope. Without IC 10 included we arrive at a relationship of $\sigma \propto r^{0.4}$ using the same MCMC framework as described in Section 3.8, in line with the results of Wisnioski et al. (2012) and similar to the GMC results. However, when the IC 10 H II regions are included, they clearly lie above the size - σ relationship found for the other samples as shown in Figure 25. Furthermore, including the IC 10 regions in the fitting reduces the slope to $\sigma \propto r^{0.2}$. This further supports the conclusion in Sections 3.4 & 3.5.4 that the H II regions identified in this study are not generally virialized. In fact, if we retain only the component of velocity dispersion due to rotational motion as identified in Section 3.5.4, then the identified H II regions in IC 10 follow the same relationship identified for the rest of the samples (see Figure 25b). There is a significant amount of scatter in the r − σ relationship, but it suggests that rotational motion is a much more significant source of the measured line widths in the other star-forming regions than in IC 10's H II regions.

4. DISCUSSION

Observational studies of the stars and H II regions in IC 10 suggest that the starburst occurred relatively recently, likely in the past $\lesssim 10$Myr (e.g., Hodge & Lee 1990; Hunter 2001). Clustering of the young stellar population (Vacca et al. 2007) and similar properties across multiple regions of the starburst (Polles et al. 2019) in-

dicate a potential common origin for the recent star formation.

In our KCWI observations of the H II regions in IC 10's central starbursting region, we find further evidence that these regions are young, with average crossing times < Myr. Feedback plays an important role in the regulation of star forming environments and the dissipation of material. There are many forms this feedback can take and their contribution can be estimated from their energy or momentum input into the ISM. In our KCWI observations, we only observe the ionized gas and therefore cannot estimate the contribution of every form of potential feedback, but we do estimate the contribution of two important factors: direct radiation pressure, P_{dir}, and warm gas pressure, P_{gas}. Of these two we find the contribution of P_{gas} to be dominant over P_{dir} by ~ 3 orders of magnitude. It should be noted that radiation pressure is sensitive to the effects of stochastic sampling of the initial mass function since the majority of the radiation is produced in the most massive stars. The impact of radiation pressure can therefore be somewhat uncertain in smaller clusters like those powering IC 10's H II regions where the stellar population of the ionizing cluster is not well represented by the assumed IMF. Though, since P_{gas} is ~ 3 orders of magnitude greater than the estimated P_{dir} we do expect radiation pressure to be comparably negligible even if the estimate is impacted by stochasticity. The same trend with a minor contribution from P_{dir} is also found in the giant H II region 30 Doradus (Pellegrini et al. 2011; Lopez et al. 2011), a sample of 32 LMC and SMC H II regions (Lopez et al. 2014), and an additional sample 11 LMC H II regions (McLeod et al. 2019), although to a lesser extent.

The total P_{out} is on average $3\times$ the inward pressure which is predominantly due to turbulence in the surrounding gas. The self-gravity of the H II regions is

Table 8. Size - Velocity Dispersion Relation Fit Parameters: ($\sigma = \beta r_{clump}^{\alpha}$)

Sample	Figure	α	β	Scatter (r)	Scatter (σ)	# of Clumps
all comparisons	25b	$0.406^{+0.025}_{-0.025}$	$3.704^{+1.129}_{-1.154}$	$0.444^{+0.288}_{-0.276}$	$0.414^{+0.275}_{-0.294}$	469
IC 10 & all comparisons	25a	$0.216^{+0.013}_{-0.012}$	$10.442^{+1.072}_{-1.060}$	$0.262^{+0.165}_{-0.171}$	$0.257^{+0.176}_{-0.172}$	515

NOTE—Results of model parameters determined from MCMC fitting of IC 10 H II regions and the local and high-redshift comparison sample for the size-velocity dispersion relationship discussed in Section 3.8.3.

comparably weak in the compact H II regions found in IC 10. This is in contrast to results found in the molecular ISM of nearby galaxies showing kpc and sub-kpc scale equilibrium between gravitational potential and outward pressure (e.g., Sun et al. 2020). However, our H II regions observations are on much smaller size scales, resulting in the average $P_{out} \sim 3 \times P_{in}$, and with 89% of the H II regions identified in IC 10 showing greater P_{out} indicating expansion. This is somewhat at odds with theoretical expectations of feedback effectiveness. For both direct radiation pressure and warm gas pressure, massive stars are expected to be the dominant source of the required ionizing photons, and thus these mechanisms are not expected to limit the star formation efficiency in populations with low stellar mass clusters ($\lesssim 400\,M_{\odot}$, Krumholz et al. 2019). This may vary by cluster due to stochasticity of the IMF, but given we find P_{gas} to be an effective counter to inward pressure in the majority of IC 10's H II regions this may require further exploration. We should note that discussions of limiting the star formation efficiency are usually explored in the context of the larger molecular cloud, while we are limited to studying these mechanisms within the H II regions and therefore cannot directly measure how much impact these mechanisms will have on clearing gas further from the ionizing cluster, but this still implies that P_{gas} may effectively limit star formation efficiency in a wider range of environments than previously expected. This is compounded by another potential source of expansion in the detection of diffuse X-ray emission by Wang et al. (2005) for which they note a morphological similarity with the Hα gas in the region of IC 10 that we observe with KCWI. They argue that this indicates the hot gas is still confined and may be driving expansion of the surrounding ionized gas structures. However, the effectiveness of this hot gas in driving feedback is dependent on leakage and mixing and likely sub-dominant compared to P_{gas} (Lopez et al. 2014).

The stacked spectrum of all the identified H II regions shows further evidence of expansion and/or outflowing gas, with an underlying broad component to the [OIII]5007Å emission line with $\sigma \sim 35\mathrm{km\,s^{-1}}$. Even

the regions with evidence of rotation do not seem to have reached an equilibrium state with the surrounding gas as seen in the $\sim14\mathrm{km\,s^{-1}}$ higher measured velocity dispersions than what would be due to just rotation as well as virial parameters, $\alpha_{vir} \gg 1$. The higher velocity dispersions and elevated log ([OIII]/Hβ) at the edges of many of the H II regions indicate that there may be shocks present which could be due to expansion of the region, champagne flows, or hot stellar winds mixing with cold gas. Over 35% of the regions show these pockets of elevated velocity dispersion at or near the edges of the H II region. The velocity dispersions are not high enough to be produced by shocks in the H II regions themselves as the elevated dispersions are $\sim2\times$ the sound speed, c_s. However, at the H II region boundaries the expanding gas may collide with cold molecular gas in the ISM which could induce a shock. With typical ISM temperatures of ~100K, c_s would be on the order of $1\mathrm{km\,s^{-1}}$ for an ideal gas; $20\times$ less than the areas considered to have elevated velocity dispersion. A previous study of IC 10 ionized gas by Thurow & Wilcots (2005) also found systematically larger line widths outside of H II regions, but they attribute this to superposition of different filaments or shells. These IFU observations have similar spectral resolution to our small slicer, R$\sim$18,000 observations, but with KCWI we are able to achieve $3\times$ greater spatial resolution, limiting the potential for superposition of structures with different velocities. Given that we observe areas of higher velocity dispersion at spaxels with the highest log ([OIII]5007Å/Hβ) we find shocked gas to be a plausible alternative to the superposition of independent filaments, particularly with the significant improvement in spatial resolution of KCWI requiring these structures to be aligned along the line of sight on $\sim$few pc scales.

Resolved areas of significantly elevated velocity dispersion ($\sigma > 25\mathrm{km\,s^{-1}}$) were identified around 6 H II regions with average eddy turnover times $\tau_{eddy} = 1/\sigma \sim 0.2$Myr. The turbulent volumes around the three largest of these H II regions are most likely caused primarily by champagne flows, but stellar winds from early O stars
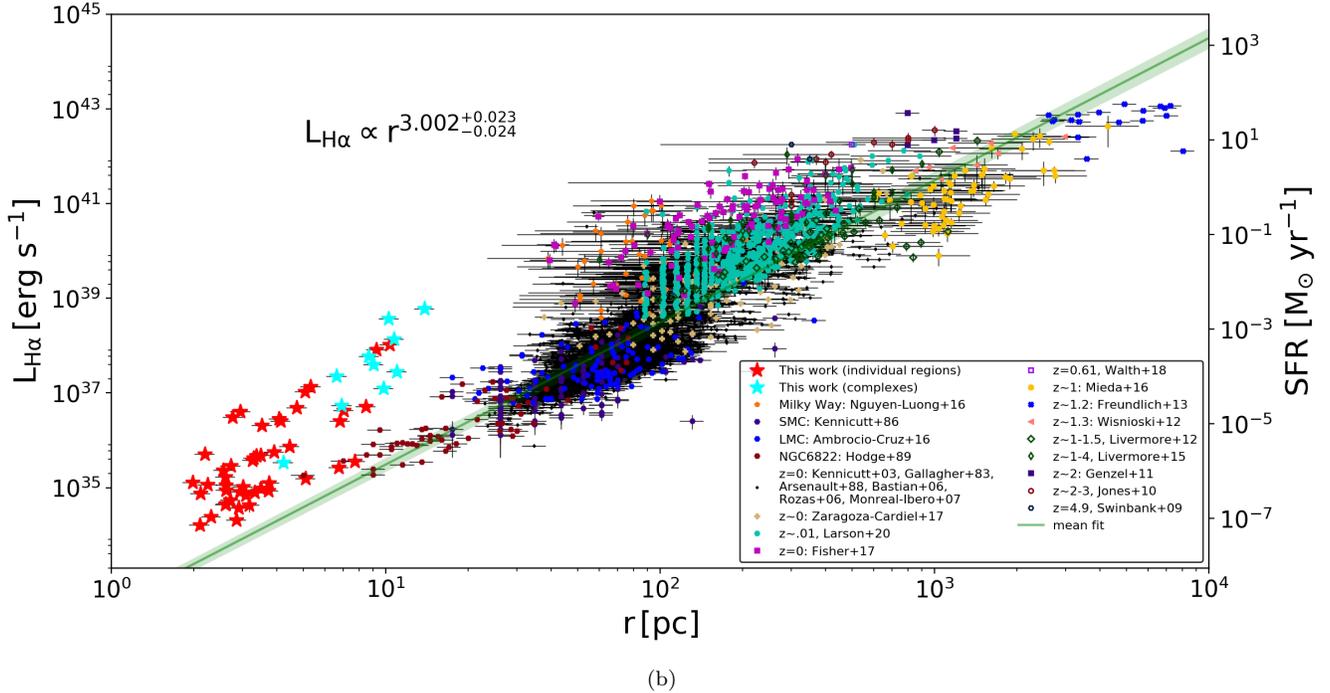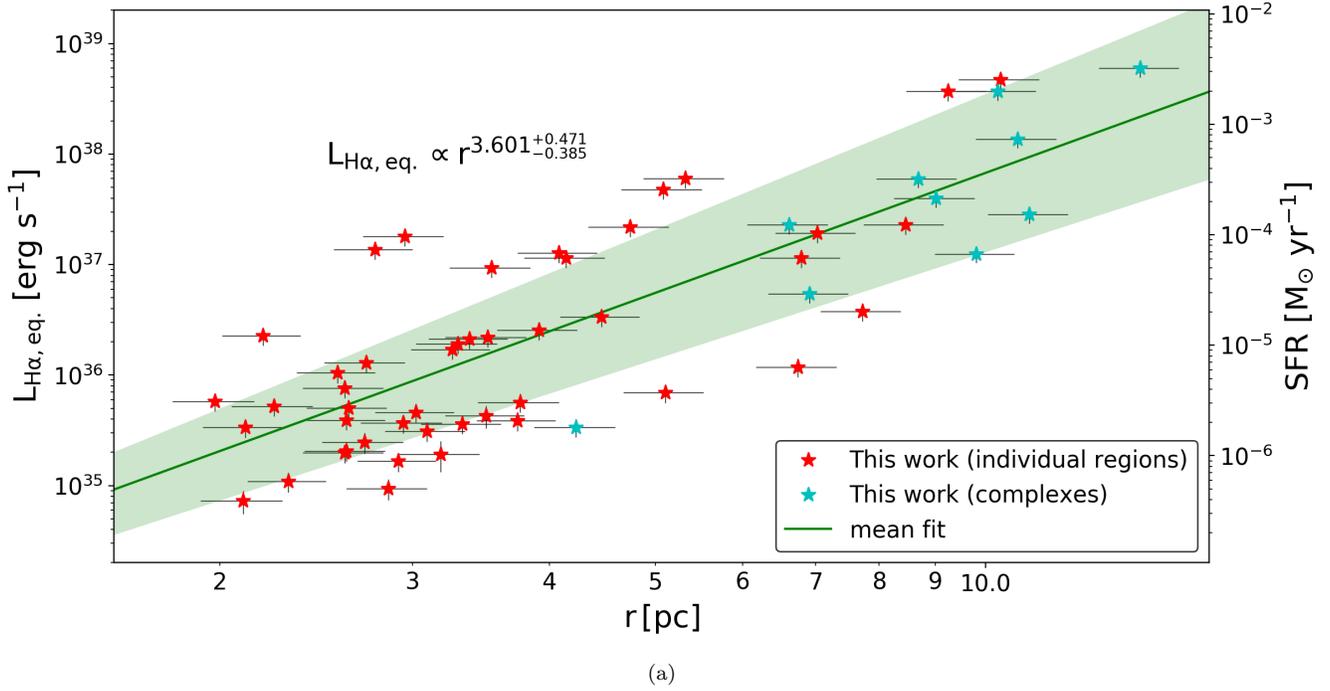
Figure 23. (a): Results of fitting the size-luminosity scaling relationship for IC 10 H II regions identified in our KCWI observations. (b): Results of fitting the size-luminosity scaling relationship for IC 10 H II regions (red stars) as well as the rest of the local and high-redshift sample. The IC 10 region complexes are shown for comparison (cyan stars) but are not included in the determination of the fit.

could also provide sufficient energy to support the rate of turbulent dissipation (L_{turb}). Two of the smaller H II regions with resolved turbulent volumes at the border are ionized by lower mass stars with therefore lower rates of ionizing photon production. In this case we find that stellar winds are more likely to support the observed turbulence and are again sufficient to support L_{turb}. One of the six turbulent volumes has an estimated L_{turb} greater than what we estimate could be provided by the H II region and therefore is likely due to some external source of turbulence.

τ_{eddy} measured for these turbulent regions is at the low end of the range observed in galactic scale outflows driven by starbursts (0.1 - 10 Myr; Veilleux et al. 2005). However, the velocity measured in these ionized gas outflows, FWHM $\sim 61\,\mathrm{km\,s^{-1}}$, is significantly lower than that measured in galactic winds and outflows from individual star forming clumps in other studies. In a sample of 25 star-forming clumps located in LIRGs, Arribas et al. (2014) identify outflows in 83% of clumps with typical FWHM $\sim 200\,\mathrm{km\,s^{-1}}$. Similarly, in the Rodríguez del Pino et al. (2019) study of ionized gas outflows in MaNGA galaxies, finding typical FWHM $\sim 350\,\mathrm{km\,s^{-1}}$ in outflows originating from star-forming regions. Both of these studies find significantly higher velocities to the ionized gas outflows than the IC 10 H II regions which could be due to larger SFR (particularly in the case of the LIRGs), but they also have $\sim 100\times$ lower spatial resolution to what is achieved in IC 10 with KCWI. These measured outflows may then be due to aggregate measurements of multiple compact H II regions and outflows. Some of this variation may also be due to biases introduced by differences in outflow detection methods. Both Arribas et al. (2014) and Rodríguez del Pino et al. (2019) rely on separating a broad outflow component in the emission line of the integrated star-forming region spectra while the resolution of this study allows direct detection of the influence of outflows in the ionized gas surrounding the H II regions. This may then simply probe more localized, lower velocity outflows than has been possible in previous studies.

The velocity dispersions measured inside the identified H II regions are also elevated relative to what would be expected for a rotating region in equilibrium for all cases showing evidence of rotational motion. The H II regions we identify in IC 10 tend to be offset from the scaling relationships found between the region size & luminosity as well as from the Larson's Law between size & velocity dispersion. Krieger et al. (2020) find a similar offset to larger line widths for a given size when comparing molecular clouds in the starburst NGC 253 to clouds in the Milky Way's Galactic center, which they attribute to

gas that is not gravitationally bound and rather lies in transient structures. Based on the discrepancies in mass estimates and the young ages of IC 10's H II regions, it seems likely that these H II regions are still young enough to be undergoing expansion. They may then evolve onto the typical size-luminosity and size-velocity dispersion sequences after reaching an equilibrium state with the surrounding ISM.

The evolutionary stage of the Wolf-Rayet stars in the field of view provide another clue that the H II regions which host them are young. Wolf-Rayet stars are a later evolutionary stage of O stars which occurs before a type I SNe. In general, high mass O stars ($> 40 M_\odot$) evolve to a WN type WR, then a WC, and then a SNIc, whereas lower mass O stars are thought to not reach the WC stage and simply explode as a SNIb (Crowther 2007). Of the eight WR stars in the field covered by our KCWI observations, four of these fall in an H II region. Two have been identified as WN spectral types (M24 and T5 in H II regions H16a and M12 respectively), one is identified as an early WC (R10 in region I18), and the last has not yet been spectroscopically confirmed. Of the four WR stars outside of IC 10 H II regions, one is a late WN type and the rest are identified as WC. These stars are located in areas where ionized gas is nearby, but more diffuse and filamentary in appearance. The locations of these WR stars and their spectral type are shown in Figure 26 with the observed [OIII]5007Å flux and H II region contours. Though this is a small sample, the trend implies that WR stars in the WN stage could be more likely to be found in current H II regions, whereas WC types might be more likely found in areas of diffuse gas where an H II region may have previously been present. This would imply that the star clusters the WN stars belong to are younger and the surrounding gas has not yet been disrupted.

5. SUMMARY

We made use of the highest resolution mode of the Keck Cosmic Web Imager IFS $-$ 0.35″ spatial sampling with 1″ FWHM and R$\sim$18,000 $-$ to study the population of H II regions in our nearest starburst galaxy IC 10. These high quality IFS observations allowed us to study the spatial and kinematic properties of the H II regions in detail. We identified 46 individual H II regions in the central burst of the irregular galaxy with a total SFR$\sim 6 \times 10^{-3}$ M$_\odot$ yr^{-1}. The average H II region identified has a size of 4.0 pc, an SFR of 1.3×10^{-4} M$_\odot$ yr^{-1}, an ionized gas mass $M_{HII} \sim 56$ M$_\odot$, and a velocity dispersion of $\sim$16km s^{-1}.

Over 95% of the identified H II region luminosities are consistent with the ionizing photon production rate of a
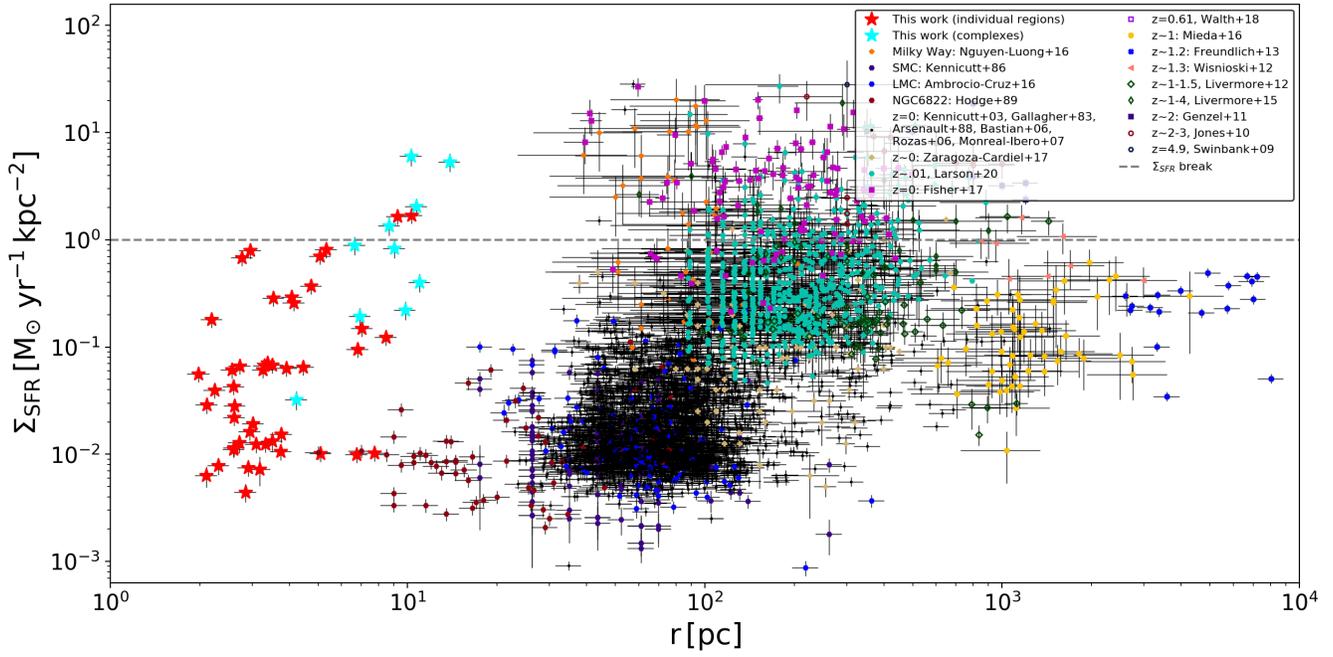
(a)
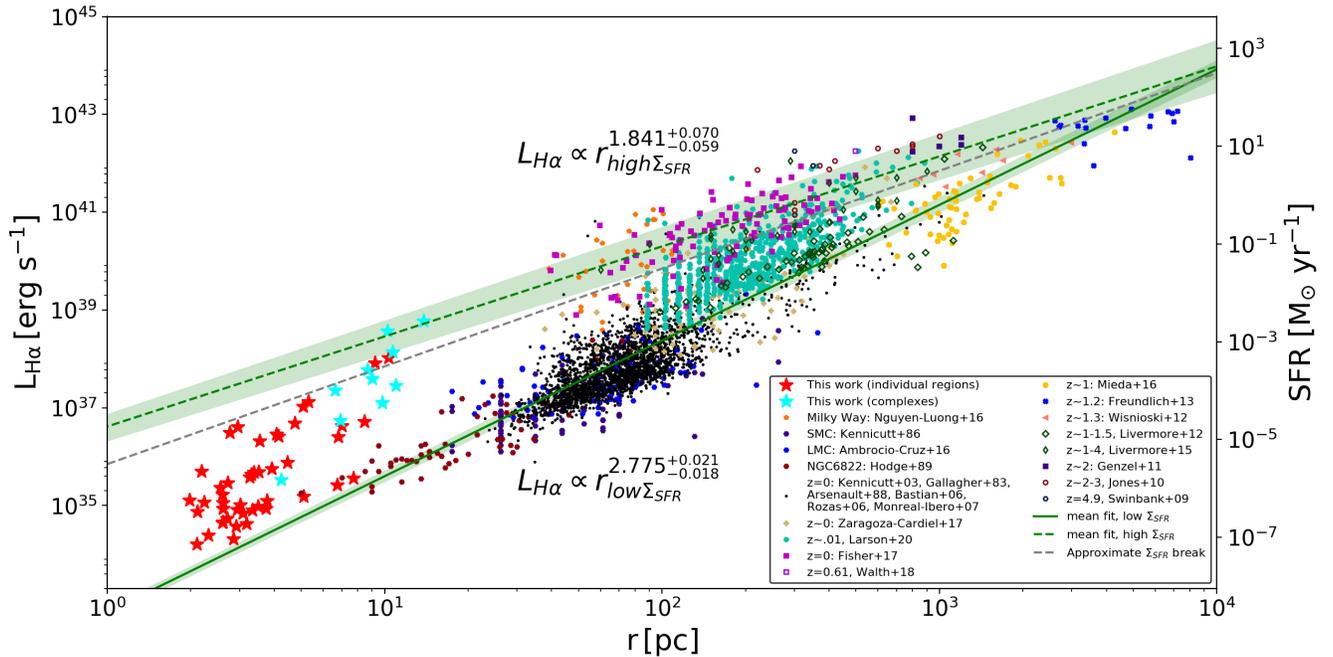
(b)

Figure 24. (a): Size vs. Σ_{SFR} for H II regions identified in our observations of IC 10 as well as each comparison sample. These data are divided into high and low Σ_{SFR} based on a break at $\Sigma_{SFR} = 1\,M_\odot\,\mathrm{yr}^{-1}\,\mathrm{kpc}^{-2}$ (dashed line). (b): Results of fitting the size-luminosity scaling relationship for these two groups. The low Σ_{SFR} subset tends towards a slop of $L \sim r^3$, while the high Σ_{SFR} subset produces a slope closer to $L \sim r^2$. The IC 10 region complexes are shown for comparison (cyan stars) but are not included in the determination of the fit.

single O or B star. 10 of the H II regions ($\sim$22%) can be powered by a single B star, with the lowest luminosity region requiring at minimum a star of spectral type B0.5.

The H II regions appear to be blue-shifted relative to the systemic velocity of IC 10 ($\sim$12km s^{-1}) while the diffuse surrounding gas often shows a relative red-shift. Supplementary KCWI observations with lower resolution and wider wavelength coverage are used to estimate the oxygen abundance via the KK04 and PT05 metallicity calibrations, both of which make use of the R_{23} strong-line calibration. These estimates yield averages of $12 + \log(\text{O/H})_{\text{PT05,lower}} \approx 7.85 \pm 0.03$ and $12 + \log(\text{O/H})_{\text{KK04,lower}} \approx 8.22 \pm 0.02$ with the "true" metallicity expected to lie within this range.

IC 10's H II regions have very short crossing times ($\tau_{\text{cr}} < $ Myr) and are not virialized ($\alpha_{\text{vir}} >> 1$ and $\text{M}_{\text{vir}} >> \text{M}_{\text{HII}}$). The measured velocity dispersions in the H II regions are also too high to be due to rotational motion alone (by $\sim$11-12 km s^{-1}). We see evidence that these regions are generally still undergoing expansion. The IC 10 H II regions are offset from the scaling relationships found between the region size & luminosity as well as the size & velocity dispersion relationship. As these regions expand they may evolve onto the scaling relationships determined for the other samples of H II regions and star-forming clumps.

We estimated the contribution of the thermal gas pressure, P_{gas}, and direct radiation pressure, P_{dir}, to the outward pressure in the H II regions. We find P_{gas} to be the dominant force of expansion in IC 10's H II regions, being $\sim$3 orders of magnitude greater than P_{dir} using the definition of P_{dir} based on ionizing photon production rate. We also find $P_{\text{out}} > P_{\text{in}}$ in 89% of the H II regions before accounting for additional expansion from hot gas pressure, a somewhat surprising result given the low stellar masses estimated for the ionizing stars. Five of the H II regions show evidence of outflows that may be supported by energy in the ionizing cluster either in the form of stellar winds or champagne flows. These pressure and energy estimates add further evidence that the H II regions in IC 10 are young and undergoing expansion into the ISM and suggest that thermal gas pressure may be a more effective form of feedback than previously expected from low mass clusters.

These high resolution and SNR observations were possible in just 1.5 nights of Keck observing time. From just this short time we were able to obtain detailed kinematic and flux maps of a significant number of H II regions. With additional observations the remainder of IC 10's H II regions can be observed in the same modes, with deeper observations of the diffuse gas and the supplementary low resolution mode. More expansive coverage of H II regions and the DIG in IC 10 will allow for detailed study of the kinematic and ionization state differences between these unique regions of ionized gas. KCWI observations at high spectral resolving power of the remainder of IC 10 would also double the number of H II regions in this unique starburst environment in which the impact of different modes of feedback and outflows can be investigated.

A relatively small investment of time with optical IFS's such as KCWI and VLT/MUSE can quickly yield a large sample of local star-forming regions in a wide range of environments. The large field of view and moderate spectral resolving power (R$\sim$2000-4000) of MUSE provides an efficient tool for mapping ionization states of H II regions and the ISM, while the R$\sim$18,000 mode of KCWI can be leveraged for a detailed look at the gas kinematics in compact regions. Utilizing these powerful IFU's across a wide sample of star forming galaxies will allow a detailed and statistically significant study of how environmental conditions impact the effectiveness of feedback mechanisms and vice versa; and whether there are age and environmental dependencies when looking at the scaling relationships. Targeted IFU studies of this kind are already well underway and as a larger collective sample is built we will be able to better compare these results with theoretical predictions of feedback and inform new models.

The reduced data cubes used in this study are available by request to facilitate further study beyond the scope of this project.

$\sigma \propto r^{0.405^{+0.025}_{-0.024}}$

(a)

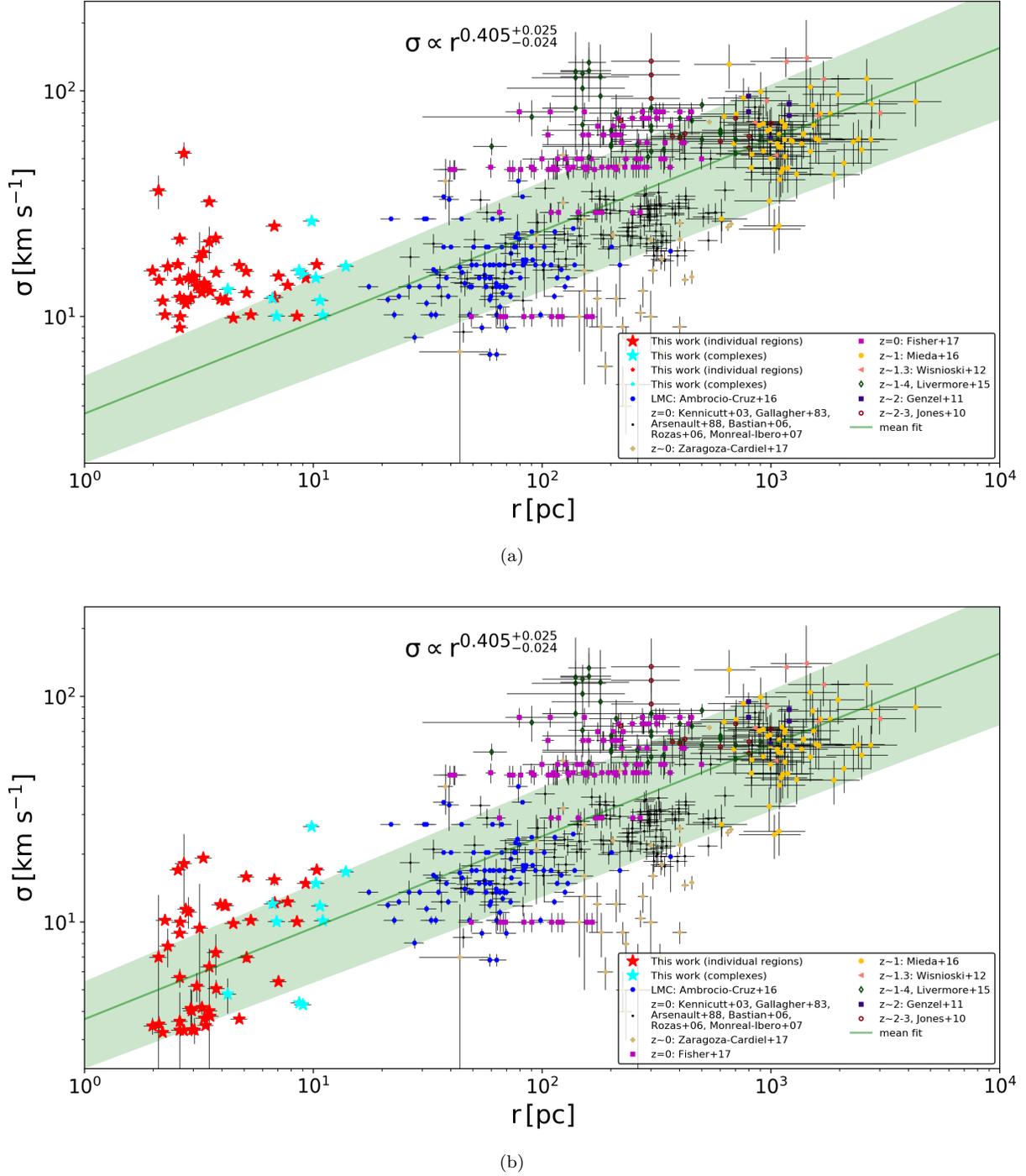$\sigma \propto r^{0.405^{+0.025}_{-0.024}}$

(b)

Figure 25. Size vs. σ relationship for the star-forming regions in each comparison sample containing spectral information. The fit is computed using our MCMC framework excluding the IC 10 H II regions (red stars) and complexes (cyan stars) from the analysis. The mean fit is shown with the green line while the uncertainty in the fit is denoted by the shaded green region. (a): Both the IC 10 H II regions and complexes fall above this mean fit, and in most cases above the uncertainty as well, indicating that these H II regions are not virialized. The complexes lie closer to the mean relationship while still tending towards higher σ for a given size, further supporting the conclusion that the individual regions are not virialized as the increase in size does not result in a proportional increase in measured line width. (b): The IC 10 H II regions and complexes lie along the mean size - σ *after* the excess velocity dispersion determined in Section 3.5.4 is removed. The excess dispersion was found to be in addition to that produced by rotational motion of the H II region gas and is therefore likely due to outflows or expansion of the ionized gas.
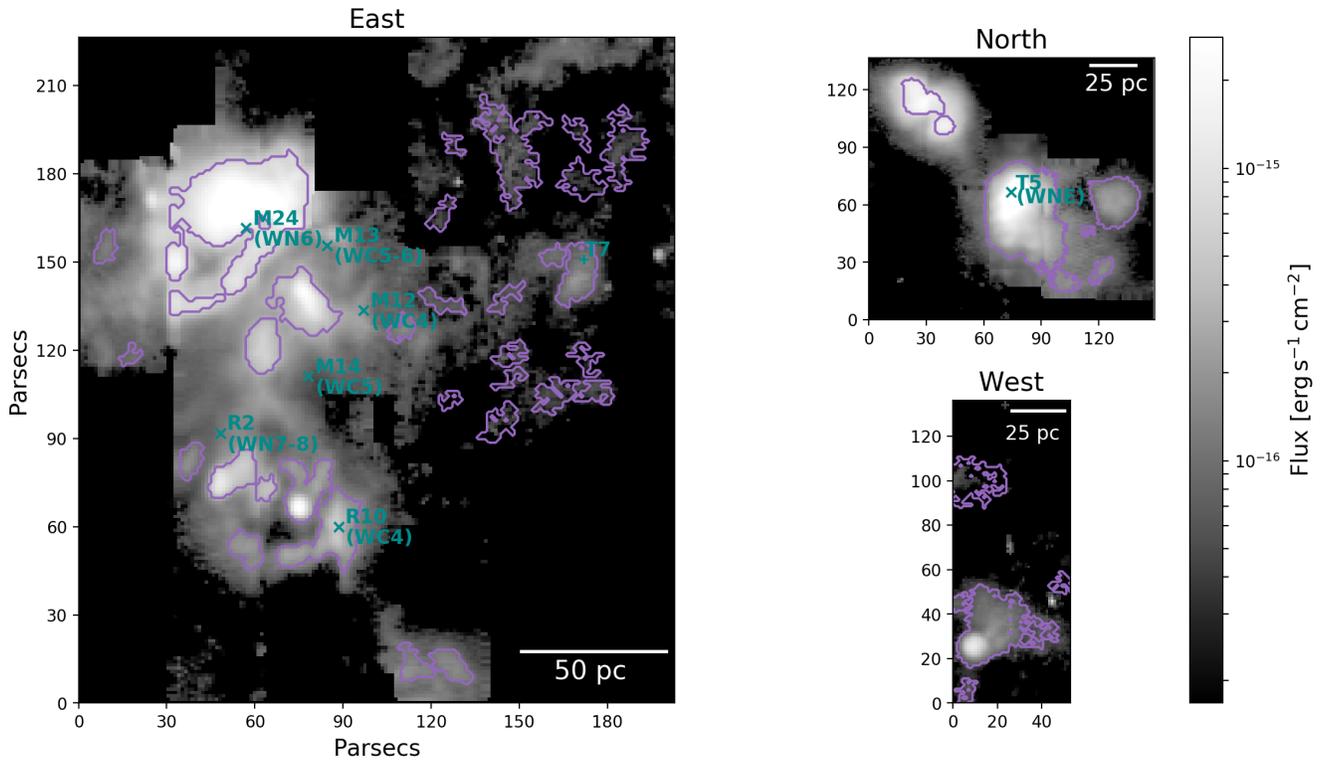
Figure 26. [OIII]5007Å integrated flux map with region contours reproduced from Figure 3 with marked locations of all known WR stars ('X') and WR candidates ('+'). The stars designation is included to the right of the location marker with the WR type in parentheses if it has been spectroscopically confirmed.

et al. 2018), IPython (Perez & Granger 2007) Matplotlib (Hunter 2007), NumPy (Harris et al. 2020), pandas (The Pandas Development Team 2016; Wes McKinney 2010), photutils (Bradley et al. 2019), PyStan (Stan Development Team 2017), reproject (Robitaille et al. 2020) SHAPE (Steffen et al. 2011)

APPENDIX

A. H II REGION NAMING CONVENTION

The previous naming of IC 10 H II regions was developed by Hodge & Lee (1990) where regions are assigned a number in order of increasing RA. If that region breaks up into smaller knots then a letter is added after the complex number (e.g., 111a). Throughout the literature this region identifier is typically preceded by either "HL90" or simply "HL" to indicate the origin of the identifier. This is a simple and clear way of tabulating the H II regions found in this early study but there are some significant shortcomings of this system now. One difficulty is in quickly identifying regions in the Hα maps as regions are only numbered based on their RA while there can be a large spread in Dec from one region to the next in the sequence. The other more problematic issue is that with better resolution and sensitivity one would expect to identify new H II regions and complexes breaking into more knots. When this occurs there is not a clear way in which to assign an identifier to these new regions. If the next number in the sequence is assigned to each new region there would no longer be a clear ordering based on RA, and reassigning numbers to each region with every new identification would make comparison between studies exceedingly difficult.

We have therefore proposed a new naming convention that we believe addresses these issues for our study and allows extension to future studies with even wider fields using the grid described in Section 3.1.1. This numbering scheme simplifies identification of nearby regions in both RA and Dec as well as extension to a larger FoV. This could be applied to the larger IC 10 H I envelope by increasing the numbering range in Dec. and extending the RA designation to double and/or negative lettering (e.g., AA or -A). Fainter H II regions may be identified in already occupied grid squares, but the next trailing letter in the sequence can be added as these should have lower luminosity than what is identified here.
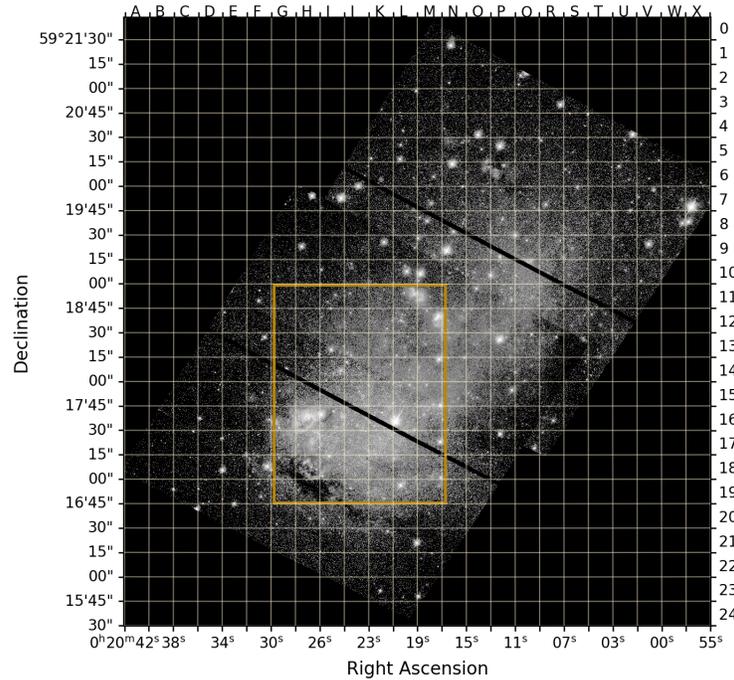
Figure A1. Coordinate grid for proposed H II region naming scheme overlaid on an HST/ACS image showing the optical extent of the galaxy. H II regions are named based on the lettered column and numbered row corresponding to their center. This could be extended to the larger H I envelope of IC 10 by going to larger positive and negative numbers as well as double and/or negative lettering (e.g., AA or -A). The gold rectangle outlines the region of IC 10 which our KCWI observations fall in.

B. IMPACT OF RADIUS DEFINITION

The choice of how to define the radius of an H II region varies significantly between studies, and particularly between local and high-redshift studies.

In observational studies of local H II regions there is wide variation in the methods used to define the size of the region, with this often not being a critical aim of the study. For example, the Green Bank Telescope H II Region Discovery Survey (HRDS) measures the sizes of 441 H II regions in the Milky Way by taking the mean of the FWHM of Gaussians fit to the RA and Dec components of continuum observations (Anderson et al. 2011). In the extensive CALIFA survey of over 26,000 extragalactic H II regions, a custom procedure called `HIIEXPLORER` (Sánchez et al. 2012b) (and the Python version `PYHIIEXPLORER`; Espinosa-Ponce et al. 2020) is used to identify H II regions. This procedure is similar in methodology to `astrodendro` except that the maximum expected extent of H II regions is provided as an input constraint. The sizes of identified regions then tend towards a relatively uniform distribution (Sánchez et al. 2012b), and the authors note that extracting reliable sizes was not a main goal of their methodology partly due to the resolution of their observations.

Studies of local GMCs typically use the second moments of the cloud structure to determine its properties (Heyer & Dame 2015). Often the geometric mean of the second moments of the cloud structure (in the direction of greatest elongation and perpendicular to that) is used to describe the RMS extent of a cloud, σ_r. An empirical factor is then used to determine the radius of a spherical cloud, $R = \eta \sigma_r$. This factor was first determined empirically in Solomon et al. (1987) to be $\eta = 1.91$ for converting their rectangular regions to spherical clouds and is used throughout the literature to convert the second moments of a variety of structures to a spherical radius. Rosolowsky & Leroy (2006) go through the derivation of this factor of η for a spherical cloud with a density profile of $\rho \propto r^{-1}$ and determine a theoretical value of $\sqrt{6} \approx 2.45$. They suggest that deviation may be due partly to the use of CO data to trace the GMC density which is shallower than the actual density profile due to saturation in dense regions and lack of detection in low density regions. This would mean that the "true" value of η would lie somewhere between the empirical value of 1.91 from Solomon et al. (1987) and the value of 2.45 determined from their toy model of a GMC. However, they recommend continued use of the radius definition from Solomon et al. (1987) in order to remain consistent with this data set. Since our observations are of ionized rather than molecular gas we do not use this same factor of η, and instead assume a Gaussian profile in our determination of $r^*_{1/2}$ from the second moments.

Zaragoza-Cardiel et al. (2017) combine CO and Hα observations in local LIRGs with regions identified using `astrodenro`. They define the radius, r, using the second moments of the structures in both cases, with the factor of 1.91 from Solomon et al. (1987). They compare the ratio of this radius to that derived from the area of the full structure, r_{eff}, and find an average $\frac{r}{r_{\text{eff}}} = 0.86 \pm 0.14$. In another sample of local LIRGs with star-forming regions identified by `astrodendro`, Larson et al. (2020) use r_{eff} to define the size of regions. Larson et al. (2020) also performs a comparison of the `astrodendro` and `CLUMPFIND` identification routines finding similar average radii and SFR, but a narrower range of fluxes for a given radius of star-forming region due to a lack of local background subtraction.

In studies of high-redshift star-forming clumps, differences in the method used to determine region sizes are also present, although perhaps less significant due to the decrease in resolution. Wisnioski et al. (2012) compares the size determined from isophotes of constant flux and from fitting a Gaussian to the radial surface profile of H II regions. They find r_{eff} from the isophotal method to be systematically larger than $r_{1/2}$ determined via Gaussian fitting, but the luminosities to be consistent between the two methods. This comes from the emission being dominated by the higher intensity cores of the H II regions. They argue that $r_{1/2}$ from Gaussian fitting is a better defined observational parameter as it is less likely to be contaminated by diffuse emission that could be significant at high-redshift. Livermore et al. (2012) also compare clump sizes determined by r_{eff} of `CLUMPFIND` isophotal structures and from fitting a 2D elliptical Gaussian profile to emission peaks. They find that using `CLUMPFIND` for their sample gives 25% larger estimates of size than from the FWHM of the 2D elliptical Gaussian, but include error bars encompassing both measures. They note a smaller deviation between their `CLUMPFIND` radii and the FWHM of fitted Gaussians than in Wisnioski et al. (2012) due in part to the use of multiple isophote levels in `CLUMPFIND` that does not need to be tuned in the same way as other single isophote methods.

Which of the many possible radius definitions is used has a significant impact on the typical size of star-forming regions and on the scaling relationships determined from those properties. To quantify just how much impact the choice of using the pseudo half-light radius ($r^*_{1/2}$) definition for the H II region radii has in this study we perform MCMC fitting with different choices of radius definition and identification constraint for our sample. We fit the relationship

between region size and luminosity for (i) the IC 10 H II regions alone, for (ii) local samples only, and for (iii) the full sample of local and high-redshift H II regions and clumps. These results are shown in Table 9.

Table 9. Radius Definition Implications

`astrodendro` Constraint	Radius Definition	Filtering	$N_{regions}$	R_{avg}		Slopes	
				(pc)	IC 10	Local	All Data
	$r^*_{1/2}$	$\cdots$	46	4.0	$3.601^{+0.471}_{-0.385}$	$3.049^{+0.029}_{-0.025}$	$3.002^{+0.023}_{-0.024}$
	$r^*_{1/2}$	r>FWHM	20	5.6	$2.972^{+0.793}_{-0.483}$	$3.147^{+0.032}_{-0.035}$	$3.067^{+0.032}_{-0.021}$
2r > FWHM	r_{eff}	$\cdots$	45	6.8	$2.979^{+0.426}_{-0.344}$	$3.045^{+0.025}_{-0.026}$	$2.987^{+0.020}_{-0.028}$
	r_{maj}	$\cdots$	46	5.1	$3.176^{+0.451}_{-0.351}$	$2.999^{+0.036}_{-0.026}$	$2.951^{+0.031}_{-0.025}$
r > FWHM	$r^*_{1/2}$	$\cdots$	23	6.1	$2.888^{+0.558}_{-0.388}$	$3.161^{+0.026}_{-0.025}$	$3.043^{+0.025}_{-0.024}$

NOTE—Results of model slope determined from MCMC fitting of the size-luminosity relationship for IC 10 H II regions and the local and high-redshift comparison sample based on different ways of defining and constraining the radius of IC 10 H II regions.

Col 1: constraint used in `astrodendro` to define an independent structure. The top section uses the more relaxed constraint that the diameter of the region must be larger than the FWHM determined from standard star observations (this always uses the definition of $r^*_{1/2}$ to match the Gaussian fit to the stars PSF). In the bottom row we require this diameter to be twice the standard star FWHM.

Col 2: radius definition used to determine H II region size; $r^*_{1/2}$, and r_{eff} used as described in Section 3.1.2, and r_{maj} is determined by converting the second moment in the direction of greatest elongation to the HWHM of a Gaussian.

Col 3: additional filtering applied to exclude regions from MCMC fits beyond the manual filtering of bad regions as described in Section 3.1

Col 4: Number of H II regions found in IC 10 based on these constraints and filtering.

Col 5: Average radius of IC 10 H II regions.

Col 6 - 8: slope and uncertainty determined from MCMC fitting of the size-luminosity relationship for IC 10 regions only (7), local regions only (8) and all local and high-redshift data (9).

Regardless of our chosen definition for region size, the slope of the local and full sample is consistent within $< 5\%$. However, there is a larger difference in the slope of the IC 10 H II region sample alone. Using the most relaxed resolution constraint in `astrodendro` and $r^*_{1/2}$ produces a slope for which the nominal value deviates by 18% from either a stricter resolution constraint (bottom row) or the definitions of r_{eff} and r_{maj} for the region size. Fitting only the IC 10 H II regions, however, leads to significantly larger uncertainties so the nominal slopes for each radius constraint are still consistent within the 1σ uncertainties.

C. SPECTRA THUMBNAILS
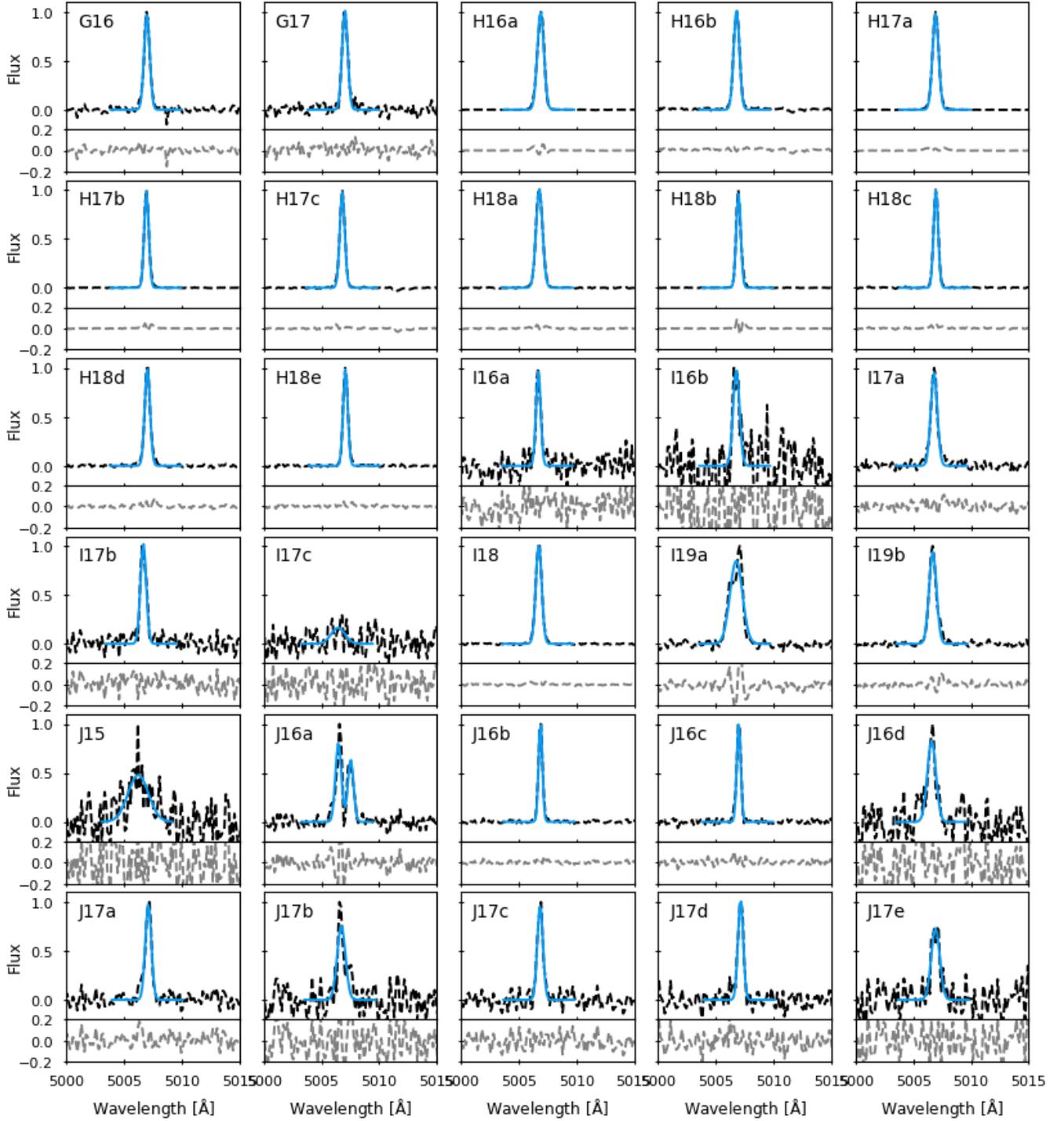
Figure C1. Spectral thumbnails of [OIII]5007Å from all H II regions detected in the small slicer, R∼18,000 observing mode. These lines are fit by a single Gaussian profile (except for J16a with a double Gaussian profile) shown in cyan with the residuals shown in grey below the associated spectrum. The spectra have been normalized to the peak of the [OIII]5007Å line.
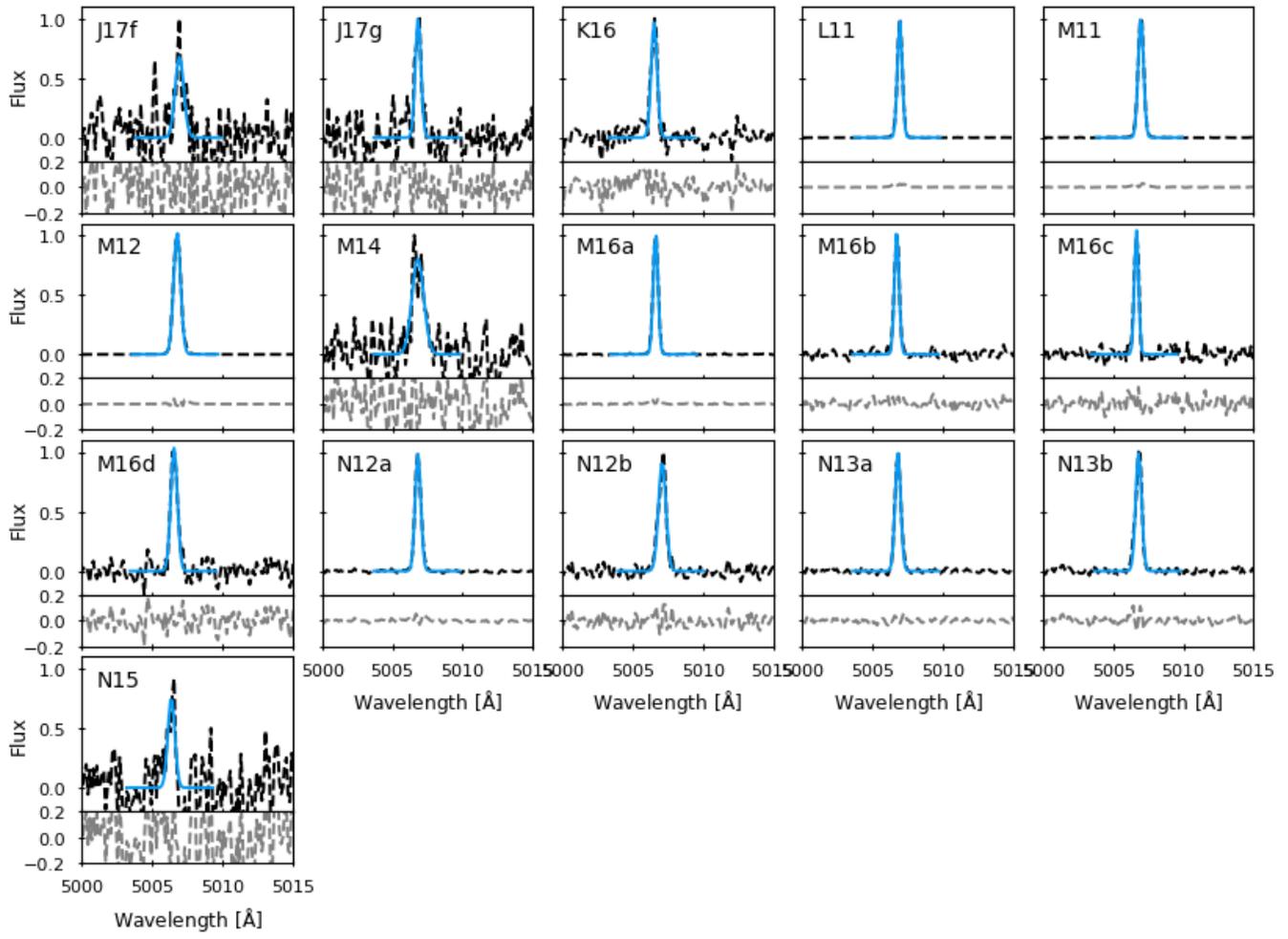
Figure C2. Figure C1 cont'd.

D. H II REGION MAPS
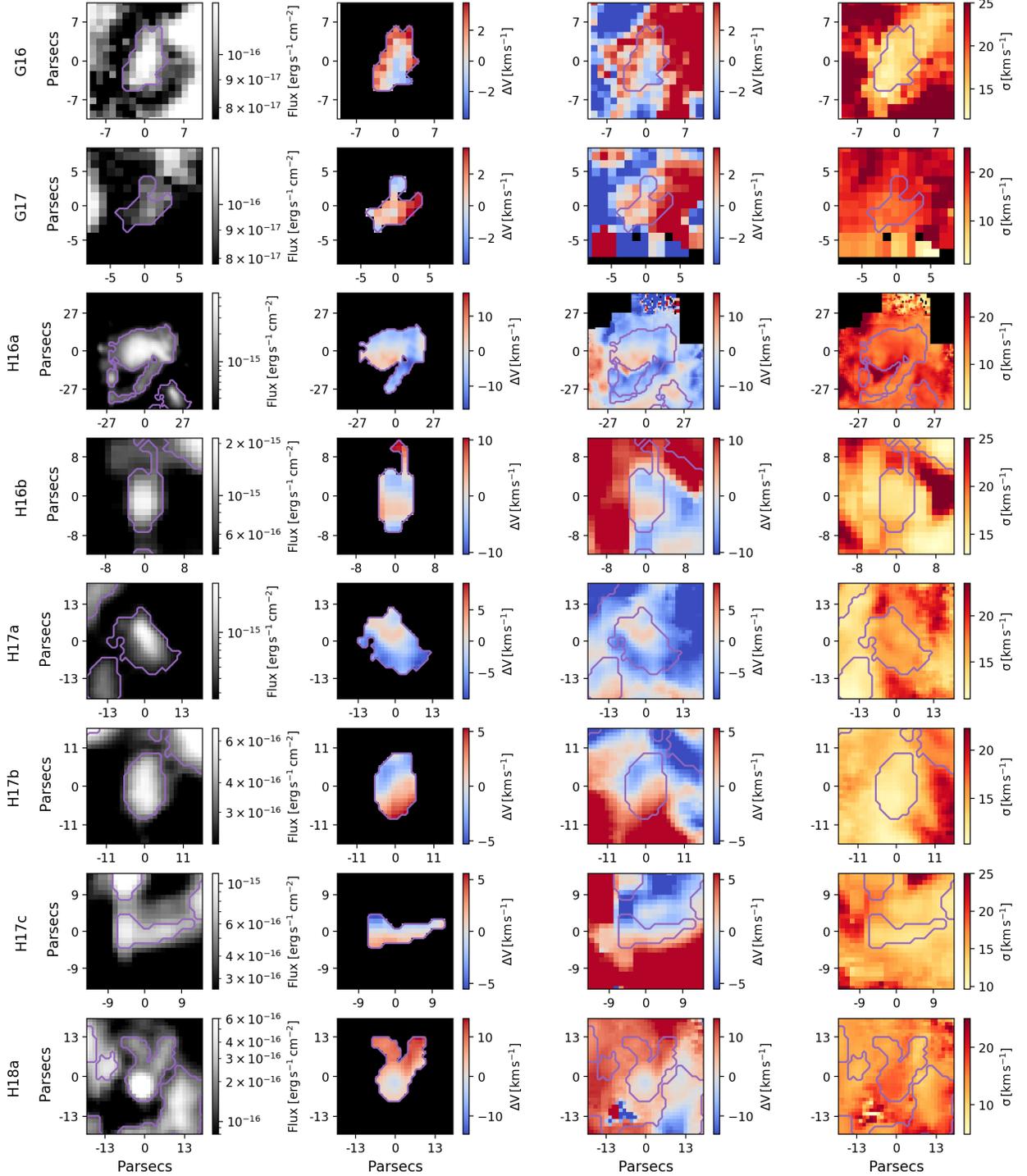
Figure D1. Thumbnail maps of H II regions identified in our KCWI observations. (Left): Flux maps of the surrounding area. (Center Left): Velocity shift of spaxels within the H II region relative to the systemic velocity of the region. (Center Right): Velocity shift of the H II region and the surrounding gas. (Left): Velocity dispersion within the H II region and the surrounding gas. Regions of elevated velocity dispersion may be indicative of outflowing gas, particularly when correlated with a velocity shift relative to the surrounding gas.
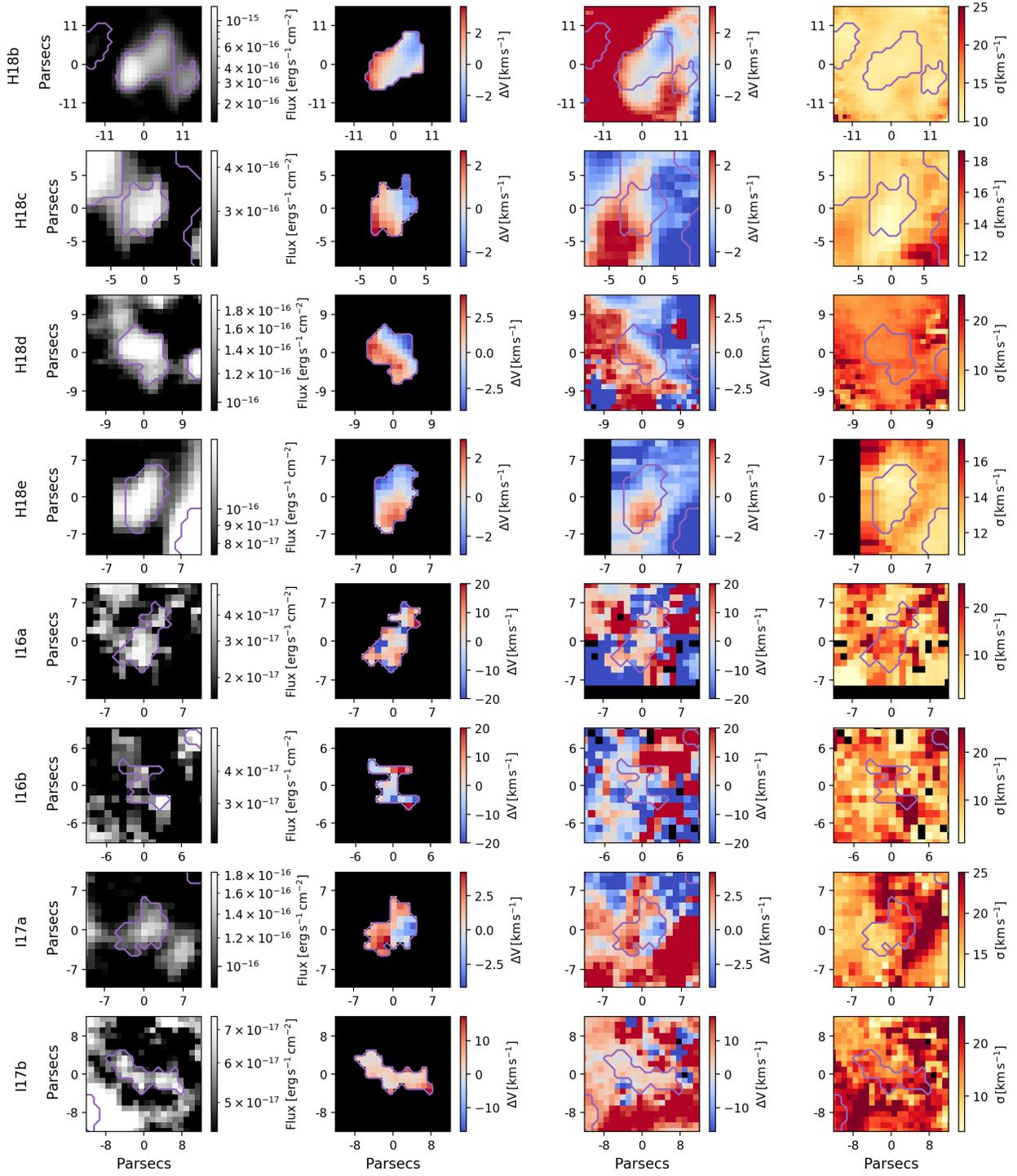
Figure D2. Figure D1 cont'd.
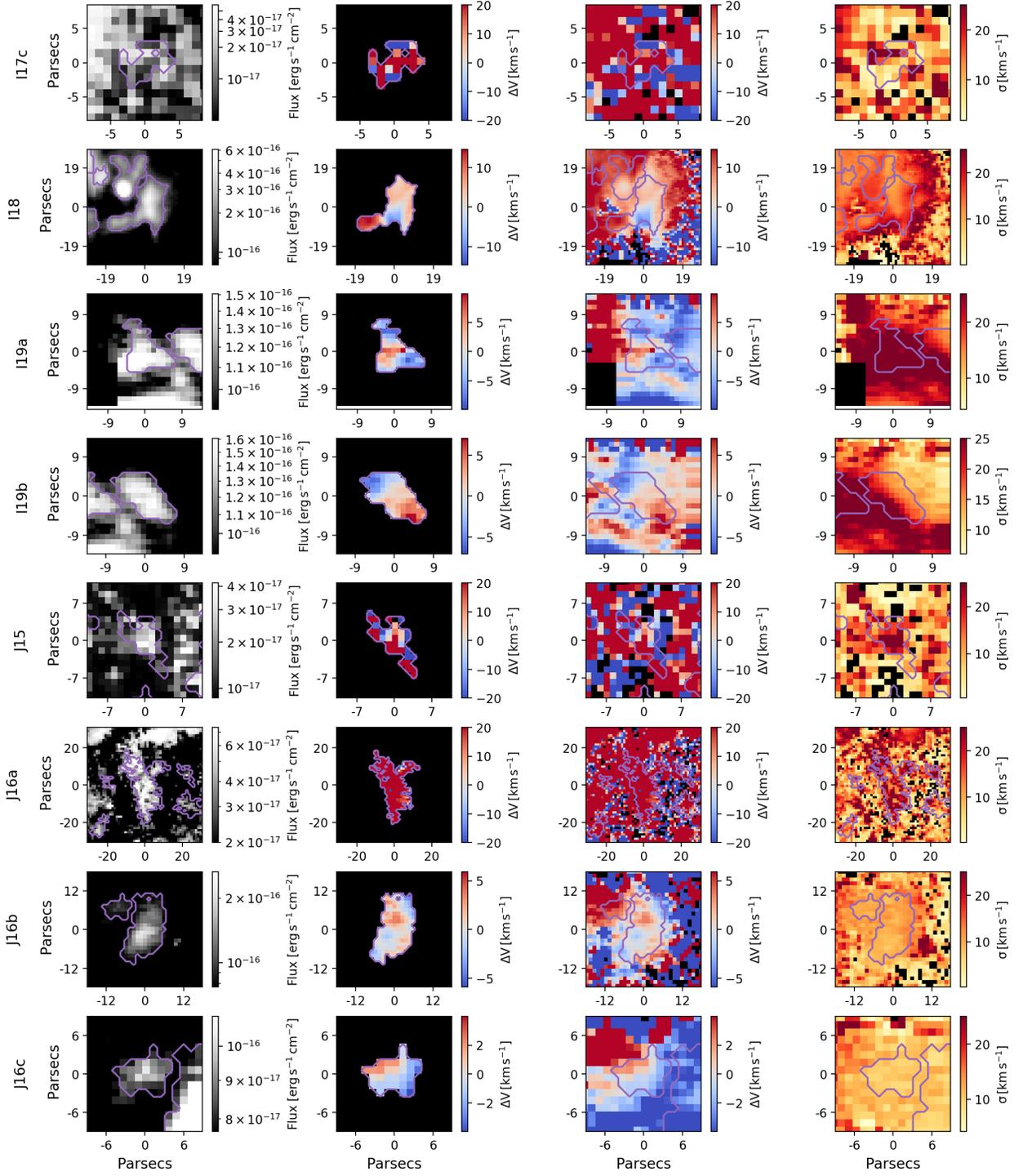
Figure D3. Figure D1 cont'd.
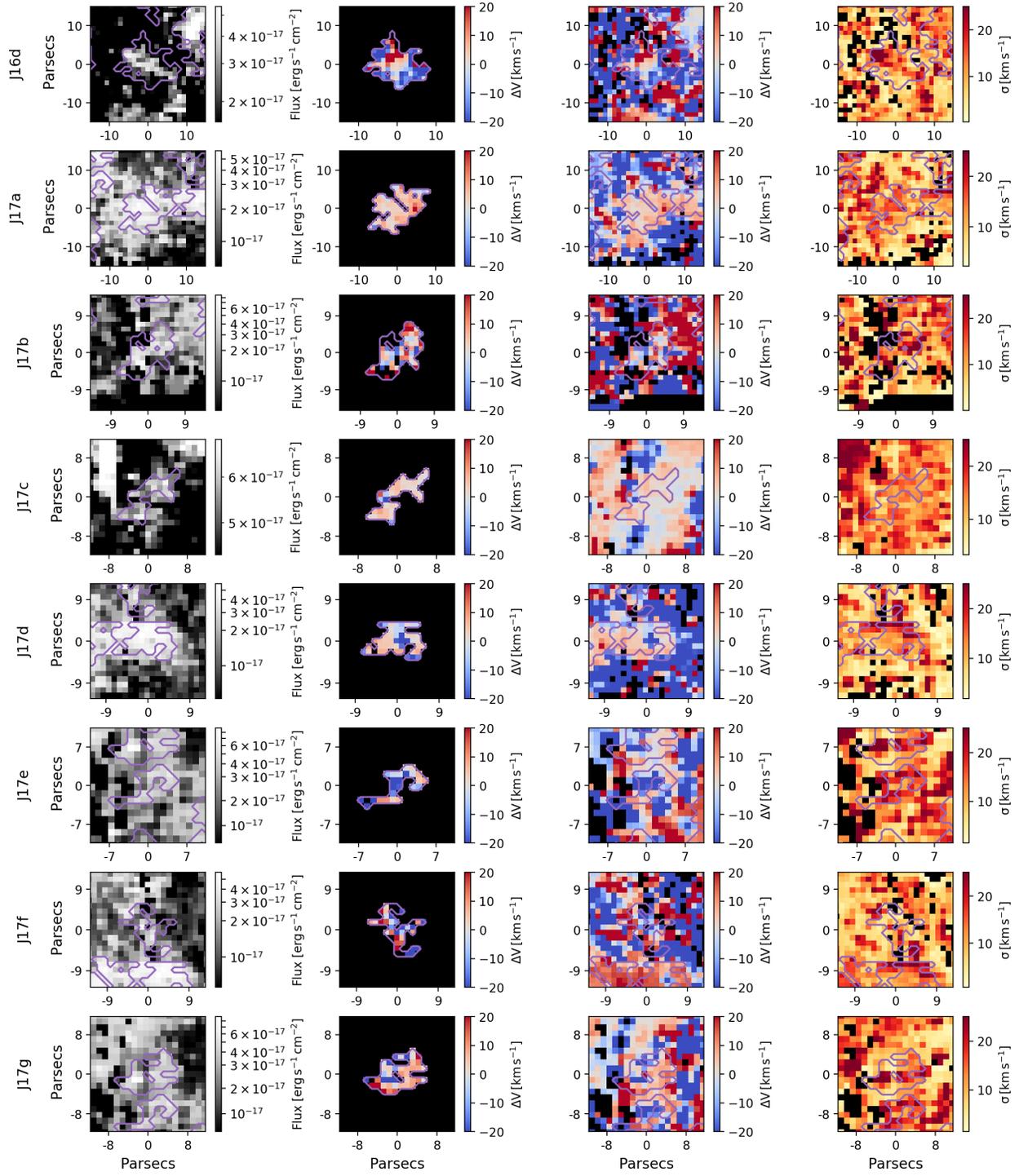
Figure D4. Figure D1 cont'd.
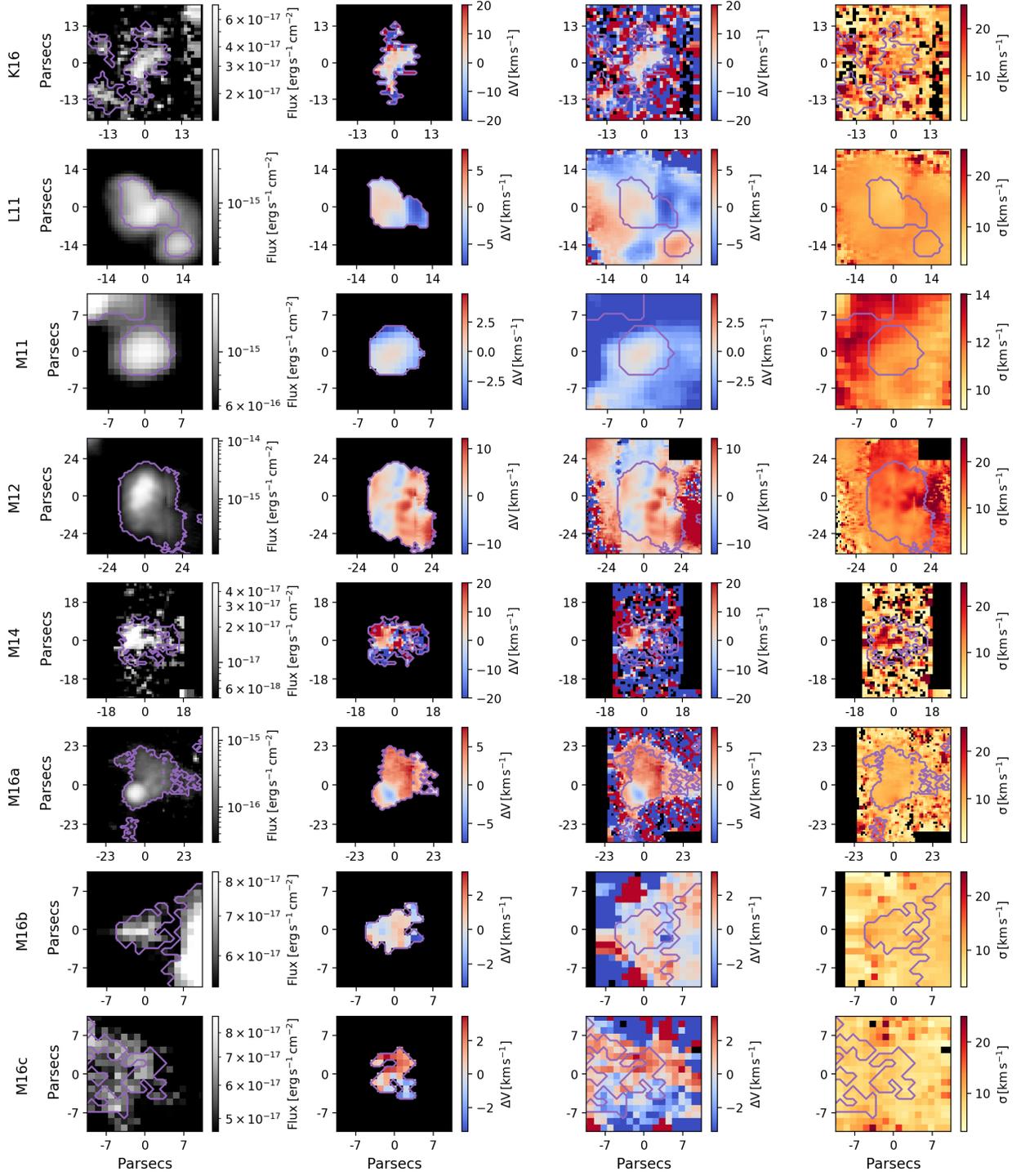
Figure D5. Figure D1 cont'd.
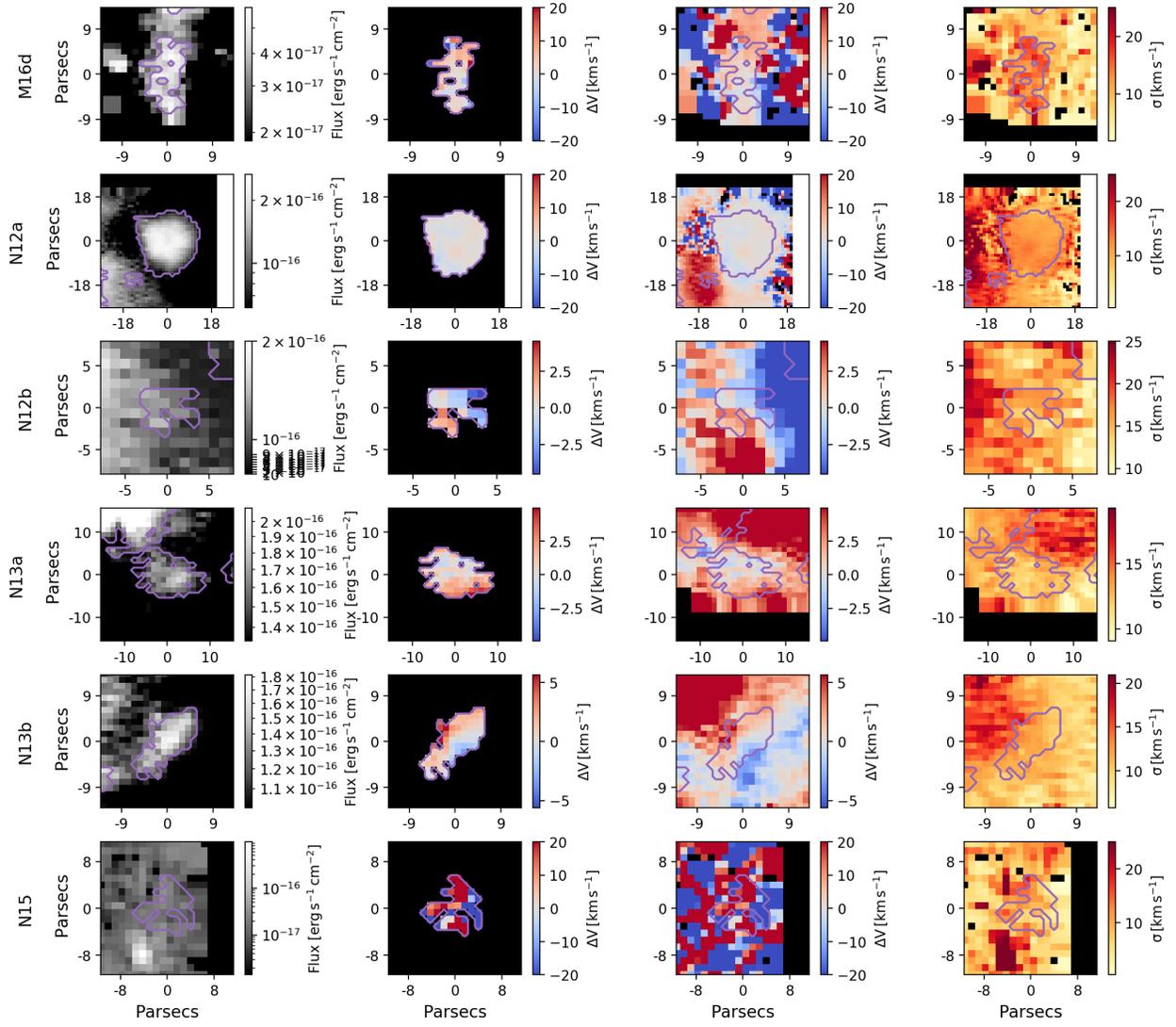
Figure D6. Figure D1 cont'd.

REFERENCES

Ambrocio-Cruz, P., Le Coarer, E., Rosado, M., et al. 2016, MNRAS, 457, 2048, doi: 10.1093/mnras/stw054

Anderson, L. D., Bania, T. M., Balser, D. S., & Rood, R. T. 2011, ApJS, 194, 32, doi: 10.1088/0067-0049/194/2/32

Armentrout, W. P., Anderson, L. D., Wenger, T. V., Balser, D. S., & Bania, T. M. 2021, ApJS, 253, 23, doi: 10.3847/1538-4365/abd5c0

Arribas, S., Colina, L., Bellocchi, E., Maiolino, R., & Villar-Martín, M. 2014, A&A, 568, A14, doi: 10.1051/0004-6361/201323324

Arsenault, R., Roy, J. R., & Boulesteix, J. 1990, A&A, 234, 23

Ashley, T., Elmegreen, B. G., Johnson, M., et al. 2014, AJ, 148, 130, doi: 10.1088/0004-6256/148/6/130

Astropy Collaboration, Robitaille, T. P., Tollerud, E. J., et al. 2013, A&A, 558, A33, doi: 10.1051/0004-6361/201322068

Bacon, R., Accardo, M., Adjali, L., et al. 2010, in Society of Photo-Optical Instrumentation Engineers (SPIE) Conference Series, Vol. 7735, Ground-based and Airborne Instrumentation for Astronomy III, ed. I. S. McLean, S. K. Ramsay, & H. Takami, 773508, doi: 10.1117/12.856027

Bolatto, A. D., Leroy, A. K., Rosolowsky, E., Walter, F., & Blitz, L. 2008, ApJ, 686, 948, doi: 10.1086/591513

Bottinelli, L., Gouguenheim, L., Paturel, G., & de Vaucouleurs, G. 1984, A&AS, 56, 381

Bradley, L., Sipőcz, B., Robitaille, T., et al. 2019, astropy/photutils: v0.7.2, v0.7.2, Zenodo, doi: 10.5281/zenodo.3568287

Bresolin, F., Rizzi, L., Ho, I. T., et al. 2020, MNRAS, 495, 4347, doi: 10.1093/mnras/staa1472

Bundy, K., Bershady, M. A., Law, D. R., et al. 2015, ApJ, 798, 7, doi: 10.1088/0004-637X/798/1/7

Cardelli, J. A., Clayton, G. C., & Mathis, J. S. 1989, ApJ, 345, 245, doi: 10.1086/167900

Castro, N., Crowther, P. A., Evans, C. J., et al. 2018, A&A, 614, A147, doi: 10.1051/0004-6361/201732084

Cortese, L., Fogarty, L. M. R., Ho, I. T., et al. 2014, ApJL, 795, L37, doi: 10.1088/2041-8205/795/2/L37

Cosens, M., Wright, S. A., Mieda, E., et al. 2018, ApJ, 869, 11, doi: 10.3847/1538-4357/aaeb8f

Cresci, G., Mannucci, F., & Curti, M. 2019, A&A, 627, A42, doi: 10.1051/0004-6361/201834637

Croom, S. M., Lawrence, J. S., Bland-Hawthorn, J., et al. 2012, MNRAS, 421, 872, doi: 10.1111/j.1365-2966.2011.20365.x

Crowther, P. A. 2007, ARA&A, 45, 177, doi: 10.1146/annurev.astro.45.051806.110615

Davies, R. D., Elliott, K. H., & Meaburn, J. 1976, MmRAS, 81, 89

Don, N., Matt, M., & Chris, M. 2018, KCWI data reduction pipeline, 1.1.0. https://github.com/Keck-DataReductionPipelines/KcwiDRP/releases/tag/v1.1.0

Ellison, S. L., Sánchez, S. F., Ibarra-Medel, H., et al. 2018, MNRAS, 474, 2039, doi: 10.1093/mnras/stx2882

Espinosa-Ponce, C., Sánchez, S. F., Morisset, C., et al. 2020, MNRAS, 494, 1622, doi: 10.1093/mnras/staa782

Ferland, G. J., Chatzikos, M., Guzmán, F., et al. 2017, RMxAA, 53, 385. https://arxiv.org/abs/1705.10877

Fisher, D. B., Glazebrook, K., Damjanov, I., et al. 2017, MNRAS, 464, 491, doi: 10.1093/mnras/stw2281

Genzel, R., Newman, S., Jones, T., et al. 2011, ApJ, 733, 101, doi: 10.1088/0004-637X/733/2/101

Hannon, S., Lee, J. C., Whitmore, B. C., et al. 2019, MNRAS, 490, 4648, doi: 10.1093/mnras/stz2820

Harper-Clark, E., & Murray, N. 2009, ApJ, 693, 1696, doi: 10.1088/0004-637X/693/2/1696

Harris, C. R., Millman, K. J., van der Walt, S. J., et al. 2020, Nature, 585, 357–362, doi: 10.1038/s41586-020-2649-2

Heyer, M., & Dame, T. M. 2015, ARA&A, 53, 583, doi: 10.1146/annurev-astro-082214-122324

Hidalgo-Gámez, A. M. 2005, A&A, 442, 443, doi: 10.1051/0004-6361:20041663

Hodge, P., & Lee, M. G. 1990, PASP, 102, 26, doi: 10.1086/132603

Hodge, P., Lee, M. G., & Kennicutt, Robert C., J. 1989, PASP, 101, 32, doi: 10.1086/132401

Hollyhead, K., Bastian, N., Adamo, A., et al. 2015, MNRAS, 449, 1106, doi: 10.1093/mnras/stv331

Huchtmeier, W. K. 1979, A&A, 75, 170

Hunter, D. A. 2001, ApJ, 559, 225, doi: 10.1086/322399

Hunter, J. D. 2007, Computing in Science & Engineering, 9, 90, doi: 10.1109/MCSE.2007.55

Israel, F. P. 1978, A&A, 70, 769

Kennicutt, R. C., J., & Hodge, P. W. 1986, ApJ, 306, 130, doi: 10.1086/164326

Kennicutt, Robert C., J. 1992, ApJ, 388, 310, doi: 10.1086/171154

—. 1998, ARA&A, 36, 189, doi: 10.1146/annurev.astro.36.1.189

Kerton, C. R., Wolf-Chase, G., Arvidsson, K., Lintott, C. J., & Simpson, R. J. 2015, ApJ, 799, 153, doi: 10.1088/0004-637X/799/2/153

Kewley, L. J., & Ellison, S. L. 2008, ApJ, 681, 1183, doi: 10.1086/587500

Kewley, L. J., Nicholls, D. C., & Sutherland, R. S. 2019,
ARA&A, 57, 511,
doi: 10.1146/annurev-astro-081817-051832

Kim, M., Kim, E., Hwang, N., et al. 2009, ApJ, 703, 816,
doi: 10.1088/0004-637X/703/1/816

Kobulnicky, H. A., & Kewley, L. J. 2004, ApJ, 617, 240,
doi: 10.1086/425299

Krieger, N., Bolatto, A. D., Koch, E. W., et al. 2020, ApJ,
899, 158, doi: 10.3847/1538-4357/aba903

Kroupa, P. 2001, MNRAS, 322, 231,
doi: 10.1046/j.1365-8711.2001.04022.x

Krumholz, M. R., McKee, C. F., & Bland-Hawthorn, J.
2019, ARA&A, 57, 227,
doi: 10.1146/annurev-astro-091918-104430

Krumholz, M. R., Bate, M. R., Arce, H. G., et al. 2014, in
Protostars and Planets VI, ed. H. Beuther, R. S. Klessen,
C. P. Dullemond, & T. Henning, 243,
doi: 10.2458/azu_uapress_9780816531240-ch011

Krumholz, M. R., Adamo, A., Fumagalli, M., et al. 2015,
ApJ, 812, 147, doi: 10.1088/0004-637X/812/2/147

Lacerda, E. A. D., Cid Fernandes, R., Couto, G. S., et al.
2018, MNRAS, 474, 3727, doi: 10.1093/mnras/stx3022

Lamers, H. J., & M. Levesque, E. 2017, in Understanding
Stellar Evolution, 2514-3433 (IOP Publishing), 15–1 to
15–12, doi: 10.1088/978-0-7503-1278-3ch15

Larson, K. L., Díaz-Santos, T., Armus, L., et al. 2020, ApJ,
888, 92, doi: 10.3847/1538-4357/ab5dc3

Larson, R. B. 1981, MNRAS, 194, 809,
doi: 10.1093/mnras/194.4.809

Lebouteiller, V., Sloan, G. C., Groenewegen, M. A. T.,
et al. 2012, A&A, 546, A94,
doi: 10.1051/0004-6361/201220087

Lequeux, J., Peimbert, M., Rayo, J. F., Serrano, A., &
Torres-Peimbert, S. 1979, A&A, 500, 145

Livermore, R. C., Jones, T., Richard, J., et al. 2012,
MNRAS, 427, 688, doi: 10.1111/j.1365-2966.2012.21900.x

Livermore, R. C., Jones, T. A., Richard, J., et al. 2015,
MNRAS, 450, 1812, doi: 10.1093/mnras/stv686

Lopez, L. A., Krumholz, M. R., Bolatto, A. D., Prochaska,
J. X., & Ramirez-Ruiz, E. 2011, ApJ, 731, 91,
doi: 10.1088/0004-637X/731/2/91

Lopez, L. A., Krumholz, M. R., Bolatto, A. D., et al. 2014,
ApJ, 795, 121, doi: 10.1088/0004-637X/795/2/121

Lundquist, M. J., Kobulnicky, H. A., Alexander, M. J.,
Kerton, C. R., & Arvidsson, K. 2014, ApJ, 784, 111,
doi: 10.1088/0004-637X/784/2/111

Magrini, L., & Gonçalves, D. R. 2009, MNRAS, 398, 280,
doi: 10.1111/j.1365-2966.2009.15124.x

Martins, F., Schaerer, D., & Hillier, D. J. 2005, A&A, 436,
1049, doi: 10.1051/0004-6361:20042386

McLeod, A. F., Dale, J. E., Evans, C. J., et al. 2019,
MNRAS, 486, 5263, doi: 10.1093/mnras/sty2696

Mieda, E., Wright, S. A., Larkin, J. E., et al. 2016, ApJ,
831, 78, doi: 10.3847/0004-637X/831/1/78

Momcheva, I. G., Lee, J. C., Ly, C., et al. 2013, AJ, 145,
47, doi: 10.1088/0004-6256/145/2/47

Morrissey, P., Matuszewski, M., Martin, D. C., et al. 2018,
ApJ, 864, 93, doi: 10.3847/1538-4357/aad597

Moustakas, J., Kennicutt, Robert C., J., & Tremonti, C. A.
2006, ApJ, 642, 775, doi: 10.1086/500964

Moustakas, J., Kennicutt, Robert C., J., Tremonti, C. A.,
et al. 2010, ApJS, 190, 233,
doi: 10.1088/0067-0049/190/2/233

Murphy, E. J., Condon, J. J., Schinnerer, E., et al. 2011,
ApJ, 737, 67, doi: 10.1088/0004-637X/737/2/67

Nagao, T., Maiolino, R., & Marconi, A. 2006, A&A, 459,
85, doi: 10.1051/0004-6361:20065216

Namumba, B., Carignan, C., Foster, T., & Deg, N. 2019,
MNRAS, 490, 3365, doi: 10.1093/mnras/stz2737

Nidever, D. L., Ashley, T., Slater, C. T., et al. 2013, ApJL,
779, L15, doi: 10.1088/2041-8205/779/2/L15

O'Dell, C. R., Ferland, G. J., & Peimbert, M. 2017,
MNRAS, 464, 4835, doi: 10.1093/mnras/stw2713

Oey, M. S., Meurer, G. R., Yelda, S., et al. 2007, ApJ, 661,
801, doi: 10.1086/517867

Osterbrock, D. E., & Ferland, G. J. 2006, Astrophysics of
gaseous nebulae and active galactic nuclei

Pagel, B. E. J., Edmunds, M. G., Blackwell, D. E., Chun,
M. S., & Smith, G. 1979, MNRAS, 189, 95,
doi: 10.1093/mnras/189.1.95

Pellegrini, E. W., Baldwin, J. A., & Ferland, G. J. 2011,
ApJ, 738, 34, doi: 10.1088/0004-637X/738/1/34

Perez, F., & Granger, B. E. 2007, Computing in Science &
Engineering, 9, 21

Pilyugin, L. S., & Thuan, T. X. 2005, ApJ, 631, 231,
doi: 10.1086/432408

Polles, F. L., Madden, S. C., Lebouteiller, V., et al. 2019,
A&A, 622, A119, doi: 10.1051/0004-6361/201833776

Price-Whelan, A. M., Sipőcz, B. M., Günther, H. M., et al.
2018, AJ, 156, 123, doi: 10.3847/1538-3881/aabc4f

Relaño, M., Beckman, J. E., Zurita, A., Rozas, M., &
Giammanco, C. 2005, A&A, 431, 235,
doi: 10.1051/0004-6361:20040483

Robitaille, T., Deil, C., & Ginsburg, A. 2020, reproject:
Python-based astronomical image reprojection.
http://ascl.net/2011.023

Rodríguez del Pino, B., Arribas, S., Piqueras López, J.,
Villar-Martín, M., & Colina, L. 2019, MNRAS, 486, 344,
doi: 10.1093/mnras/stz816

Rogers, H., & Pittard, J. M. 2013, MNRAS, 431, 1337,
   doi: 10.1093/mnras/stt255

Rosolowsky, E., & Leroy, A. 2006, PASP, 118, 590,
   doi: 10.1086/502982

Rosolowsky, E. W., Pineda, J. E., Kauffmann, J., &
   Goodman, A. A. 2008, ApJ, 679, 1338,
   doi: 10.1086/587685

Rozas, M., Sabalisck, N., Beckman, J. E., & Knapen, J. H.
   1998, A&A, 338, 15

Russell, S. C., & Dopita, M. A. 1990, ApJS, 74, 93,
   doi: 10.1086/191494

Sakai, S., Madore, B. F., & Freedman, W. L. 1999, ApJ,
   511, 671, doi: 10.1086/306716

Salpeter, E. E. 1955, ApJ, 121, 161, doi: 10.1086/145971

Sánchez, S. F., Kennicutt, R. C., Gil de Paz, A., et al.
   2012a, A&A, 538, A8, doi: 10.1051/0004-6361/201117353

Sánchez, S. F., Rosales-Ortega, F. F., Marino, R. A., et al.
   2012b, A&A, 546, A2, doi: 10.1051/0004-6361/201219578

Schlegel, D. J., Finkbeiner, D. P., & Davis, M. 1998, ApJ,
   500, 525, doi: 10.1086/305772

Shostak, G. S., & Skillman, E. D. 1989, A&A, 214, 33

Skillman, E. D., Kennicutt, R. C., & Hodge, P. W. 1989,
   ApJ, 347, 875, doi: 10.1086/168178

Smith, L. J., Norris, R. P. F., & Crowther, P. A. 2002,
   MNRAS, 337, 1309,
   doi: 10.1046/j.1365-8711.2002.06042.x

Solomon, P. M., Rivolo, A. R., Barrett, J., & Yahil, A.
   1987, ApJ, 319, 730, doi: 10.1086/165493

Spitzer, L. 1978, Physical processes in the interstellar
   medium, doi: 10.1002/9783527617722

Stan Development Team. 2017, PyStan: the Python
   interface to Stan, 2.16.0.0. http://mc-stan.org

Steffen, W., Koning, N., Wenger, S., Morisset, C., &
   Magnor, M. 2011, IEEE Transactions on Visualization
   and Computer Graphics, 17, 454,
   doi: 10.1109/TVCG.2010.62

Sun, J., Leroy, A. K., Ostriker, E. C., et al. 2020, ApJ, 892,
   148, doi: 10.3847/1538-4357/ab781c

Tehrani, K., Crowther, P. A., & Archer, I. 2017, MNRAS,
   472, 4618, doi: 10.1093/mnras/stx2124

Tenorio-Tagle, G. 1979, A&A, 71, 59

Teplitz, H. I., Malkan, M. A., Steidel, C. C., et al. 2000,
   ApJ, 542, 18, doi: 10.1086/309539

The Pandas Development Team. 2016, pandas-dev/pandas:
   Pandas, 0.19.2.
   https://pandas.pydata.org/pandas-docs/version/0.19.2/

Thomas, R., Chris, B., Braden, M., & Erik, R. 2013,
   astrodendro, doi: http://www.dendrograms.org/

Thurow, J. C., & Wilcots, E. M. 2005, AJ, 129, 745,
   doi: 10.1086/426751

Tifft, W. G., & Cocke, W. J. 1988, ApJS, 67, 1,
   doi: 10.1086/191265

Vacca, W. D., Sheehy, C. D., & Graham, J. R. 2007, ApJ,
   662, 272, doi: 10.1086/516725

Valdez-Gutiérrez, M., Rosado, M., Puerari, I., et al. 2002,
   AJ, 124, 3157, doi: 10.1086/344304

Veilleux, S., Cecil, G., & Bland-Hawthorn, J. 2005,
   ARA&A, 43, 769,
   doi: 10.1146/annurev.astro.43.072103.150610

Wang, Q. D., Whitaker, K. E., & Williams, R. 2005,
   MNRAS, 362, 1065,
   doi: 10.1111/j.1365-2966.2005.09379.x

Wes McKinney. 2010, in Proceedings of the 9th Python in
   Science Conference, ed. Stéfan van der Walt & Jarrod
   Millman, 56 – 61, doi: 10.25080/Majora-92bf1922-00a

Wilcots, E. M., & Miller, B. W. 1998, AJ, 116, 2363,
   doi: 10.1086/300595

Wisnioski, E., Glazebrook, K., Blake, C., et al. 2012,
   MNRAS, 422, 3339,
   doi: 10.1111/j.1365-2966.2012.20850.x

Yang, H., & Skillman, E. D. 1993, AJ, 106, 1448,
   doi: 10.1086/116738

Zamora-Avilés, M., Vázquez-Semadeni, E., González, R. F.,
   et al. 2019, MNRAS, 487, 2200,
   doi: 10.1093/mnras/stz1235

Zaragoza-Cardiel, J., Beckman, J., Font, J., et al. 2017,
   MNRAS, 465, 3461, doi: 10.1093/mnras/stw2963

Zaragoza-Cardiel, J., Beckman, J. E., Font, J., et al. 2015,
   MNRAS, 451, 1307, doi: 10.1093/mnras/stv1024